

**AFRL-RD-PS-  
TR-2013-0003**

**AFRL-RD-PS-  
TR-2013-0003**

## **INVESTIGATION OF Co, Ni and Fe DOPED II-VI CHALCOGENIDES**

**Sergey B. Mirov**

**University of Alabama at Birmingham  
701 20<sup>th</sup> Street  
South AB 990  
Birmingham, AL 35294-0001**

**04 January 2013**

**Final Report**

**APPROVED FOR PUBLIC RELEASE: DISTRIBUTION UNLIMITED.**



**AIR FORCE RESEARCH LABORATORY  
Directed Energy Directorate  
3550 Aberdeen Ave SE  
AIR FORCE MATERIEL COMMAND  
KIRTLAND AIR FORCE BASE, NM 87117-5776**

## NOTICE AND SIGNATURE PAGE

Using Government drawings, specifications, or other data included in this document for any purpose other than Government procurement does not in any way obligate the U.S. Government. The fact that the Government formulated or supplied the drawings, specifications, or other data does not license the holder or any other person or corporation; or convey any rights or permission to manufacture, use, or sell any patented invention that may relate to them.

This report was cleared for public release by the Air Force Research Laboratory [insert TD site] Public Affairs Office and is available to the general public, including foreign nationals. Copies may be obtained from the Defense Technical Information Center (DTIC) (<http://www.dtic.mil>).

AFRL-RD-PS-TR-2013-0003 HAS BEEN REVIEWED AND IS APPROVED  
FOR PUBLICATION IN ACCORDANCE WITH ASSIGNED DISTRIBUTION  
STATEMENT.

//Signed//  
LEANNE J. HENRY, DR-III  
Project Manager

//Signed//  
KENTON T. WOOD, DR-IV, DAF  
Chief, Laser Division

This report is published in the interest of scientific and technical information exchange, and its publication does not constitute the Government's approval or disapproval of its ideas or findings.

<b>REPORT DOCUMENTATION PAGE</b>				<i>Form Approved</i> <i>OMB No. 0704-0188</i>	
<small>Public reporting burden for this collection of information is estimated to average 1 hour per response, including the time for reviewing instructions, searching existing data sources, gathering and maintaining the data needed, and completing and reviewing this collection of information. Send comments regarding this burden estimate or any other aspect of this collection of information, including suggestions for reducing this burden to Department of Defense, Washington Headquarters Services, Directorate for Information Operations and Reports (0704-0188), 1215 Jefferson Davis Highway, Suite 1204, Arlington, VA 22202-4302. Respondents should be aware that notwithstanding any other provision of law, no person shall be subject to any penalty for failing to comply with a collection of information if it does not display a currently valid OMB control number. <b>PLEASE DO NOT RETURN YOUR FORM TO THE ABOVE ADDRESS.</b></small>					
<b>1. REPORT DATE (DD-MM-YYYY)</b> 01-04-2013		<b>2. REPORT TYPE</b> Final Report		<b>3. DATES COVERED (From - To)</b> 06/04/2010 – 01/04/2013	
<b>4. TITLE AND SUBTITLE</b> Investigation of Co, Ni and Fe Doped II-VI Chalcogenides				<b>5a. CONTRACT NUMBER</b> FA9451-10-C-0254	
				<b>5b. GRANT NUMBER</b> N/A	
				<b>5c. PROGRAM ELEMENT NUMBER</b> 62605F	
<b>6. AUTHOR(S)</b> Sergey B. Mirov				<b>5d. PROJECT NUMBER</b> 4866	
				<b>5e. TASK NUMBER</b> LR10	
				<b>5f. WORK UNIT NUMBER</b> D01J	
<b>7. PERFORMING ORGANIZATION NAME(S) AND ADDRESS(ES)</b> University of Alabama at Birmingham 701 20 <sup>th</sup> Street South AB 990 Birmingham, AL 35294-0001				<b>8. PERFORMING ORGANIZATION REPORT NUMBER</b>	
<b>9. SPONSORING / MONITORING AGENCY NAME(S) AND ADDRESS(ES)</b> Air Force Research Laboratory 3550 Aberdeen Ave SE Kirtland AFB, NM 87117-5776				<b>10. SPONSOR/MONITOR'S ACRONYM(S)</b> AFRL/RDLTS	
				<b>11. SPONSOR/MONITOR'S REPORT NUMBER(S)</b> AFRL-RD-PS-TR-2013-0003	
<b>12. DISTRIBUTION / AVAILABILITY STATEMENT</b> Approved for public release: distribution unlimited. 377ABW-2013-0458; 4 Jun 13. Government Purpose Rights.					
<b>13. SUPPLEMENTARY NOTES</b>					
<b>14. ABSTRACT</b> Middle-infrared (mid-IR) laser sources are in great demand for a variety of applications including molecular spectroscopy, non-invasive medical diagnostics, laser medical scalpel that make use of the ability of the laser to tune in and out of the strong absorption band of liquid water, industrial process control, environmental monitoring, atmospheric sensing and free space communication, oil prospecting, and numerous defense related applications such as infrared aircraft countermeasures, monitoring of munitions disposal, stand-off detection of explosion hazards, eye safe seekers for smart munitions and cruise missiles, covert communications systems, and injection seeding of high power chemical (e.g. HF) lasers.					
<b>15. SUBJECT TERMS</b> Mid-IR Laser, Chalcogenide					
<b>16. SECURITY CLASSIFICATION OF:</b>			<b>17. LIMITATION OF ABSTRACT</b>  SAR	<b>18. NUMBER OF PAGES</b>  126	<b>19a. NAME OF RESPONSIBLE PERSON</b> Leanne J. Henry
<b>a. REPORT</b> Unclassified	<b>b. ABSTRACT</b> Unclassified	<b>c. THIS PAGE</b> Unclassified			<b>19b. TELEPHONE NUMBER (include area code)</b>

Standard Form 298 (Rev. 8-98)

This page intentionally left blank.

## TABLE OF CONTENTS

Section	Page
1.0 SUMMARY .....	1
2.0 INTRODUCTION .....	2
2.1 Fabrication of $\text{Ni}^{2+}$ ; $\text{Fe}^{2+}$ ; and $\text{Co}^{2+}$ doped ZnSe/ZnS samples .....	4
2.2 Fabrication of $\text{Ni}^{2+}$ and $\text{Co}^{2+}$ doped ZnSe/ZnS samples .....	8
2.3 Fabrication of $\text{Fe}^{2+}$ and $\text{Co}^{2+}$ doped ZnSe/ZnS samples .....	10
3.0 THEORETICAL ANALYSIS OF ENERGY LEVEL DIAGRAMS RADIATIVE AND NONRADIATIVE TRANSITIONS OF 3D GROUP IONS (FE, NI, CO) IN II-VI CRYSTALS .....	11
3.1 Spectra of iron group ions in tetrahedral semiconductors of $\text{A}^{\text{II}}\text{B}^{\text{VI}}$ type .....	11
3.1.1 Red shift of iron group ions spectra in tetrahedral semiconductors of $\text{A}^{\text{II}}\text{B}^{\text{VI}}$ type .....	11
3.1.2 Piezoelectric effects in tetrahedral semiconductors of the $\text{A}^{\text{II}}\text{B}^{\text{VI}}$ type .....	12
3.2 The peculiarities of spectra of the iron group ions in $\text{A}^{\text{II}}\text{B}^{\text{VI}}$ semiconductor Crystals .....	12
3.3 State classification of electronic configuration $3d^n$ .....	13
3.3.1 States of total angular momentum J of spin-orbital interaction .....	14
3.3.2 States of $\text{Fe}^{2+}$ ( $3d^6$ electronic configuration) .....	14
3.3.3 States of $\text{Co}^{2+}$ ( $3d^7$ electronic configuration) .....	16
3.3.4 States of $\text{Ni}^{2+}$ ( $3d^8$ electronic configuration) .....	18
3.4 Theory .....	19
3.4.1 Formula for calculation of the matrix elements of crystal field potential .....	21
3.4.2 Formula for calculation of the matrix elements of electrostatic interaction .....	21
3.4.3 Formula for calculation of the matrix elements of spin-orbit interaction .....	22
3.5 Intensities of transitions between states of $3d^n$ electronic configurations .....	22
3.5.1 Formula for calculation of the intensity matrix elements for transitions in iron group ions .....	24
3.6 Simulation of the absorption spectra of $d^n$ electronics configurations .....	24
3.7 Oscillator strength and decay time of $d^n$ electronic configurations .....	24

3.8	Spectroscopic diagrams of $\text{Co}^{2+}$ in tetrahedral crystals of the type $\text{A}^{\text{II}}\text{B}^{\text{VI}}$ .....	26
3.8.1	Diagrams of energy states of $\text{Co}^{2+}$ ions in tetrahedral semiconductors of the type $\text{A}^{\text{II}}\text{B}^{\text{V}}$ .....	26
3.9	Spectra of $\text{Co}^{2+}$ in CdS.....	28
3.9.1	Absorption spectra of $\text{Co}^{2+}$ in CdS .....	28
3.9.2	Luminescence spectra of $\text{Co}^{2+}$ in CdS .....	29
3.10	Absorption spectra from excited states of $(^4\text{F})^4\text{F}_2$ multiplet .....	33
3.11	Selection rule for the transitions $(^4\text{F})^4\text{A}_2 - (^4\text{F})^4\text{F}_2$ and $(^4\text{F})^4\text{A}_2 - (^4\text{F})^4\text{F}_1$ .....	33
3.12	Configuration coordinate model of transition dynamics .....	34
3.13	Spectra of $\text{Co}^{2+}$ in ZnSe .....	34
3.13.1	Absorption spectra of $\text{Co}^{2+}$ in ZnSe.....	34
3.14	Configuration coordinate model of the transition dynamics of $\text{Co}^{2+}$ in ZnSe .....	38
3.15	Spectral properties of $\text{Ni}^{2+}$ in ZnSe.....	41
3.15.1	$\text{Ni}^{2+}$ energy state diagrams in tetrahedral semiconductors of the type $\text{A}^{\text{II}}\text{B}^{\text{VI}}$ .....	41
3.16	Configuration coordinate model for the transition dynamics of $\text{Ni}^{2+}$ in ZnSe .....	46
3.17	Spectral properties of $\text{Fe}^{2+}$ in ZnSe.....	49
3.18	Configuration coordinate model of transition dynamics of $\text{Fe}^{2+}$ in ZnSe.....	53
3.19	Overview of experimental data in literature .....	55
3.19.1	Experimental spectra of $\text{Co}^{2+}$ in ZnSe .....	55
3.19.2	Experimental spectra of $\text{Ni}^{2+}$ in ZnSe.....	66
3.19.3	Experimental spectra of $\text{Fe}^{2+}$ in ZnSe.....	67
4.0	SPECTROSCOPIC CHARACTERIZATION OF TM DOPED SAMPLES .....	70
4.1	Concentration and temperature quenching of the mid-IR photoluminescence in Fe:ZnSe and Fe:ZnS crystals.....	70
4.1.1	Fe:ZnSe crystal .....	71
4.1.2	Fe:ZnS crystal .....	75

4.2	Cobalt doped samples .....	77
4.3	Spectroscopic characterization of $\text{Co}^{2+}$ and $\text{Fe}^{2+}$ co-doped samples .....	81
4.4	Energy transfer in $\text{Co:Fe:ZnS/ZnSe}$ crystals under excitation at 720 nm .....	83
4.5	Spectroscopic characterization of $\text{Co}^{2+}$ and $\text{Ni}^{2+}$ co-doped samples .....	87
5.0	LASER CHARACTERIZATION OF TM DOPED SAMPLES .....	89
5.1	Lasing of $\text{Co:Fe:ZnSe}$ and $\text{Co:Fe:ZnS}$ crystals via effective $\text{Co} \rightarrow \text{Fe}$ energy transfer under 1.56 $\mu\text{m}$ wavelength excitation .....	89
5.2	Lasing of $\text{Co:Fe:ZnSe}$ and $\text{Co:Fe:ZnS}$ crystals via effective $\text{Co} \rightarrow \text{Fe}$ energy transfer under 0.76 $\mu\text{m}$ wavelength excitation .....	93
5.3	Preliminary laser experiments with $\text{Co:ZnSe/ZnS}$ crystals .....	95
5.4	$\text{Co:ZnSe}$ saturable absorber for passively Q-switched $\text{Er:YAG}$ lasers .....	97
6.0	CONCLUSIONS .....	101
7.0	REFERENCES .....	102
	APPENDIX .....	104
A.1	Program for calculation of the spectra of $\text{TM}^{2+}:\text{ZnSe}$ .....	104
A.2	Matrix of energy interactions for iron group ions .....	104
A.3	Program for calculating eigenvectors and eigenvalues of the total matrix A .....	107
A.4	Program for calculating the matrix elements of the second and fourth order tensor operators $U_2$ and $U_4$ .....	107
	LIST OF SYMBOLS, ABBREVIATIONS, AND ACRONYMS .....	109

## LIST OF FIGURES

Figure	Page
1 Plasma Sputtering System at IPG Photonics Corporation .....	6
2 Topography of iron films having different thicknesses as measured by AFM (each grid represents 500nm).....	6
3 A) Calibration curve for the deposition monitor used for cobalt deposition during magnetron sputtering at 1000 nm; B) percentage transmission of a cobalt thin film deposited on a microscopic glass slide vs thin-film thickness.....	7
4 Cobalt doped ZnSe (7×3.1×50 mm <sup>3</sup> ) samples after annealing for 7 days at 950°C .....	7
5 Nickel – Cobalt co-doped ZnSe and ZnS samples.....	10
6 Diagram of the matrix describing the 3d <sup>6</sup> electronic configuration of Fe <sup>2+</sup> .....	16
7 Diagram of the matrix for the 3d <sup>7</sup> electron configuration of Co <sup>2+</sup> .....	18
8 Diagram of the matrix for the 3d <sup>8</sup> electronic configuration of Ni <sup>2+</sup> .....	19
9 Energy level diagram Co <sup>2+</sup> , showing $E/Dq$ and $E/F_{22}$ versus the relative parameters $F_{22}/Dq$ and $Dq/F_{22}$ when $\xi_{3d} = 0$ .....	26
10 The energy levels of Co <sup>2+</sup> in the relative units $E/F_{22}$ versus the relative parameter $Dq/F_{22} = 0-0.5$ at $\xi_{3d} = 0$ .....	27
11 The energy levels (with labels) of Co <sup>2+</sup> in the relative units $E/F_{22}$ versus the relative parameter $Dq/F_{22} = 0.3-0.5$ at $\xi_{3d} = 0$ .....	27
12 The Absorption spectra of both the $\sigma$ - and $\pi$ - transitions of Co <sup>2+</sup> in CdS in the 2000 – 14000 cm <sup>-1</sup> energy region .....	28
13 The absorption spectra of both the $\sigma$ - and $\pi$ - transitions of Co <sup>2+</sup> in CdS in the 2000 – 6000 cm <sup>-1</sup> energy region.....	29
14 The luminescence spectra of Co <sup>2+</sup> in CdS in the 0-6000 cm <sup>-1</sup> region upon excitation of the $\pi$ - transition ${}^4A_2-{}^4F_1$ .....	30
15 The luminescence spectra in the 0-6000 cm <sup>-1</sup> region of Co <sup>2+</sup> in CdS upon excitation of the $\sigma$ - transition ${}^4A_2-({}^4F){}^4F_1$ .....	30
16 Luminescence spectra in the 8000-14000 cm <sup>-1</sup> region of Co <sup>2+</sup> in CdS upon excitation of the $\pi$ -transition ${}^4A_2-({}^4P){}^4F_1$ .....	31



17	Luminescence spectra in the 8000-14000 $\text{cm}^{-1}$ region of $\text{Co}^{2+}$ in CdS upon excitation of the $\sigma$ -transition $^4\text{A}_2-(^4\text{P})^4\text{F}_1$ .....	31
18	Luminescence spectra in the 0-18000 $\text{cm}^{-1}$ region of $\text{Co}^{2+}$ in CdS upon excitation of the $\pi$ - transition $^4\text{A}_2-(^2\text{D})^2\text{F}_2$ .....	32
19	Luminescence spectra in the 0-18000 $\text{cm}^{-1}$ region of $\text{Co}^{2+}$ in CdS upon excitation of the $\sigma$ - transition $^4\text{A}_2-(^2\text{D})^2\text{F}_2$ .....	32
20	Absorption spectra of $\text{Co}^{2+}$ in CdS for both the $\sigma$ - and $\pi$ - transitions from the excited states of the $(^4\text{F})^4\text{F}_2$ multiplet .....	33
21	Absorption spectra in the 3000-42000 $\text{cm}^{-1}$ range of $\text{Co}^{2+}$ in ZnSe .....	36
22	Absorption spectra in the 3000-24000 $\text{cm}^{-1}$ range of $\text{Co}^{2+}$ in ZnSe .....	37
23	Absorption spectra in the 11000-15000 $\text{cm}^{-1}$ range of $\text{Co}^{2+}$ in ZnSe .....	37
24	Energy level diagram of $\text{Co}^{2+}$ in ZnSe versus the relative configuration coordinate $r/R$ ..	38
25	Diagram of the energy levels of the $^4\text{A}_2(\Gamma_8)$ state (the lower curve) and the $^4\text{T}_2(\Gamma_8)$ state (the upper curve) of $\text{Co}^{2+}$ in ZnSe versus the relative configuration coordinate $x = r/R$ ...	39
26	Diagram of the energy levels $^4\text{A}_2(\Gamma_8)$ (the lower curve) and $^4\text{T}_2(\Gamma_8)$ (the upper curve) of $\text{Co}^{2+}$ in ZnSe with the energies and configuration coordinate values for the absorption and emission transitions .....	39
27	Diagram of the energy levels $^4\text{A}_2(\Gamma_8)$ (the lower curve) and $^4\text{T}_2(\Gamma_8)$ (the upper curve) of $\text{Co}^{2+}$ in ZnSe along with the photon and phonon parameters of the absorption and emission transitions.....	40
28	Diagram of $\text{Ni}^{2+}:\text{ZnSe}$ energy levels (in $\text{cm}^{-1}$ ).....	42
29	$\text{Ni}^{2+}:\text{ZnSe}$ energy level diagram of $E/Dq$ and $E/F_{22}$ versus the relative parameter values $F_{22}/Dq$ and $Dq/F_{22}$ with no spin-orbital interaction $\xi_{3d} = 0$ .....	42
30	Energy levels of $\text{Ni}^{2+}:\text{ZnSe}$ in terms of $E/F_{22}$ versus the relative parameter $Dq/F_{22} = 0.25-0.5$ at $\xi_{3d} = 0$ .....	43
31	The energies $E$ and oscillator strength $f$ for the absorption spectra of $\text{Ni}^{2+}$ in ZnSe for the total polarization .....	44
32	The energies $E$ and oscillator strength $f$ of the absorption spectra of $\text{Ni}^{2+}$ in in ZnSe for the $\pi$ and $\sigma$ polarizations .....	45

33	Oscillator strength $f$ of the theoretical spectra for the $\pi$ polarization (the upper red line) and the experimental spectra (the lower black line) in arbitrary units [14] for the absorption of $\text{Ni}^{2+}$ in ZnSe in the wavelength region 0 – 2500 nm .....	45
34	Oscillator strength $f$ of the theoretical spectra for the $\pi$ polarization (the upper red line) and the experimental spectra (the lower black line) in arbitrary units [14] of absorption of $\text{Ni}^{2+}$ in ZnSe in the wavelength $\lambda$ region of 1000 – 2600 nm .....	46
35	Energy level diagram of $\text{Ni}^{2+}$ in ZnSe versus the relative configuration coordinate $r/R$ ..	46
36	Energy level diagram of $\text{Ni}^{2+}$ in ZnSe versus the relative configuration coordinate $r/R$ ..	47
37	Energy levels of $\text{Ni}^{2+}$ in ZnSe for various $k_g$ (quoted in the Fig. as “diag”) and $k$ values.	48
38	The energy $E$ and oscillator strength $f$ of the absorption spectra of $\text{Fe}^{2+}$ in ZnSe for the $\pi$ and $\sigma$ polarizations as well as the total polarization .....	51
39	Energy $E$ and oscillator strength $f$ of the absorption spectra of $\text{Fe}^{2+}$ in ZnSe for the total polarization .....	51
40	Energy $E$ and oscillator strength $f$ of the absorption spectra of $\text{Fe}^{2+}$ in ZnSe for the $\sigma$ polarization .....	52
41	Energy $E$ and oscillator strength $f$ of the absorption spectra of $\text{Fe}^{2+}$ in ZnSe for the $\pi$ polarization .....	52
42	The oscillator strength $f$ of the theoretical spectra for the $\sigma$ polarization (the upper, red line) and the experimental data in arbitrary units (the lower, black line) [15] for the absorption spectra in the 2500 – 3500 nm region of $\text{Fe}^{2+}$ in ZnSe .....	53
43	Diagram of the energy levels of $\text{Fe}^{2+}$ in ZnSe versus the relative configuration coordinate $r/R$ .....	54
44	Diagram of the energy levels: $^5\text{D}_4(\Gamma_8)$ (the lower curve) , $^5\text{D}_3(\Gamma_8)$ and $^3\text{H}_6(\Gamma_8)$ (the upper curve) of $\text{Fe}^{2+}$ in ZnSe versus the relative configuration coordinate $x = r/R$ .....	54
45	Low energy experimental absorption spectra of $\text{Co}^{2+}$ in ZnSe: orange line, – ref. [1]; green line, (b) – ref. [1]; black line, (c) – ref. [16]; and violet line, (d) – ref. [17] .....	56
46	Infrared absorption spectra in the 5000-7500 $\text{cm}^{-1}$ spectral region of $\text{Co}^{2+}$ in ZnSe: orange line, (a) – ref. [1]; green line, (b) – ref. [1]; black line, – ref. [16]; violet line, (d) – ref. [17]; cyan line, (e) – ref. [18] .....	56

47	Infrared absorption spectra in the 5000-7500 $\text{cm}^{-1}$ spectral region of $\text{Co}^{2+}$ in ZnSe: orange line, (a) – ref. [1]; green line, (b) – ref. [1]; together with curve fits (black dashes).....	57
48	Infrared absorption spectra in the 5000-7500 $\text{cm}^{-1}$ spectral region of $\text{Co}^{2+}$ in ZnSe .....	58
49	Infrared absorption spectra in the 5000-7500 $\text{cm}^{-1}$ spectral range of $\text{Co}^{2+}$ in ZnSe .....	58
50	Spectra of $\text{Co}^{2+}$ in ZnSe from 11200 to 11800 $\text{cm}^{-1}$ from ref. [17] (blue line) and the Gaussian fit to the peak (green line) .....	59
51	Spectra of $\text{Co}^{2+}$ in ZnSe from 1180 to 12800 $\text{cm}^{-1}$ : (c), black line – experimental data from ref. [16] and its fit (red line); (d) – experimental data from ref. [17] (blue line) and it's fit (green line) .....	59
52	Absorption spectra of $\text{Co}^{2+}$ in ZnSe in visible region: orange line, (a) – ref. [1]; green line, (b) – ref. [1]; black line, (c) – ref. [16]; violet line, (d) – ref. [17], blue line (d') – data from ref. [17] multiplied by a factor of 0.1; cyan line, (e) – ref. [18] .....	60
53	Absorption spectra of $\text{Co}^{2+}$ in ZnSe in the visible region from 13000 to 14600 $\text{cm}^{-1}$ : experimental data from ref. [17] (blue line) and it's fit by the sum of five Gaussian functions (green line) .....	61
54	Absorption spectra of $\text{Co}^{2+}$ in ZnSe in visible region from 14400 to 15400 $\text{cm}^{-1}$ : experimental data from ref. [17] (violet line) and it's fit by the sum of two Gaussian function (green line) .....	61
55	Absorption spectra of $\text{Co}^{2+}$ in ZnSe from 15500 to 18000 $\text{cm}^{-1}$ : experimental data from ref. [16] (black line) and it's fit by the sum of three Gaussian functions (red line) .....	62
56	Absorption spectra of $\text{Co}^{2+}$ in ZnSe from 15500 to 18000 $\text{cm}^{-1}$ : experimental data from ref. [17] (violet line) and its fit by the sum of three Gaussian functions (green line).....	62
57	High-energy absorption spectra of $\text{Co}^{2+}$ in ZnSe from 18750 to 20750 $\text{cm}^{-1}$ : orange line, (a) – ref. [1]; black line, (c) – ref. [16]; violet line, (d) – ref. [17].....	63
58	Absorption spectra of $\text{Co}^{2+}$ in ZnSe from 18500 to 21000 $\text{cm}^{-1}$ : orange line – experimental data taken from ref. [1]; green line – the mathematical fit. ....	64
59	Absorption spectra of $\text{Co}^{2+}$ in ZnSe from 18500 to 21000 $\text{cm}^{-1}$ : black line – experimental data taken from ref. [16]; red line – the mathematical fit .....	64
60	Absorption spectra of $\text{Co}^{2+}$ in ZnSe from 18500 to 21000 $\text{cm}^{-1}$ : violet line – experimental data taken from ref. [17]; green line – the mathematical fit .....	65

61	Luminescence spectra of $\text{Co}^{2+}$ in ZnSe over the 2500 to 2800 $\text{cm}^{-1}$ spectral range (experimental data were taken from paper [16]).....	65
62	Absorption spectra of $\text{Ni}^{2+}$ in ZnSe over the 500 to 2500 $\text{cm}^{-1}$ spectral range, taken from reference [14] .....	66
63	Absorption spectra of $\text{Ni}^{2+}$ in ZnSe from 4000 to 14000 $\text{cm}^{-1}$ taken from reference [14] in $\text{cm}^{-1}$ (black line) and its mathematical fit (red line).....	66
64	Absorption and luminescence spectra of $\text{Fe}^{2+}$ in ZnSe taken from [2] .....	67
65	Absorption spectra of $\text{Fe}^{2+}$ in ZnSe over the 2600 to 4000 $\text{cm}^{-1}$ spectral range: (a) ref. [2], (b) – ref. [1], (c) – ref. [19] .....	68
66	Absorption spectra of $\text{Fe}^{2+}$ in ZnSe over the 2600 to 4100 $\text{cm}^{-1}$ spectral range: experiment from ref. [2] – black line and its fit – red line .....	69
67	Luminescence spectra of $\text{Fe}^{2+}$ in ZnSe, blue line – ref. [19], black line – ref. [2]. Spectroscopic characterization of TM doped samples.....	69
68	Room temperature absorption (A) and emission (B) spectra of Fe:ZnSe (solid line) and Fe:ZnS (dashed line) crystals.....	70
69	Luminescence kinetics of Fe:ZnSe samples having iron concentrations of: $C = 0.1 \times 10^{18} \text{ cm}^{-3}$ (i,ii); $C = 5 \times 10^{18} \text{ cm}^{-3}$ (iii,iv); and $C = 86 \times 10^{18} \text{ cm}^{-3}$ (v,vi); at $T = 20^\circ\text{K}$ (ii;iv;vi), $T = 110^\circ\text{K}$ (iii,v); and $T = 120^\circ\text{K}$ (i) .....	72
70	Luminescence spectra of Fe:ZnSe samples at $T = 14^\circ\text{K}$ having the following iron concentrations: (i) $C_{\text{Fe}} = 112 \times 10^{18} \text{ cm}^{-3}$ and (ii) $C_{\text{Fe}} = 5 \times 10^{18} \text{ cm}^{-3}$ ; and an Fe:ZnS sample at $T = 14^\circ\text{K}$ having an iron concentration of: (iii) $C_{\text{Fe}} = 5 \times 10^{18} \text{ cm}^{-3}$ .....	72
71	Luminescence lifetime versus temperature for Fe:ZnSe (+ - $C_{\text{Fe}} = 0.1 \times 10^{18} \text{ cm}^{-3}$ ) and for Fe:ZnS crystals ( $\times$ - $C_{\text{Fe}} = 3 \times 10^{18} \text{ cm}^{-3}$ , $\square$ - $C_{\text{Fe}} = 73 \times 10^{18} \text{ cm}^{-3}$ ); curves describing the fits are described in the text .....	73
72	Configuration coordinate diagram for linear coupling [23].....	73
73	A) Luminescence kinetics of Fe:ZnSe samples with different iron concentrations: (1)- $C_{\text{Fe}} = 0.1 \times 10^{18} \text{ cm}^{-3}$ ; (2)- $C_{\text{Fe}} = 14 \times 10^{18} \text{ cm}^{-3}$ ; (3)- $C_{\text{Fe}} = 45 \times 10^{18} \text{ cm}^{-3}$ ; and (4)- $C_{\text{Fe}} = 112 \times 10^{18} \text{ cm}^{-3}$ , B) same luminescence kinetics with an expanded time scale.....	74
74	Average relaxation time of the $^5\text{T}_2 \rightarrow ^5\text{E}$ transition versus iron concentration in Fe:ZnSe samples measured at room temperature (dashed line shows least square fit using	

	eq. 70) .....	75
75	A) Luminescence kinetics of Fe:ZnS samples having different iron concentrations: (1)- $C_{Fe} = 3 \times 10^{18} \text{ cm}^{-3}$ ; (2)- $C_{Fe} = 15 \times 10^{18} \text{ cm}^{-3}$ ; (3)- $C_{Fe} = 73 \times 10^{18} \text{ cm}^{-3}$ at $T = 220^\circ\text{K}$ ; B) Luminescence kinetics of Fe:ZnS having an iron concentration of $C_{Fe} = 3 \times 10^{18} \text{ cm}^{-3}$ at different temperatures (4-6) .....	76
76	Experimental setup and results for the measurement of the cobalt concentration gradient in a Co:ZnSe crystal.....	77
77	The absorption cross-sections of $\text{Co}^{2+}$ ions in ZnSe crystals on the $^4\text{A}_2(\text{F}) \rightarrow ^4\text{T}_2(\text{P})$ ( <i>Upper  part</i> ); $^4\text{A}_2(\text{F}) \rightarrow ^4\text{T}_1(\text{F})$ ( <i>Middle part part</i> ); and $^4\text{A}_2(\text{F}) \rightarrow ^4\text{T}_2(\text{F})$ transitions ( <i>Bottom part</i> ).79	
78	The absorption cross-sections of $\text{Co}^{2+}$ ions in ZnS crystals on the $^4\text{A}_2(\text{F}) \rightarrow ^4\text{T}_2(\text{P})$ ( <i>Upper  part</i> ); $^4\text{A}_2(\text{F}) \rightarrow ^4\text{T}_1(\text{F})$ ( <i>Middle part</i> ); and $^4\text{A}_2(\text{F}) \rightarrow ^4\text{T}_2(\text{F})$ transitions ( <i>Bottom part</i> )......80	
79	Diagram of the energy transfer mechanisms in the iron, chromium and cobalt co-doped II-VI materials.....	81
80	Transmission and absorption spectra of Co:Fe:ZnSe crystal.....	82
81	Absorption spectra of Co:Fe:ZnS crystals .....	82
82	Time resolved spectra of Co:Fe:ZnSe under $1.56 \mu\text{m}$ excitation with a $4 \mu\text{s}$ gate-width and $0 \mu\text{s}$ (i) and $40 \mu\text{s}$ time delays (ii) .....	83
83	Absorption spectrum of the Co:Fe:ZnS sample measured at RT (red curve) and $T = 16^\circ\text{K}$ (blue curve) .....	84
84	Kinetics of the mid-IR photoluminescence of Co:Fe:ZnS (curve i); Co:ZnS (curve ii); and Fe:ZnS (curve iii) at $T = 20^\circ\text{K}$ and $77^\circ\text{K}$ under $\text{Co}^{2+}$ excitation (curve i and ii) at $720 \text{ nm}$ ; and under $\text{Fe}^{2+}$ excitation (curve iii) at $2.8 \mu\text{m}$ .....	85
85	Kinetics of mid infrared photoluminescence of Co:Fe:ZnSe (curve i); Co:ZnSe (curve ii); and Fe:ZnS (curve iii) under $760 \text{ nm}$ excitation of $\text{Co}^{2+}$ (curves i and ii); and $2.8 \mu\text{m}$ excitation of $\text{Fe}^{2+}$ excitation (curve iii) at $T = 14^\circ\text{K}$ .....	86
86	Mid-infrared luminescence spectra of iron and cobalt co-doped ZnSe crystals at $T = 14^\circ\text{K}$ under $760 \text{ nm}$ excitation.....	87
87	Absorption spectra of the Co:Ni:ZnSe (black curve), and Co:ZnSe (red curve) crystals..87	
88	RT photo-luminescence spectra of Ni:Co:ZnS (black curve) and Co:ZnS (red curve) samples.....	88

89	Mid-infrared luminescence spectra of iron and cobalt doped crystals at $T = 14^\circ\text{K}$ .....	90
90	A) Mid-infrared luminescence spectra of a Co:Fe:ZnS crystal under different pump energies at $T=14^\circ\text{K}$ , B) photoluminescence kinetics of a Co:Fe:ZnS crystal for different pump energies below (red) and above (pink) the laser threshold .....	92
91	Mid-infrared luminescence spectra of the Co:Fe:ZnSe crystal for different pump energies under 760 nm excitation at $T = 14^\circ\text{K}$ measured below and above the laser threshold.....	93
92	A) Co:Fe:ZnSe crystal photoluminescence kinetics for different pump energies at an excitation wavelength of 760 nm measured below and above the laser threshold at $14^\circ\text{K}$ . B) Difference between the measured kinetics and the normalized luminescence signals measured below the laser threshold .....	94
93	Middle-Infrared PL spectra of Co:ZnS and Co:ZnSe .....	95
94	PL kinetics of Co:ZnS and Co:ZnSe crystals .....	96
95	Laser Experimental Setup .....	96
96	Experimental setup.....	97
97	Transmission spectrum of the Co:ZnS crystal .....	98
98	Output power of a passively Q-switched and CW Er:YAG laser.....	98
99	Train of output pulses from a passively Q-switched Er:YAG laser at a pump power of 7.4 W .....	99
100	Output energy (A) and repetition rate (B) of the passively Q-switched Er:YAG laser .....	99
101	Temporal profile of the passively Q-switched output pulses.....	100

## LIST OF TABLES

Table	Page
1 Thickness, $h$ , of the transition metal film required for fabrication of a mm sample with an average concentration of $N_{TM} = 10^{19} \text{ cm}^{-3}$ .....	5
2 Summary of fabricated Ni:Co:Fe:ZnS/Se samples .....	8
3 States and their degeneration numbers for the $3d^6$ electronic configuration of $\text{Fe}^{2+}$ .....	15
4 States and the degeneration numbers for the $3d^7$ electronic configuration of $\text{Co}^{2+}$ .....	17
5 States and the degeneration numbers for the $3d^8$ electron configuration of $\text{Ni}^{2+}$ .....	19
6 Dependence of the ratio of the cross section for the two transitions $G = Q(^4A_2 - (^4F)^4F_2)/Q(^4A_2 - (^4F)^4F_1)$ on the ratio of the two main intensity parameters $B_4/B_2$ .....	34
7 Energy levels and oscillator strengths of the absorption spectra transitions of $\text{Co}^{2+}$ in ZnSe (with polarizations $\pi$ , $\sigma$ , and total polarization).....	35
8 Parameters associated with the minimum in the configuration curves (CC) as well as the absorption energies from the $(^4F)^4T_2$ ground state with $k = 0.2$ .....	38
9 Strengths ( $f \cdot 10^7$ ) of the absorption transitions ( $J-J'$ ) of $\text{Ni}^{2+}$ in ZnSe for both $\pi$ and $\sigma$ polarizations as well as the total polarization (transitions occur from the base state $J = (^3F)(^3T_1)^3A_1$ ).....	43
10 Minimum values of the energies of the states and the associated configuration coordinates $r/R$ calculated with the following electron phonon parameters: $k_g = 2000 \text{ cm}^{-1}$ and $k = 0.2$ 47	
11 Values for the energy levels of $\text{Ni}^{2+}$ in ZnSe for the minimas of the Relative configuration coordinate $x_0$ of the two states $(^3F)(^3T_1)A_1$ , and $(^3F)(^3T_2)T_1$ .....	49
12 Absorption spectra of $\text{Fe}^{2+}$ ZnSe for both the total and ( $\pi$ and $\sigma$ ) polarizations (transitions occur from the base state $(^5D_4)^5A_1$ ) .....	49
13 Equations of the energy levels of $\text{Fe}^{2+}$ in ZnSe versus the relative configuration coordinate $x = r/R$ when $k = 0.2$ . Also shown are the coordinates $x_0$ and values of the energy minimums $E(x_0)$ for these levels .....	55
14 Values of the energy levels of $\text{Fe}^{2+}$ in ZnSe for the minima of the relative configuration coordinate $x_0$ of the three states $^5D_4$ , $^5D_4$ , and $^3H_6$ .....	55
15 Summary of the spectroscopic characteristics of Co:ZnSe and Co:ZnS .....	78
16 Properties of Co:ZnSe and Co:ZnS samples studied by pumping with a 739.7 nm laser .95	





## 1.0 SUMMARY

The technology of high optical quality gain elements based on Co, Ni, and Fe doped ZnSe and ZnS crystals promising for room-temperature lasing was developed. Multiple crystals have been fabricated and studied via absorption and photoluminescence spectroscopy. For the first time lasing was achieved on Fe ions in ZnS and ZnSe crystals co-doped with Co via effective Co-Fe energy transfer. For the first time Co:ZnS crystals were successfully used for passive Q-switching of continuous wave (CW) pumped Er:YAG 1645 nm lasers.

The matrices for calculating the energy and intensity of electric dipole transitions of  $3d^n$  electronic configurations were created. These matrices enabled calculation of the energies, oscillator strengths, and lifetimes for any transition of the  $3d^n$  ( $n = 2, 3, 4, 6, 7, 8$ ) electronic configuration. This thereby enabled calculation of the absorption, luminescence, luminescence excitation spectra, as well as the absorption spectra for transitions from the excited states. Within the energy and intensity matrices, the configuration curves of the energy levels are developed by approximating the zero- and fourth-order crystal field parameters with parabolic dependences on the vibration amplitudes. The configuration diagrams of  $\text{Co}^{2+}$ ,  $\text{Fe}^{2+}$ , and  $\text{Ni}^{2+}$  ions are calculated for different cases of anharmonicity. The proposed theory is applied to analyze the experimental spectra of  $\text{Co}^{2+}$ ,  $\text{Fe}^{2+}$ , and  $\text{Ni}^{2+}$  ions in ZnSe available in the literature and yields good agreement between the experimental and modeled spectra.

## 2.0 INTRODUCTION

Middle-infrared (mid-IR) laser sources are in great demand for a variety of applications including molecular spectroscopy, non-invasive medical diagnostics, laser medical scalpels that make use of the ability of the laser to tune in and out of the strong absorption band of liquid water, industrial process control, environmental monitoring, atmospheric sensing and free space communication, oil prospecting, and numerous defense related applications such as infrared aircraft countermeasures, monitoring of munitions disposal, stand-off detection of explosion hazards, eye safe seekers for smart munitions and cruise missiles, covert communications systems, and injection seeding of high power chemical (e.g. HF) lasers.

Mid-IR wavelengths are typically generated using relatively complex nonlinear optical conversion techniques or by means of direct generation in hetero-junction lead-salt, antimonide, or quantum cascade semiconductor lasers featuring limited output power and tuning range. Impurity doped crystalline vibronic lasers, having a gain bandwidth up to 50% of central wavelength, constitute another viable route for broadly tunable mid-IR coherent sources. Among them are transition metal ( $\text{TM}^{2+}$ , e.g.,  $\text{Cr}^{2+}$  or  $\text{Fe}^{2+}$ ) doped binary (e.g.,  $\text{ZnSe}$ ,  $\text{ZnS}$ ,  $\text{CdSe}$ ,  $\text{CdS}$ ,  $\text{ZnTe}$ ) and ternary (e.g.,  $\text{CdMnTe}$ ,  $\text{CdZnTe}$ ,  $\text{ZnSSe}$ ) chalcogenide crystals that represent a relatively new class of solid state gain media with strong, ultra-broad absorption and emission bands in the mid-IR range of the optical spectrum. In 1996, Scientists from the Lawrence Livermore National Laboratory [1] were the first to show that among the different types of crystalline gain materials,  $\text{TM}^{2+}$  doped wide bandgap II-VI semiconductor crystals could be very special for mid-IR lasing:

- An important feature of II-VI compounds is their tendency to crystallize as tetrahedral coordinated structures, as opposed to the typical octahedral coordination at the dopant site. Tetrahedral coordination results in a smaller crystal field splitting which has the effect of placing the dopant transitions further into the infrared (IR).
- Another key feature of these materials is that the heavy anions in the crystal enable a very low energy optical phonon cutoff which makes them transparent in a wide spectral region while decreasing the efficiency of non-radioactive decay. This gives the promise of a high fluorescence yield at room temperature (RT).

Active interest in transition metal (TM) doped II-VI compounds inspired by [1] was explained by the fact that these media are close mid-IR analogs of titanium-doped sapphire (Ti-S) in terms of spectroscopic and laser characteristics. It was anticipated that  $\text{TM}^{2+}$  doped chalcogenides would lase in the mid-IR with a great variety of possible modes of oscillation, similar to what has been found with the Ti-S laser. Indeed, optically pumped RT lasers based on  $\text{Cr}:\text{ZnS}$ ,  $\text{Cr}:\text{ZnSe}$ ,  $\text{Cr}:\text{Cd}_{1-x}\text{Mn}_x\text{Te}$ ,  $\text{Cr}:\text{CdSe}$ , and  $\text{Fe}:\text{ZnSe}$  crystals providing access to the 2-3 and 3.8-5  $\mu\text{m}$  spectral regions with high (up to 70%) efficiency, multi-Watt-level output powers, tunability in excess of 1000 nm, and narrow spectral linewidth (<20 MHz), have been reported by several groups (see e.g. reviews [2, 3, 4, 5, 6] and references therein). Arguably these lasers represent nowadays the simplest and the most cost-effective route for high power, broadly tunable lasing in the 2-3 and 3.8-5  $\mu\text{m}$  wavelength ranges.

There are still several challenges to be overcome in the development of affordable high power tunable TM:II-VI lasers continuously covering the 2-5  $\mu\text{m}$  spectral range. Among them are the:

- 1) Lack of developed gain materials capable of effectively operating over the currently unavailable 3-4  $\mu\text{m}$  spectral range.
- 2) Lack of convenient pump sources for 3.8-5  $\mu\text{m}$  Fe:ZnSe lasers
- 3) Lack of TM:II-VI gain materials pumped by the radiation of readily available neodymium or ytterbium lasers.

To address the enumerated challenges, the following research objectives are proposed:

1. Development of the technology associated with high optical quality gain elements based on  $\text{Co}^{2+}$  doped ZnSe crystals that are promising for room-temperature lasing over the 3-4  $\mu\text{m}$  spectral range.
2. Fabrication and characterization of  $\text{Co}^{2+}$ :ZnSe experimental samples that lase over the 3-4  $\mu\text{m}$  spectral range under Er-fiber, 808 nm diode, and/or Alexandrite laser pumping.
3. Development of the technology associated with high optical quality gain elements based on  $\text{Ni}^{2+}$  co-doped  $\text{Co}^{2+}$ :ZnSe crystals which are promising for room-temperature lasing over the 3-4  $\mu\text{m}$  spectral range via energy transfer from Ni to Co.
4. Fabrication and characterization of  $\text{Ni}^{2+}$  co-doped  $\text{Co}^{2+}$ :ZnSe experimental samples for 3-4  $\mu\text{m}$  lasing under Yb-fiber and/or Nd laser pumping.
5. Development of the technology associated with high optical quality gain elements based on  $\text{Co}^{2+}$  co-doped Fe:ZnSe crystals which are promising for room-temperature lasing over the 3.8-5.2  $\mu\text{m}$  spectral range via energy transfer from Co to Fe.
6. Fabrication and characterization of  $\text{Co}^{2+}$  co-doped  $\text{Fe}^{2+}$ :ZnSe experimental samples for 3.8-5.2  $\mu\text{m}$  lasing under Er-fiber and/or 808 nm diode laser pumping via energy transfer from Co to Fe.

The specific tasks to be performed at the University of Alabama Birmingham (UAB) in collaboration with the A.M. Prokhorov General Physics Institute of the Russian Academy of Science business representative towards realization of the proposed objectives are as follows:

**Task 1.** Analyze and evaluate the basic parameters relevant for fabrication of TM doped ZnSe crystals by post-growth thermal diffusion of Ni, Co, and Fe ions in high optical quality IR window-grade polycrystalline ZnSe. (UAB)

**Task 2.** Theoretically analyze energy level diagrams, radiative and nonradiative transitions of 3d group ions (Fe, Ni, Co) in II-VI crystals. (Subcontractor – Prokhorov General Physics Institute (GPI), RAS business representative).

**Task 3.** Fabricate 25 ZnSe samples having a concentration series of Ni, Co, Fe, Ni-Co, and Co-Fe concentrations ranging from  $10^{18}$  to  $5 \times 10^{19} \text{ cm}^{-3}$  (5 samples for each dopant). (UAB)

**Task 4.** Perform temperature dependent absorption, photoluminescence (PL), time resolved PL, and microscopic characterization of fabricated crystals. (UAB)

**Task 5.** Perform decay kinetic analysis of optical energy migration and concentration quenching in fabricated samples. (UAB)

**Task 6.** Theoretically analyze the optical excitation energy transfer schemes, sensitization as well as up and down energy conversion. Evaluate the multipolarity, dimensionality, macro-efficiency and micro-efficiency. Derive an analytical solution and perform a Monte Carlo simulation. **(GPI)**

**Task 7.** Using information from tasks 1-6 fabricate and optically characterize the following:

- a) Co:ZnSe gain elements optimal for 3-4  $\mu\text{m}$  lasing under Er-fiber laser excitation. **(UAB)**
- b) Co:ZnSe gain elements optimal for 3-4  $\mu\text{m}$  lasing under 808 nm diode laser excitation. **(UAB)**
- c) Co:ZnSe gain elements optimal for 3-4  $\mu\text{m}$  lasing under gain-switched alexandrite laser excitation. **(UAB)**

**Task 8.** Using information from tasks 1-6 fabricate and optically characterize:

- a)  $\text{Ni}^{2+}$  co-doped  $\text{Co}^{2+}$ :ZnSe gain elements optimal for 3-4  $\mu\text{m}$  lasing under Yb-fiber laser excitation. **(UAB)**
- b)  $\text{Ni}^{2+}$  co-doped  $\text{Co}^{2+}$ :ZnSe gain elements optimal for 3-4  $\mu\text{m}$  lasing under gain switched Nd:YAG laser excitation. **(UAB)**

**Task 9.** Using information from tasks 1-6 fabricate and optically characterize:

- a)  $\text{Co}^{2+}$  co-doped Fe:ZnSe gain elements optimal for 3.8-5.2  $\mu\text{m}$  lasing under Er-fiber laser excitation. **(UAB)**
- b)  $\text{Co}^{2+}$  co-doped Fe:ZnSe gain elements optimal for 3.8-5.2  $\mu\text{m}$  lasing under 808 nm diode laser excitation. **(UAB)**
- c)  $\text{Co}^{2+}$  co-doped Fe:ZnSe gain elements optimal for 3.8-5.2  $\mu\text{m}$  lasing under alexandrite laser excitation. **(UAB)**

**Task 10.** Laser characterization of gain elements fabricated in tasks 7-9. **(UAB and Kirtland AFB)**

In the final report, the results of our research are summarized in the following chapters:

- Chapter 2: Fabrication of II-VI crystals with a concentration series of dopants (tasks: 1,3,7,8,9)
- Chapter 3: Theoretical analysis of energy level diagrams, radiative and nonradiative transitions of 3d group ions (Fe, Ni, Co) in II-VI crystals (tasks: 2,6)
- Chapter 4: Spectroscopic characterization of TM doped samples (tasks: 4,5,7,8,9)
- Chapter 5: Laser characterization of TM doped samples (tasks: 10) Fabrication of II-VI crystals with concentration series of dopants

## **2.1 Fabrication of $\text{Ni}^{2+}$ ; $\text{Fe}^{2+}$ ; and $\text{Co}^{2+}$ doped ZnSe/ZnS samples**

Post-growth thermal diffusion from a metal film on the surface of a crystal was used to fabricate Co, Ni, Fe and Cr co-doped ZnSe/ZnS samples for this project. This technique utilizes thermally activated diffusion of transition metal ions into II-VI crystals. The typical experimental

procedure includes the following technological operations:

- Blank crystal preparation
- Deposition of the metal film on the crystal surface
- Sealing of a sample into a quartz ample
- Annealing of the sample in an oven at high temperature (800-1200°C)

The average TM concentration in a sample can be controlled by the specific thickness of the TM thin film deposited on the crystal surface. The thicknesses of a TM thin film required for a concentration of  $N_{TM} = 10^{19} \text{ cm}^{-3}$  in a 1 mm thick crystal are presented in the Table 1. The density associated with bulk metals was used for these calculations.

**Table 1. Thickness,  $h$ , of the transition metal film required for fabrication of a 1 mm sample with an average concentration of  $N_{TM} = 10^{19} \text{ cm}^{-3}$**

<b>Metal</b>	<b><math>h(\text{nm})</math></b>
Cr	120
Fe	118
Co	110
Ni	110

Values for the diffusion coefficients of TM ions in II-VI hosts reported by several research groups were not similar with differences up to several orders of magnitude. These differences may have resulted from several parameters which are difficult to control. These parameters include: the polycrystalline structure of the II-VI host; the surface crystal preparation, as well as sublimation of the metal and host during thermal diffusion. However, based on data reported on the thermal diffusion coefficients for different transition metal ions under similar experimental conditions, one could consider the following to be the rank of the TM diffusion coefficients in a ZnSe host at  $T = 946^\circ\text{C}$  from lowest to highest:

$$D(\text{Fe}) < D(\text{Co}) < D(\text{Ni}) < D(\text{Cr})$$

IPG Photonics Corporation has developed a commercial fabrication procedure for quantitative (accuracy of pre-assigned concentration of dopant is better than 3%), fast thermo-diffusion of chromium ions in ZnSe crystals with suppressed sublimation of the anion and cation sublattices. The resulting fabricated crystals are uniformly doped through a thickness of up to 7 mm and feature a low scattering loss of 1-2 % per cm for samples with a Cr concentration of  $5 \times 10^{18} \text{ cm}^{-3}$ . The diffusion procedures for other TM ions were based on the one developed for chromium.

Metal targets for deposition of thin films having purity better than 99.95% were purchased from the Kurt J. Lesker Company. Transition metal films were deposited by either thermal evaporation or magnetron sputtering in a vacuum chamber. Thermal diffusion was then carried out in sealed vacuumed ( $\sim 10^{-5}$  Torr) ampoules at temperatures between 900-1100°C over a period of 7-20 days. The most reliable and controllable results for deposition of the metal film were obtained with the use of magnetron sputtering (see Figure.1).

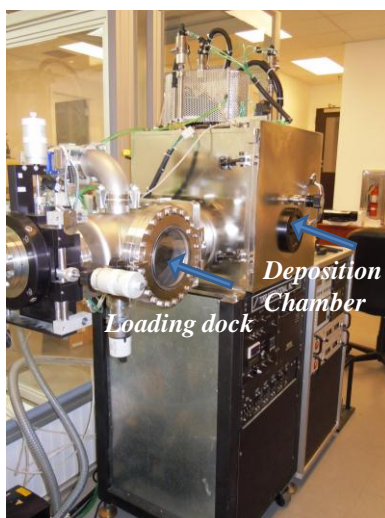


**Figure 1. Plasma Sputtering System at IPG Photonics Corporation**

The thin film deposition rate and the substrate temperature have been optimized by choosing parameters which provide the most uniform thin film thickness according to Atomic Force Microscopy (AFM) data, and the best film adhesion determined by the stability of the film during rapid heating of the crystal under vacuum conditions. The thickness deposition monitor has been calibrated with Atomic Force Microscopy (AFM, Park Systems) to enable a precise determination of the thickness of the TM film on ZnSe. For the deposition monitor calibration, several microscopic slides having different thicknesses of deposited TM films were prepared.

Their thicknesses were measured by the AFM. As shown in Figure 2, the thickness of the iron films in the left and the right samples were estimated to be 1020 and 1305 nm, respectively.

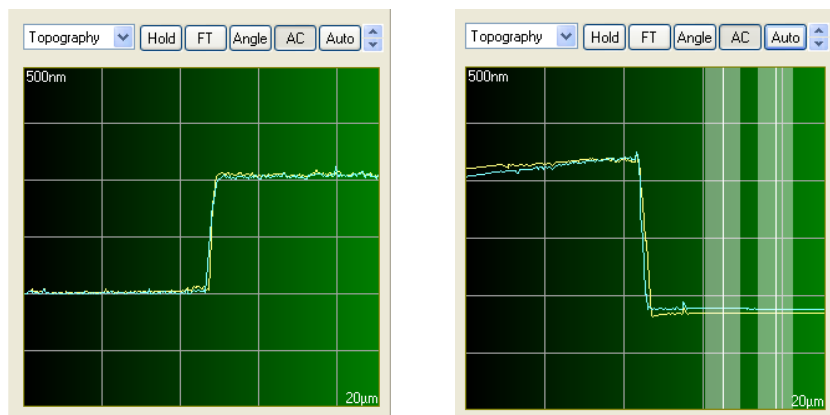


**Figure 2. Topography of iron films having different thicknesses as measured by AFM (each grid represents 500 nm)**

In addition to the calibration of thin film deposition by AFM, the percentage transmission of deposited metal films was also measured. Figure 3 shows the percentage transmission of a cobalt thin film deposited on a glass slide measured at a wavelength of 1000 nm as a function of the film thickness. As one can see from Figure 3, this simple method can be used to determine the thickness of a film lying between 5-125 nm, post deposition.

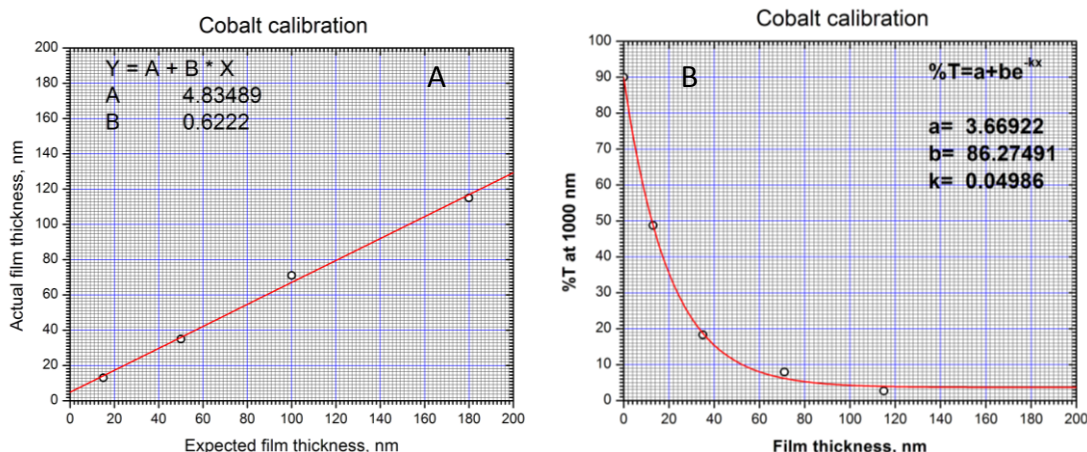


**Figure 3. A) Calibration curve for the deposition monitor used for cobalt deposition during magnetron sputtering at 1000 nm; B) percentage transmission of a cobalt thin film deposited on a microscopic glass slide vs thin-film thickness.**

The fabricated samples were then sealed in separate quartz ampoules at  $10^{-5}$  Torr and annealed at 900-1000°C for 7-24 days. Figure 4 shows a photo of cobalt doped ZnSe samples annealed for 7 days at 950°C. For spectroscopic characterization, a number of ZnSe samples having a concentration series of Ni, Co, and/or Fe, ranging from  $10^{18}$  to  $5 \times 10^{19} \text{ cm}^{-3}$  were prepared. Several samples having different iron concentrations were fabricated from the initial Co:ZnS/Co:ZnSe crystals. Study of the luminescence quenching of cobalt (nickel) photoluminescence in iron co-doped crystals should provide information on the energy transfer rate from the Co (Ni) co-dopants to the Fe ions.

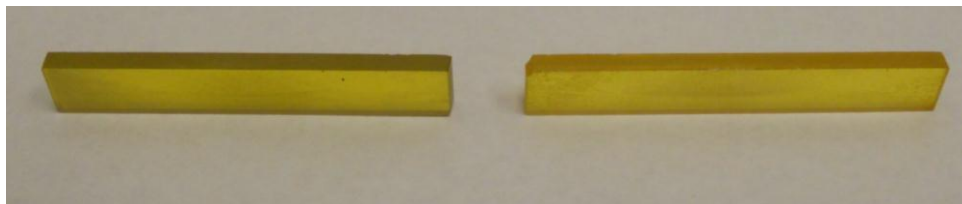


**Figure 4. Cobalt doped ZnSe ( $7 \times 3.1 \times 50 \text{ mm}^3$ ) samples after annealing for 7 days at 950°C.**

## 2.2 Fabrication of Ni<sup>2+</sup> and Co<sup>2+</sup> doped ZnSe/ZnS samples

Initially, ZnS and ZnSe samples were doped with the cobalt impurity by using a thermo-diffusion method which is described in detail in a previous report [7]. The Co:ZnSe/ZnS samples were then co-doped with nickel. The nickel co-doped samples were also fabricated by thermal diffusion from a metal film deposited by the Plasma Sputtering System at IPG Photonics Corporation. A summary of all the fabricated samples is shown in Table 2 and pictures of the samples 811-60/62/63/64/65 are shown in Figure 5 below.

**Table 2. Summary of fabricated Ni:Co:Fe:ZnS/Se samples**

Crystal #	Mat.	Thicknes s [cm]	Width [cm]	Length [cm]		Concentration calculated (Ni) [cm <sup>-3</sup> ]	Ann.time (at 950°C for Ni)	Concentration calculated (Co) [cm <sup>-3</sup> ]
811-59	ZnS	0.33	0.64	5.7		3.00×10 <sup>18</sup>	10 days	1.00×10 <sup>18</sup>
811-60	ZnS	0.33	0.64	5.74		3.00×10 <sup>18</sup>	10 days	3.00×10 <sup>18</sup>
811-61	ZnS	0.33	0.64	3.15		3.00×10 <sup>18</sup>	10 days	3.00×10 <sup>19</sup>
811-62	ZnS	0.32	0.64	5.73		3.00×10 <sup>18</sup>	10 days	1.00×10 <sup>20</sup>
811-63	ZnS	0.33	0.64	2.74		3.00×10 <sup>19</sup>	10 days	3.00×10 <sup>19</sup>
811-64	ZnSe	0.33	0.75	4.3		3.00×10 <sup>18</sup>	10 days	1.00×10 <sup>18</sup>
811-65	ZnSe	0.3	0.75	4.2		3.00×10 <sup>18</sup>	10 days	3.00×10 <sup>18</sup>
811-66	ZnSe	0.35	0.75	2.34		3.00×10 <sup>18</sup>	10 days	3.00×10 <sup>19</sup>
811-67	ZnSe	0.33	0.75	4.33		3.00×10 <sup>18</sup>	10 days	1.00×10 <sup>20</sup>
811-68	ZnSe	0.33	0.74	2.26		3.00×10 <sup>19</sup>	10 days	3.00×10 <sup>19</sup>
Crystal #	Mat.	Thicknes s [cm]	Width [cm]	Length [cm]		Concentration calculated (Co) [cm <sup>-3</sup> ]		Concentration calculated (Fe) [cm <sup>-3</sup> ]
811-1a	ZnS	0.25	0.55	0.96		5.560×10 <sup>17</sup>		
811-1b	ZnS	0.25	0.55	0.96		6.007×10 <sup>17</sup>		
811-1c	ZnS	0.25	0.55	0.96		8.261×10 <sup>17</sup>		
811-1d	ZnS	0.25	0.55	0.96		7.824×10 <sup>17</sup>		
811-1e	ZnS	0.28	0.24	0.55		2.908×10 <sup>17</sup>		
811-1f	ZnS	0.28	0.24	0.55		1.596×10 <sup>17</sup>		
811-1g	ZnS	0.28	0.24	0.55		2.674×10 <sup>17</sup>		
811-1h	ZnS	0.28	0.24	0.55		1.846×10 <sup>17</sup>		



811-1k	ZnS	0.28	0.24	0.55		$8.826 \times 10^{17}$		
811-44a	ZnS	0.28	0.24	0.55		$1.949 \times 10^{19}$		$2.86 \times 10^{18}$
811-44b	ZnS	0.28	0.24	0.55		$1.885 \times 10^{19}$		$2.86 \times 10^{18}$
811-44c	ZnS	0.28	0.24	0.55		$1.943 \times 10^{19}$		$3.66 \times 10^{18}$
811-14d	ZnS	0.25	0.6	1.7	Brewster	$1.781 \times 10^{19}$		
811-14e	ZnS	0.25	0.6	3.7	Brewster	$1.760 \times 10^{19}$		
811-15a	ZnS	0.25	0.6	2.6	Brewster	$2.017 \times 10^{19}$		
811-15b	ZnS	0.25	0.6	2.6	Brewster	$1.884 \times 10^{19}$		
811-43a	ZnS	0.28	0.24	0.55		$1.841 \times 10^{19}$		$2.88 \times 10^{18}$
811-43b	ZnS	0.28	0.24	0.55		$1.806 \times 10^{19}$		$2.76 \times 10^{18}$
811-43c	ZnS	0.28	0.24	0.55		$1.954 \times 10^{19}$		$8.49 \times 10^{18}$
811-17a	ZnSe	0.24	0.55	0.96		$1.388 \times 10^{18}$		
811-17b	ZnSe	0.24	0.55	0.96		$1.407 \times 10^{18}$		
811-17c	ZnSe	0.28	0.24	0.55		$9.055 \times 10^{17}$		
811-17d	ZnSe	0.28	0.24	0.55		$1.105 \times 10^{18}$		
811-29	ZnSe	0.24	0.68	4	Brewster	$2.150 \times 10^{19}$		
811-28	ZnSe	0.24	0.68	3	Brewster	$2.080 \times 10^{19}$		
811-58a	ZnSe	0.29	0.245	0.6		$1.307 \times 10^{19}$		$3.14 \times 10^{18}$
811-58b	ZnSe	0.28	0.24	0.6		$1.360 \times 10^{19}$		$4.56 \times 10^{18}$
811-57a	ZnSe	0.28	0.24	0.6		$1.312 \times 10^{19}$		$2.82 \times 10^{18}$
811-57b	ZnSe	0.28	0.24	0.6		$1.325 \times 10^{19}$		$5.82 \times 10^{18}$
<b>Crystal #</b>	<b>Mat.</b>	<b>Thick [cm]</b>	<b>Width [cm]</b>	<b>Length [cm]</b>		<b>Concentration calculated(Co) [cm<sup>-3</sup>]</b>	<b>Ann.time for Fe@ 1000C</b>	<b>Concentration calculated(Fe) [cm<sup>-3</sup>]</b>
F1109	ZnSe	1.0	0.69	0.13			17days	$112 \times 10^{18}$
A2109	ZnSe	0.82	0.8	0.35			17days	$0.1 \times 10^{18}$
A1309	ZnSe	0.71	0.67	0.13			17days	$38 \times 10^{18}$
J3110	ZnS	0.84	0.75	0.5			66 days	$1.1 \times 10^{18}$
J3210	ZnS	0.84	0.75	0.5			66 days	$3.0 \times 10^{18}$
J3310	ZnS	0.84	0.75	0.5			66 days	$5.0 \times 10^{18}$
J3510	ZnS	0.84	0.75	0.5			66 days	$23 \times 10^{18}$
J2110	ZnSe	0.77	0.75	0.21		$6 \times 10^{18}$	16 days	0

J4110	ZnS	1.0	0.54	0.12		$6 \times 10^{18}$	16days	0
J4110	ZnS	1.0	0.54	0.12		$6 \times 10^{18}$	16 days	0
J4210	ZnS	1.0	0.54	0.12		$6 \times 10^{18}$	36 days	$0.5 \times 10^{18}$
J4310	ZnS	1.0	0.54	0.12		$6 \times 10^{18}$	36days	$7.0 \times 10^{18}$
J4410	ZnS	1.0	0.54	0.13		$6 \times 10^{18}$	36days	$10 \times 10^{18}$
J2110	ZnSe	0.77	0.75	0.21		$6 \times 10^{18}$	16days	0
J2310	ZnSe	0.77	0.75	0.2		$6 \times 10^{18}$	36 days	$8.5 \times 10^{18}$
J2410	ZnSe	0.77	0.75	0.2		$6 \times 10^{18}$	36 days	$12.4 \times 10^{18}$
J2510	ZnSe	0.77	0.75	0.2		$6 \times 10^{18}$	36 days	$18.7 \times 10^{18}$

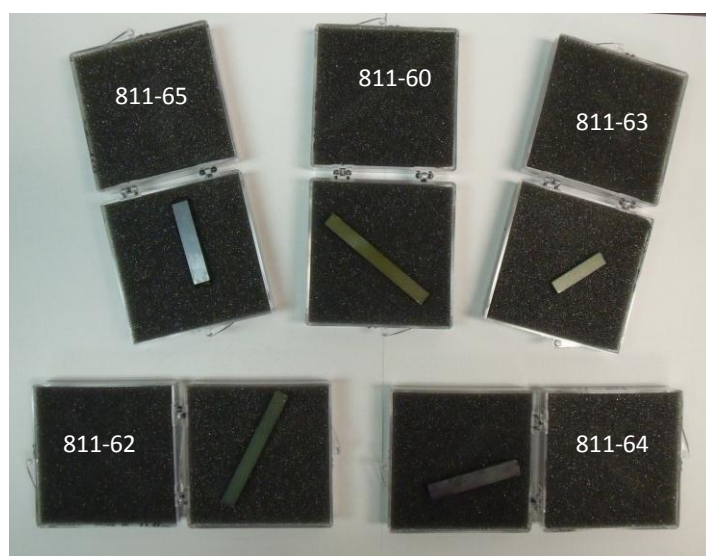


**Figure 5. Nickel – Cobalt co-doped ZnSe and ZnS samples**

### 2.3 Fabrication of $\text{Fe}^{2+}$ and $\text{Co}^{2+}$ doped ZnSe/ZnS samples

Co-doped Co:Fe:ZnSe and Co:Fe:ZnS polycrystals having a dimension of  $10 \times 10 \times 1.2 \text{ mm}^3$  were fabricated using a two-stage thermo-diffusion method. The initial thermal diffusion of cobalt ions was performed in a sealed quartz ampoule at  $10^{-5}$  Torr at an annealing temperature of  $1000^\circ\text{C}$  for 16 days. The thermal diffusion of iron ions was performed at the same temperature for 20 days. The diffusion procedure was optimized to provide for a uniform distribution of iron over the crystal thickness ( $\sim 1 \text{ mm}$ ).

A controlled thermal diffusion of iron ions was used to fabricate co-doped Co:Fe:ZnSe and Co:Fe:ZnS samples with an Fe concentration range of  $8.5\text{--}19 \times 10^{18} \text{ cm}^{-3}$  and  $0.5\text{--}10 \times 10^{18} \text{ cm}^{-3}$ , respectively, while the cobalt concentration was maintained at the  $6.4 \times 10^{18} \text{ cm}^{-3}$  level for all crystals.

### 3.0 THEORETICAL ANALYSIS OF ENERGY LEVEL DIAGRAMS, RADIATIVE AND NONRADIATIVE TRANSITIONS OF 3D GROUP IONS (FE, NI, CO) IN II-VI CRYSTALS

We are interested in the energy states that fall within the forbidden zone of II-VI materials since they can be pumped and manifest themselves. The purpose of the modeling in this section is to delineate the desired energy states (that fit in the forbidden zone) and the other energy states that cannot be pumped.

#### 3.1 Spectra of iron group ions in tetrahedral semiconductors of the $A^{II}B^{VI}$ type

Usually, the spectral properties of the dopant ions of the iron group are investigated in dielectric crystals with a high crystal field potential and a large splitting of energy levels. As a result, transitions between the primary levels of absorption and luminescence lay in the visible or near infrared wavelength range.

The future increase in the data traffic of telecommunication optical fiber networks calls for the creation of lasers and wideband amplifiers in new spectral ranges. In particular, for the second and third telecommunication transmission windows (around 1.3 and 1.5  $\mu\text{m}$ ), there are no effective active sources that are compatible with common silica-based telecommunication fibers. The advancement in the area of longer wavelengths (1.7-3.5  $\mu\text{m}$  range) is limited by the absorption properties of quartz glass. This drives the utilization of a different type of environment such as telluride ( $\text{TeO}_2$ ) or AgBr and AgCl materials for the middle infrared. In addition, powerful light sources in the 1.7-3.5  $\mu\text{m}$  spectral range can be frequency doubled into the 0.85-1.75  $\mu\text{m}$  spectral range for scientific, technological and medical purposes.

The basic problem of modern quantum and nano electronics is the creation of lasers and amplifiers in semiconductor materials. Creation of such devices would involve a symbiosis of the spectral properties of the active centers and the basic semiconductor material. Taken together with the ability of a semiconductor material to carry a current, new possibilities in both quantum and nano electronics can be opened up.

Among the large set of possible semiconductor materials, those materials having an ionic bond and a wide forbidden zone of the type  $A^{II}B^{VI}$  are of specific interest. Thus, it is necessary to verify that the absorption levels of an active center align with the width of the forbidden zone so that sufficient pumping can be obtained. The intricate problem of the interaction between the electrons of the active center with the electrons of the valence zone and the conduction band demands special research.

##### 3.1.1 Red shift of iron group ion spectra in tetrahedral semiconductors of the $A^{II}B^{VI}$ type.

In crystals, ions belonging to the iron group may occupy the coordinate centers of polyhedrons having orbits with coordinate numbers  $k = 4, 6$ , and  $8$ . The crystal field parameter  $Dq$  (as well as its sign) depends on the number of coordinates associated with the orbits:

$$Dq(6) > 0, \quad (1)$$

$$Dq(4) = -\frac{2}{3} Dq(6) \quad (2)$$

Semiconductor crystals having tetrahedral orbits with  $k = 4$  have a weaker crystal field (CF) potential than dielectric crystals having octahedral orbits with  $k = 6$ .

In crystals of the  $A^{II}B^{VI}$  type, ions of the iron group are bivalent and have a smaller CF potential and  $Dq$  value than they would have if they were in the trivalent state in an octahedral dielectric crystal. Thus, in  $A^{II}B^{VI}$  semiconductor crystals doped with ions of the iron group having tetrahedral orbits, a “red shift” should be exhibited with the transition energies of the absorption and fluorescence spectra of the ions of iron group characterized by lower frequencies.

The parameter  $Dq$ , which depends on the charge of an electron, has a different sign for an iso electron-hole configuration. Thus, the  $Dq$  parameter for the hole configuration of ions of the iron group in tetrahedral semiconductor crystals is positive. It is also positive for the case of an iso-electron configuration of ions in octahedral crystals of a dielectric:

$$Dq(d^{10-n}, k=4) > 0 \quad Dq(d^n, k=6) > 0 \quad (3)$$

The parameters of the electronic electrostatic interaction depend on the charge squared and have the same sign for both the electron and hole configurations. The spin-orbital interaction parameter is linearly proportional to the sign of electronic charge, so it changes sign when the hole configuration is changed. In summary, the parameters of crystal field ( $Dq$ ), the electrostatic interaction ( $F_2$  and  $F_4$ ) and the spin-orbital interaction ( $\xi_{3d}$ ) of ions of the iron group in semiconductor crystals of the  $A^{II}B^{VI}$  type should have the following signs:

$$Dq > 0, F_2 > 0, F_4 > 0, \xi_{3d} < 0. \quad (4)$$

### 3.1.2 Piezoelectric effects in tetrahedral semiconductors of the $A^{II}B^{VI}$ type.

The tetrahedral symmetry of the group  $T_d$  (no center of symmetry) defines the existence of a piezoelectric effect in semiconductor materials. This allows one to use an external electric field to control the spectral properties of the laser transitions. It is difficult to expect a large influence from an external electric field on the frequencies of laser transitions. However, mechanical deformations caused by the piezoeffect can generate odd harmonics of a crystal field in the environment of an active center thereby changing the intensity of the transitions. The result will be a redistribution of the transition intensities on the Stark levels that will depend on the size and direction of the applied electric field.

## 3.2 The peculiarities of spectra of iron group ions in $A^{II}B^{VI}$ semiconductor crystals

The spectra of iron group ions are usually analyzed by means of Tanabe-Sugano (TS) diagrams. However, they have limited application for tetrahedral centers in semiconductor crystals.

TS theory is based on the strong (intermediate) field case, where the energy of interaction with the crystal neighborhood is greater than the electrostatic interaction between electrons. In this case, the 3d energy configuration of iron group ions in crystal fields having  $O_h$  group symmetry is split into e and  $t_2$  levels,  $3d^n \Rightarrow e^m t_2^{n-m}$ . In semiconductor crystals of the  $A^{II}B^{VI}$  type, the crystal field interaction potential is smaller than the electrostatic interaction and there is therefore little use in considering configurations on the basis of strong CF state functions. Using this basis, the quantum numbers of a free atom and the representations of the orthogonal rotation symmetry

group  $O_3$  are meaningless. In this case, quantum numbers are replaced by the indices of the irreducible representations of a point symmetry group for which there is no possibility of defining exact quantum numbers and performing analytical calculations algebraically. As a result, the powerful tool of angular momentum summation theory is rendered useless.

TS matrices make use of the Racah parameters of the electrostatic interaction which are linear combinations of the Slater parameters. The Racah parameters arise from the internal symmetry of the free atom states. They facilitate the diagonalization of the matrices of the electrostatic interaction. In TS theory, combinations of the Racah parameters are used in the basis of the strong CF wavefunctions. When studying the dependence of the electrostatic interaction parameters on covalent effects in semiconductor crystals, it is better to use the Slater parameters which have an explicit form for the radial wave function of the atom rather than a combination of the radial wave functions of various orders.

In tetrahedral semiconductors, the symmetry group is of the type  $T_d$  or  $T$ . While even parts of the crystal potential for the groups  $O_h$  and  $(T_d, T)$  do not change, the types of irreducible representations do. Non-diagonal elements (absent in crystal fields of  $O_h$  symmetry) appear as shown in [8]. In addition, odd terms (of the third order) of the crystal potential combine with an odd electro-dipole operator to form an even operator allowing an electro-dipole transition. That is why TS matrices and diagrams are of little use for evaluating oscillator strengths.

Another point is that relativistic effects must be taken into account for ions of the  $3d^n$  configuration in  $A^{II}B^{VI}$  semiconductors. The effects are manifested by the spin-orbit (SO) interaction, which can be as strong as the CF interaction in the semiconductor crystal field. The SO interaction splits the crystal field levels and is seen in the band structure of transition metals. When considering the spin-orbit interaction, one needs to employ the double symmetry group state classification which cannot be accomplished using a basis comprised of the strong field wave functions of the TS theory.

In addition, the actual symmetry of a crystal field can be described by lower symmetry groups of the trigonal or rhombic type. This requires additional CF terms that are outside the framework of the TS matrices.

All of the above calls for the development of a new theory and the construction of new matrices for the  $3d^n$  configuration in order to take into account all of the effects. To address this need, a theory and concrete formulas to enable an analytical calculation of the matrix elements of the electrostatic interaction, spin-orbit interaction, and crystal field interactions in the basis set of wave-functions with the quantum numbers  $l = 2$ ,  $SLJm_j$  will be developed. We will work to enable the calculation of all matrices in one mathematical program without referring to any external data for the 3j, 6j, and 9j genealogical coefficients. Thus, the program will compute all of the matrices of the  $3d^n$  configuration states.

### 3.3. State classification of the electronic configuration $3d^n$

Classification of the states of the  $3d^n$  electron configuration is based on reduction of the irreducible representations of the following groups:

$$\begin{aligned}
U_{4l+2} &\supset SU_2 \times R_{2l+1} \supset SU_2 \times R_3 \\
\{1^n\} &\supset [S] \times [W] \supset [S] \times [L],
\end{aligned} \tag{5}$$

where  $U_{4l+2}$  is a unitary group having a dimension of  $4l+2$  that represents all the states of the anti-symmetric representation  $\{1^n\}$  which describe an electron in the  $l^n$  configuration,  $W$  is a representation of the orthogonal group  $R_{2l+1}$  having a dimension of  $2l+1$ , and  $S$  and  $L$  are the spin and orbital quantum numbers representing the spin and orbital groups  $SU_2$  and  $R_3$ , respectively. Ions in the  $d^n$  configuration with  $l = 2$ , are represented by the unitary group  $U_{10}$  and the orthogonal group  $R_5$  of five-dimensional space. As an example, one-electron in the  $d^1$  configuration with  $l = 2$  is characterized by the following series:

$$\begin{aligned}
U_{10} &\supset SU_2 \times R_5 \supset SU_2 \times R_3 \\
\{1\} &\supset [1] \times [1] \supset [1] \times [2] = {}^2 D.
\end{aligned} \tag{6}$$

All states of any  $d^n$  configuration can therefore be obtained by reducing one anti-symmetric state  $\{1^n\}$  of the  $U_{10}$  group as in (6).

### 3.3.1 States of the total angular momentum $J$ of the spin-orbital interaction.

Due to the spin – orbital interaction, the spin  $S$  and the angular momentum  $L$  are mixed with a total angular momentum  $J$  being obtained. The spin  $S$  and the orbital momentum  $L$  of a given electronic state give the total angular momentum  $J$  according to the following rules for the multiplication of the irreducible representation of the orthogonal rotation group  $R_3$ :  $L \times S = L+S, L+S-1 \dots |L-S|$ . For example, the  ${}^3F$  state has the following multiplets:  $S=1, L=3$  and  $J=4, 3$ , and  $2$ , which results in the  ${}^3F_4, {}^3F_3, {}^3F_2$  spin – orbit states. Tables of the states of the three electron configurations  $d^n$  where  $n = 6, 7$ , and  $8$  with the values of  $J$  are presented below.

### 3.3.2 States of $Fe^{2+}$ ( $3d^6$ electronic configuration).

The  $Fe^{2+}$  ion has a  $3d^6$  electronic configuration and all its states are determined by the following representations:

$$\begin{aligned}
U_{10} &\supset SU_2 \times R_5 \supset SU_2 \times R_3 \\
\{1^6\} &\supset [2] \times [10] \supset [2] \times [2] = {}^5 D \\
&\quad [1] \times [11] \supset [1] \times [1] = {}^3 P^{(1)} \\
&\quad \quad \supset [1] \times [3] = {}^3 F^{(1)} \\
&\quad [1] \times [21] \supset [1] \times [1] = {}^3 P^{(2)} \\
&\quad \quad [1] \times [2] = {}^3 D \\
&\quad \quad [1] \times [3] = {}^3 F^{(2)} \\
&\quad \quad [1] \times [4] = {}^3 G \\
&\quad \quad [1] \times [5] = {}^3 H \\
&\quad [0] \times [00] \supset [0] \times [0] = {}^1 S^{(1)} \\
&\quad [0] \times [22] \supset [0] \times [0] = {}^1 S^{(2)} \\
&\quad [0] \times [20] \supset [0] \times [2] = {}^1 D^{(1)} \\
&\quad [0] \times [22] \supset [0] \times [2] = {}^1 D^{(2)} \\
&\quad \quad [0] \times [3] = {}^1 F \\
&\quad [0] \times [20] \supset [0] \times [4] = {}^1 G^{(1)} \\
&\quad [0] \times [22] \supset [0] \times [4] = {}^1 G^{(2)} . \\
&\quad \quad [0] \times [6] = {}^1 I
\end{aligned} \tag{7}$$

The resulting states are designated as  ${}^{2S+1}L^{(p)}$ . The upper-left index denotes the spin (S) degeneration and is represented by number  $2S+1$ . The upper-right index (p) = (1) or (2) distinguishes duplicate states having the same quantum numbers. The orbital quantum numbers are denoted by the letter L with the following correspondence:

	S	P	D	F	G	H	I
Quantum number L	0	1	2	3	4	5	6

The orbital degeneration is equal to  $2L+1$ . The degeneration numbers of the  ${}^{2S+1}L$  states are equal to  $(2S+1)(2L+1)$ . Finally, the states and their degeneration numbers for the  $3d^6$  electron configuration of  $Fe^{2+}$  are given in Table 3.

**Table 3. States and their degeneration numbers for the  $3d^6$  electronic configuration of  $Fe^{2+}$**

State $3d^6$	${}^5D$	${}^3P^{(1)},$ ${}^3P^{(2)}$	${}^3F^{(1)},$ ${}^3F^{(2)}$	${}^3D$	${}^3G$	${}^3H$	${}^1S^{(1)},$ ${}^1S^{(2)}$	${}^1D^{(1)},$ ${}^1D^{(2)}$	${}^1F$	${}^1G^{(1)},$ ${}^1G^{(2)}$	${}^1I$
L-degeneration	5	3	7	5	9	11	1	5	7	9	13
Total degeneration	25	$9 \times 2$	$21 \times 2$	15	27	33	$1 \times 2$	$5 \times 2$	7	$9 \times 2$	13
Angular momentum J	4, 3, 2, 0	2, 1, 0	4, 3, 2	3, 2, 1	5, 4, 3	6, 5, 4	0	2	3	4	6

The states with quantum numbers S and L are obtained by taking into account only the electrostatic interaction between the electrons.

Graphically, a diagram of the full matrix of the electronic configurations  $d^6$  is presented in Figure 6. The white spaces correspond to elements of the matrix which are zero while the black spaces correspond to different nontrivial values which depend in a complex way on the parameters of all the interaction types.

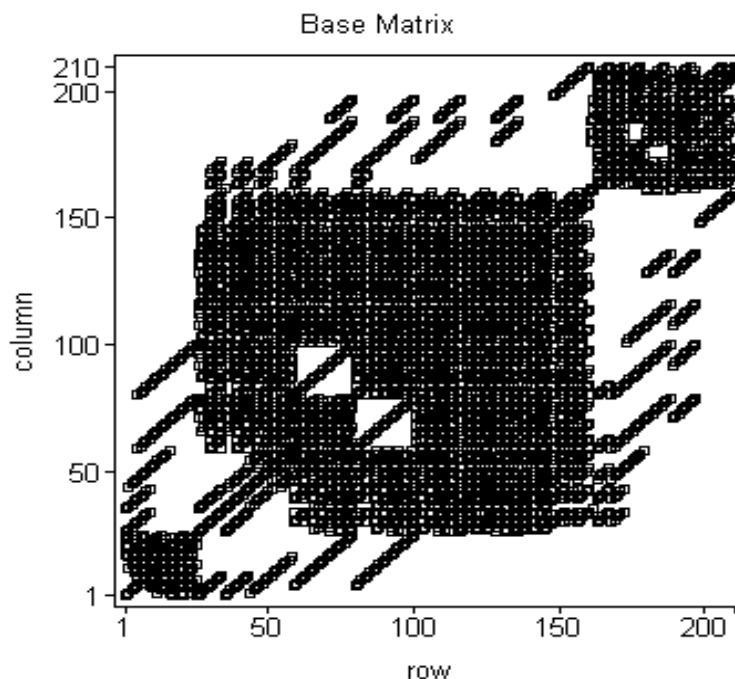


**Figure 6. Diagram of the matrix describing the  $3d^6$  electronic configuration of  $\text{Fe}^{2+}$ . The total number of states is 210.**

### 3.3.3 States of $\text{Co}^{2+}$ ( $3d^7$ electron configuration).

$\text{Co}^{2+}$  ion has a  $3d^7$  electronic configuration and all its states are determined by the following representations:



$$\begin{aligned}
U_{10} &\supset SU_2 \times R_5 \supset SU_2 \times R_3 \\
\{1^7\} &\supset [3/2] \times [11] \supset [3/2] \times [1] = {}^4P \\
&\quad [3/2] \times [11] \supset [3/2] \times [3] = {}^4F \\
&\quad [1/2] \times [21] \supset [1/2] \times [1] = {}^2P \\
&\quad [1/2] \times [10] \supset [1/2] \times [2] = {}^2D_1, \\
&\quad [1/2] \times [21] \supset [1/2] \times [2] = {}^2D_2 \\
&\quad [1/2] \times [21] \supset [1/2] \times [3] = {}^2F \\
&\quad [1/2] \times [21] \supset [1/2] \times [4] = {}^2G \\
&\quad [1/2] \times [21] \supset [1/2] \times [5] = {}^2H
\end{aligned} \tag{8}$$

The states and the degeneration numbers associated with the  $3d^7$  electronic configuration of  $\text{Co}^{2+}$  are given in Table 4. The diagram of the matrix is shown in Figure 7.

**Table 4. States and the degeneration numbers for the  $3d^7$  electronic configuration of  $\text{Co}^{2+}$**

State $3d^7$	${}^4P$	${}^4F$	${}^2P$	${}^2D^1, {}^2D^2$	${}^2F$	${}^2G$	${}^2H$
L-degeneration	3	7	3	5	7	9	11
Total degeneration	12	28	6	10×2	14	18	22
Angular momentum J	5/2, 3/2, 1/2	9/2, 7/2, 5/2, 3/2	3/2, 1/2	5/2, 3/2	7/2, 5/2	9/2, 7/2	11/2, 9/2

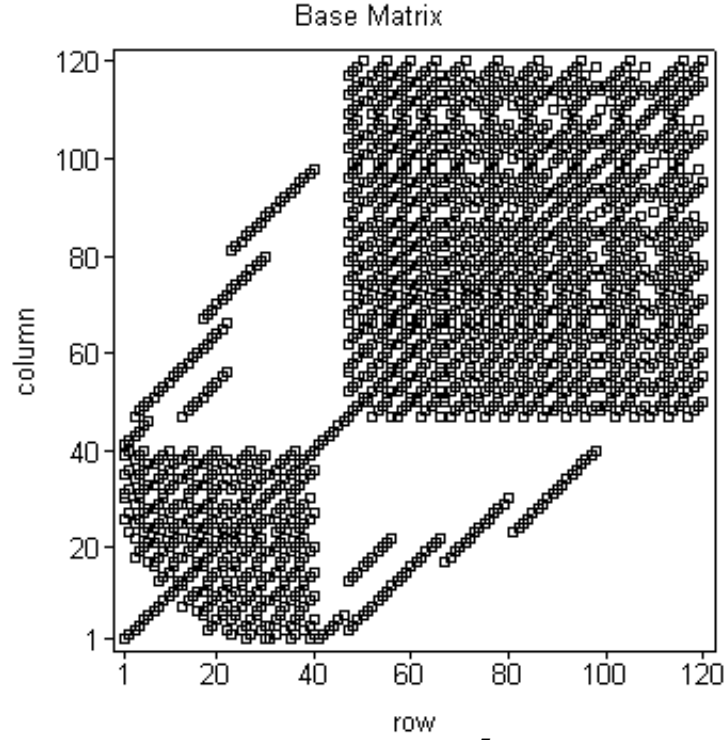


**Figure 7. Diagram of the matrix for the  $3d^7$  electron configuration of  $\text{Co}^{2+}$ .  
The total number of states is 120.**

### 3.3.4 States of $\text{Ni}^{2+}$ ( $3d^8$ electronic configuration).

$\text{Ni}^{2+}$  has a  $3d^8$  configuration and the states are determined by the following representations:

$$\begin{aligned}
 U_{10} &\supset SU_2 \times R_5 \supset SU_2 \times R_3 \\
 \{1^8\} &\supset [1] \times [11] \supset [1] \times [1] = {}^3P \\
 &\supset [1] \times [3] = {}^3F \\
 [0] \times [00] &\supset [0] \times [0] = {}^1S \\
 [0] \times [20] &\supset [0] \times [2] = {}^1D \\
 &\supset [0] \times [4] = {}^1G
 \end{aligned} \tag{9}$$

States and the degeneration numbers for the  $3d^8$  electronic configuration of  $\text{Ni}^{2+}$  are given in Table 5. The diagram of the matrix is shown in Figure 8.

**Table 5. States and the degeneration numbers for the  $3d^8$  electron configuration of  $Ni^{2+}$**

State $3d^8$	$^3P$	$^3F$	$^1S$	$^1D$	$^1G$
L-degeneration	3	7	1	5	9
Total degeneration	9	21	1	5	9
Angular momentum J	2, 1, 0	4, 3, 2	0	2	4

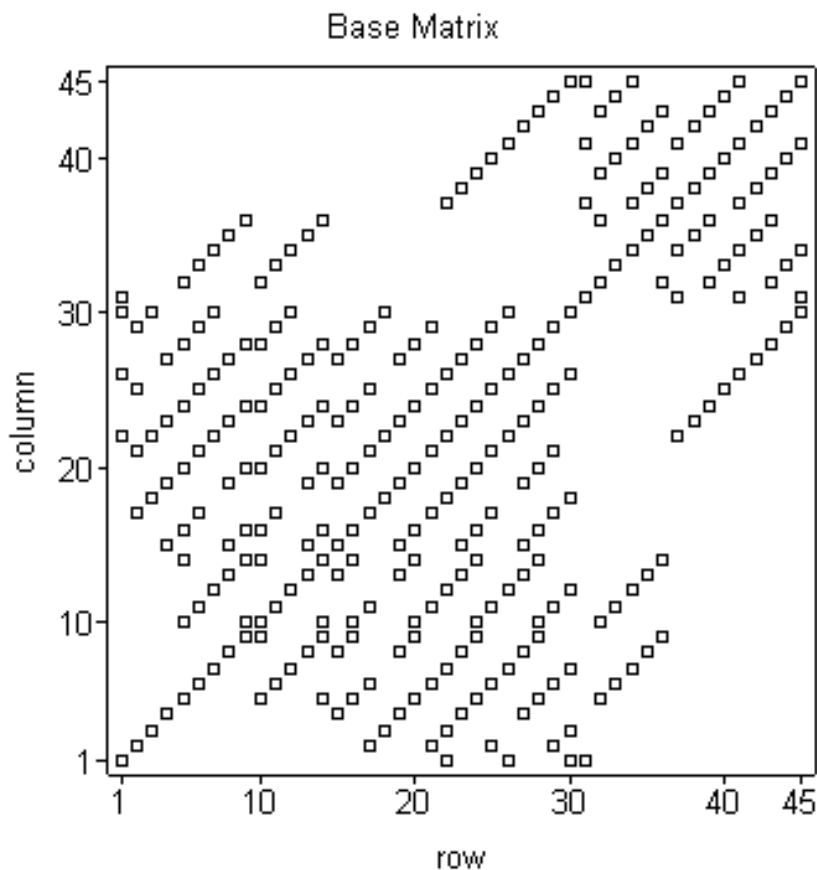


**Figure 8. Diagram of the matrix for the  $3d^8$  electronic configuration of  $Ni^{2+}$ . The total number of states is 45.**

### 3.4 Theory

We will be dealing with the  $3d^n$  electronic configuration of  $M$  atoms in an  $MB_p$ -complex. The goal is to calculate the main interactions of this molecular complex to include the spin-orbit and crystal field interactions of  $M$  with the ligand electrons. The Hamiltonian of these interactions is described by:

$$H = V_{qq} + H_{CF} + H_{SO} \quad (10)$$

where  $V_{qq}$  is the matrix representing the electrostatic interaction between electrons,  $H_{SO}$  is the spin-orbit interaction and  $H_{CF}$  is the crystal field interaction.

The phenomenological method of molecular orbital (MO) (PMMO) theory involves calculation of the energies by using the symmetry of the MO states and the interaction operators. The parameters are then determined by comparing theory with the experiment.

Because of this, matrix elements of the operator defined by equation (10) may be calculated with a formula invoking the full rotation group matrix elements. Therefore, the problem consists of the operation of one or two electron interaction operators on a double  $(l_1, l_2)$  shell electronic configuration.

Matrix elements of the electrostatic and exchange interactions in the form of two electron operators are represented by [9, 10]

$$\begin{aligned} V_{qq}(l_1 l_2 SL) = & f_k(l_1 l_2 L, 2) C_{fk}(l_1 l_2 2) F_2 + f_k(l_1 l_2 L, 4) C_{fk}(l_1 l_2 4) F_4 \\ & + (-1)^S g_k(l_1 l_2 L, 2) C_{gk}(l_1 l_2 2) G_2 + (-1)^S g_k(l_1 l_2 L, 1) C_{gk}(l_1 l_2 1) G_1 \end{aligned} \quad (11)$$

where  $F_2$ ,  $F_4$  and  $G_2$ ,  $G_1$  are the parameters of the electrostatic and exchange interactions, respectively, with the coefficients  $f_k(l_1 l_2 L, k)$ ,  $g_k(l_1 l_2 L, k)$ ,  $C_{fk}(l_1 l_2 k)$ , and  $C_{gk}(l_1 l_2 k)$  being expressed in terms of the  $3j$  and  $6j$  coefficients [11] as:

$$\begin{aligned} f_k(l_1 l_2 L, k) = & (-1)^{l_1 + l_2 + L} \begin{Bmatrix} l_1 & l_2 & L \\ l_2 & l_1 & k \end{Bmatrix}, \quad g_k(l_1 l_2 L, k) = \begin{Bmatrix} l_1 & l_2 & L \\ l_1 & l_2 & k \end{Bmatrix}, \\ C_{fk}(l_1 l_2 k) = & (-1)^{l_1 + l_2 + k} (2l_1 + 1)(2l_2 + 1) \begin{pmatrix} l_1 & k & l_1 \\ 0 & 0 & 0 \end{pmatrix} \begin{pmatrix} l_2 & k & l_2 \\ 0 & 0 & 0 \end{pmatrix} \\ C_{gk}(l_1 l_2 k) = & (2l_1 + 1)(2l_2 + 1) \begin{pmatrix} l_2 & k & l_1 \\ 0 & 0 & 0 \end{pmatrix}^2 \end{aligned} \quad (12)$$

Matrix elements for the exchange interactions with the parameters  $G_1$  and  $G_2$  exist only for the p and d states, respectively. The matrix elements for the exchange operator in eq. (10), last two terms in equation (11), are:

$$\begin{aligned} H_{ex} = & g_2(d) G_2 + g_1(p) G_1, \\ g_2(d) = & (-1)^S g_k(2, 0, 2, 2) C_{gk}(2, 0, 2), \quad g_1(p) = (-1)^S g_k(1, 0, 1, 1) C_{gk}(1, 0, 1) \end{aligned} \quad (13)$$

The matrix elements for the spin-orbit interaction operator of eq. (10) are [9]:

$$\begin{aligned} H_{so}(l_1 l_2 S_1 S_2 L_1 L_2 J) = & \xi_d V_d(l_1 l_2 S_1 S_2 L_1 L_2 J), \\ V_d(l_1 l_2 S_1 S_2 L_1 L_2 J) = & (-1)^{l_1 + l_2 + 1 + L_1 - L_2 - J} \sqrt{2(2l_2 + 1)(2L_1 + 1)(2S_1 + 1)(2L_2 + 1)(2S_2 + 1)} \\ & \begin{Bmatrix} l_2 & l_1 & L_1 \\ L_2 & 1 & l_2 \end{Bmatrix} \begin{Bmatrix} 1/2 & 1/2 & S_1 \\ S_2 & 1 & 1/2 \end{Bmatrix} \begin{Bmatrix} L_1 & S_1 & J \\ S_2 & L_2 & 1 \end{Bmatrix} \end{aligned} \quad (14)$$

The interaction with the CF potential is defined by matrix elements whose values may be calculated from the following formula:

$$V_{gf}(l_1 l_2 S L_1 L_2 J_1 J_2 q_1 q_2) = \sum_{k,q} A_{kq} \begin{bmatrix} J_1 & k & J_2 \\ q_1 & q & q_2 \end{bmatrix} C_{gf}(l_1 l_2 S L_1 L_2 J_1 J_2 k), \quad (15)$$

where

$$C_{gf}(l_1 l_2 S L_1 L_2 J_1 J_2 k) = (-1)^{l_1 + l_2 + S_1 + J_2} \sqrt{(2L_1 + 1)(2J_1 + 1)(2L_2 + 1)(2J_2 + 1)} \\ \left\{ \begin{matrix} l_2 & L_1 & l_1 \\ L_2 & l_2 & k \end{matrix} \right\} \left\{ \begin{matrix} L_1 & J_1 & S \\ J_2 & L_2 & k \end{matrix} \right\},$$

and the square brackets

$$\begin{bmatrix} J_1 & k & J_2 \\ q_1 & q & q_2 \end{bmatrix} = \frac{1}{\sqrt{2J_1 + 1}} \left\{ \begin{matrix} J_1 & k & J_2 \\ q_1 & q & q_2 \end{matrix} \right\}$$

denote the Klebsh-Gordon coefficient. Note that  $V_{gf}$  is equivalent to  $H_{CF}$  in equation 10.

Usually, in the case of semiconductors of the type  $A^{II}B^{VI}$ , the CF symmetry of the active center is described by the  $T_d$  group with distortion from the  $C_{3v}$  group determining the set of CF parameters:  $k, q = 2, 0; 4, 0; 4, 3; 4, -3$ . It is more convenient, though, to use well-known CF parameters corresponding to the pure tetrahedral ( $Dq$  parameter) and trigonal ( $D_E$  parameters) components of the CF potential [9]:

$$\begin{aligned} A_{20} &= A_{2E}, \\ A_{40} &= 21Dq - \frac{\sqrt{15}}{6} D_{4E}, \\ A_{44} &= 3\sqrt{\frac{35}{2}} Dq - \sqrt{\frac{7}{24}} D_{4E}, \quad A_{4-4} = A_{44} \end{aligned} \quad (16)$$

Finally, the interaction operators in (10) are parameterized with the following:  $\xi_d$  as the spin-orbit constant of the d(M) electrons;  $A_{20}$ ,  $A_{40}$ , and  $A_{44}$  as the parameters of interaction with the CF potential of tetrahedral ( $T_d$ ) ( $Dq$ ) symmetry; and  $D_{2E}$ ,  $D_{4E}$  as the low symmetry parameters of the CF potential.

### 3.4.1. Formula for calculation of the matrix elements of the crystal field potential.

$$\langle SL_1 J_1 m_1 | V_{CF} | SL_2 J_2 m_2 \rangle = \sum_{k=2,4} \sum_{q=-k}^{q=k} A_{kq} J_{31}(J_1, k, J_2, m_1, q, m_2) Cr_d(n_1, n_2, S, L_1, L_2, J_1, J_2, k) \quad (17)$$

The calculation of this is described in Appendix 1.  $Cr_d$  is a name for a computer procedure calculating a part of the matrix element of the CF potential.

### 3.4.2. Formula for calculation of the matrix elements of the electrostatic interaction

$$\langle n_1, SL_1 J_1 m_1 | V_{qq} | n_2, SL_2 J_2 m_2 \rangle = qq(n_1, n_2) \quad (18)$$

The calculation of this is described in Appendix 1.

### 3.4.3. Formula for calculation of the matrix elements of the spin-orbit interaction

$$\begin{aligned} \langle n_1, S_1 L_1 J_1 m_1 | V_{SO} | n_2, S_2 L_2 J_2 m_2 \rangle = \\ \delta(J_1 m_1, J_2 m_2) W^{11}(n_1, n_2, L_1, L_2, S_1, S_2) J(n_1, n_2, L_1, L_2, S_1, S_2, J_1) \xi_{3d} \end{aligned} \quad (19)$$

$W^{11}$  is the notation of the reduced double (11) tensor operator in the orbital and spin coordinates of the electron. The calculation of this is described in Appendix 1.

### 3.5. Intensities of transitions between states having the $3d^n$ electronic configuration

Electric dipole (ED) transitions between states of the  $d^n$  configuration are forbidden by parity selection rules. However, in crystals, electro-dipole transitions may exist due to the admixture of the states having opposite parity due to the odd terms of crystal field potential (CFP).

The classification of the odd terms of the CF potential may be done using the following symmetry group reduction series:

$$\begin{aligned} O_3 &\supset O_h \supset T_d \supset C_{3v} \supset C_{4v} \supset C_{2v} \\ [3] &\supset A_{2u} \supset A_1 \\ [1], [3] &\supset F_{1u} \supset F_2 \supset A_1 \\ [3] &\supset F_{1u} \supset F_2 \supset A_1 \\ [3] &\supset F_{2u} \supset F_1 \supset A_1 \end{aligned} \quad (20)$$

The four terms of the series (20) has the following symmetry:  $T_d$ ,  $C_{3v}$ ,  $C_{4v}$  and  $C_{2v}$ , respectively. This is determined by reduction of the odd representations of  $O_3$  on the unity representation of the corresponding groups.

The odd part of CFP may arise from the odd static and dynamic components of the crystal field. The static component which has the representation  $[3]$  of the  $O_3$  group depends on the positions of the surrounding atoms and the second, dynamic component having the representation  $[1]$  of the  $O_3$  group may be due to the vibrations of the atoms.

For case of  $T_d$  symmetry, the resulting even ED operator may be obtained as the product of the odd term  $A_{2u}$  operator of the CFP  $[3]$  and the operator  $[1]$  of the electro dipole transition with the result:  $[3] \times [1] = [4] + [3] + [2]$ . For the  $p$  and  $d$  states, only representations  $[2]$  and  $[4]$  have non-zero matrix elements. The same representation in the  $T_d$  group is determined by the next product:  $[1]F_{1u} \times [3]A_{2u} = [2]F_{2g} + [4]F_{2g}$  and only the  $[2]F_2$  and  $[4]F_2$  operators of  $T_d$  group may be used as representations of the transition operators. Thus, for all of the symmetry groups (20), the transition operator is:

$$\begin{aligned} [2], [4] F_2(0) &\rightarrow \sigma \text{ polarization,} \\ [2], [4] F_2(\pm 1) &\rightarrow \pi \text{ polarization.} \end{aligned} \quad (21)$$

The resulting intensity operator is an even with the matrix coinciding with the crystal field matrix.

For the case of tetrahedral symmetry of the  $T_d$  group, there exists only one independent parameter ( $3A_2$ ), with the other parameters being a linear combination of a spherical function with the parameters  $B_{kq}$ :

$$B_{k\Gamma q} = (1F_{1u}, 3A_{2u} | k\Gamma (F_{1u}\mu_1, A_{2u}e | \Gamma q) 1F_{1u}\mu_1) | 3A_{2u}e \rangle, \quad (22)$$

where the subgroup and Klebsh-Gordon coefficients are presented in [12] and the ratio between the intensities of the spherical parameters is:

$$B_{4q} = -\frac{2}{\sqrt{5}} B_{2q}. \quad (23)$$

Expressions for the  $B_{20}$ ,  $B_{21}$ , and  $B_{2-1}$  polarization parameters in terms of the spherical functions are the following:

$$B_{20} = \sqrt{\frac{5}{16\pi}} \frac{3z^2 - r^2}{r^2}, B_{21} = \sqrt{\frac{15}{8\pi}} \frac{z(x+iy)}{r^2}, B_{2-1} = \sqrt{\frac{15}{8\pi}} \frac{z(-x+iy)}{r^2}. \quad (24)$$

Intensities of the MO transitions may be estimated using a matrix representing the transition operators followed by normalization of this matrix by calculating the interaction between the states of the MO configuration.

The energy level values or eigenvalues are obtained by diagonalization of the matrix  $C_{Rp}$  represented by the operator by:  $E(SL) = M \times C_{Rp} \times M^{-1}$  where  $M$  is the basis function transformation.

The normalized expression for the transition intensities will be:

$$I(SL, SL') = M \times E_{Dp} \times M^{-1}, \quad (25)$$

and the intensities of the electric dipole transitions between the states may be calculated by the following formula:

$$I(l_1 l_2 SL_1 L_2 J_1 J_2 q_1 q_2) = B_{2q} \begin{bmatrix} J_1 & 2 & J_2 \\ q_1 & q & q_2 \end{bmatrix} C_{gf}(l_1 l_2 SL_1 L_2 J_1 J_2 2) + B_{4q} \begin{bmatrix} J_1 & 4 & J_2 \\ q_1 & q & q_2 \end{bmatrix} C_{gf}(l_1 l_2 SL_1 L_2 J_1 J_2 4), \quad (26)$$

where

$$C_{gf}(l_1 l_2 SL_1 L_2 J_1 J_2 k) = (-1)^{l_1 + l_2 + S_1 + J_2} \sqrt{(2L_1 + 1)(2J_1 + 1)(2L_2 + 1)(2J_2 + 1)} \\ \left\{ \begin{matrix} l_2 & L_1 & l_1 \\ L_2 & l_2 & k \end{matrix} \right\} \left\{ \begin{matrix} L_1 & J_1 & S \\ J_2 & L_2 & k \end{matrix} \right\}, k = 2, 4,$$

Intensities of the magnetic dipole transitions, which can be obtained by operating  $L+2S$  on the MO states of equivalent electrons, may be calculated from the following formula:

$$I(l_1 l_2 SL_1 L_2 J_1 J_2 q_1 q_2) = \delta(l_1, l_2) \delta(L_1, L_2) A_{1q} \begin{bmatrix} J_1 & 1 & J_2 \\ q_1 & q & q_2 \end{bmatrix} C_{L+2S}(l_1 l_2 SL_1 L_2 J_1 J_2 1), \quad (27)$$

where

$$G_{L+2S}(l_1 l_2 SL_1 L_2 J_1 J_2 1) = (-1)^{L_1+S+J_2} \sqrt{L_1(L_1+1)(2L_1+1)} \begin{Bmatrix} L_1 & J_1 & S \\ J_2 & L_2 & 1 \end{Bmatrix} +$$

$$+ 2(-1)^{L_1+S+J_1} \sqrt{S(S+1)(2S+1)} \begin{Bmatrix} S & J_1 & L_1 \\ J_2 & S & 1 \end{Bmatrix}.$$

### 3.5.1. Formula for calculation of the transition intensity matrix elements for transitions in iron group ions.

$$\langle SL_1 J_1 m_1 | U_{J_1, J_2} | SL_2 J_2 m_2 \rangle = \sum_{k=2,4} \sum_{q=-k}^{q=k} B_{kq} J_{31}(J_1, k, J_2, m_1, q, m_2) Cr_d(n_1, n_2, S, L_1, L_2, J_1, J_2, k)$$

The transition intensity matrix elements are calculated in the same manner as the matrix elements of the crystal field with the exception of using the intensity parameters  $B_{kq}$ .

### 3.6. Simulation of the absorption spectra of d<sup>n</sup> electronics configurations

Because the  $d^n$  states have many levels which are clumped into a few bands of levels, the absorption spectra of the transitions are characterized by broad bands. This is why it is preferable to represent the spectral distribution of the transition between the ground and excited states as a Gaussian which depends on the wavelength. Thus, theoretical simulation of the absorption spectra may be performed using the following formula for the effective cross section of the absorption transitions:

$$Q(\lambda) = \sum_{\nu=5}^{70} \frac{Q_{\nu}}{\lambda} \exp \left[ - \frac{\left( \frac{10^7}{\lambda} + E_0 - E_{\nu} \right)^2}{S_{\nu}^2} \right], \quad (28)$$

where  $E_0$  and  $E_{\nu}$  are the energies of ground and excited states, respectively,  $S_{\nu}$  is the dispersion width parameter, and  $Q_{\nu}$  is the effective cross-section in  $\text{cm}^{-1}$ .

### 3.7. Oscillator strength and decay time of d<sup>n</sup> electronics configurations

It is reasonable to analyze the absorption spectra of ions of the iron group using parameters which are independent of the form of absorption band. These parameters are the oscillator strength of the absorption transition and the fluorescence lifetime (or decay time).

The oscillator strength  $f$  and decay time  $\tau$  are given by following formulas:

$$f_{JJ'} = \frac{3\epsilon \lambda_{JJ'}^2}{8\pi^2 c r_0 \tau_{JJ'}}, \quad \frac{3}{8\pi^2 c r_0} = 4.52 \text{ cm}^{-2} \text{ s}$$



$$f_{JJ'} = 4.52 \frac{c^2 \varepsilon}{v^2 \tau_{JJ'}} = 1.13 * 10^{-8} \left( \frac{\bar{\lambda}_{JJ'}}{500} \right)^2 \frac{\varepsilon}{\tau_{JJ'}} = 1.13 * 10^{-8} \left( \frac{20000}{E_{JJ'}} \right)^2 \frac{\varepsilon}{\tau_{JJ'}} \quad (29)$$

$$f_{JJ'} = 4.52 \frac{\varepsilon}{E_{JJ'}^2 \tau_{JJ'}} \quad \tau_{JJ'} = 4.52 \frac{\varepsilon}{E_{JJ'}^2 f_{JJ'}}$$

where  $E_{JJ'}$  is the energy gap between the states  $J$  and  $J'$ , the speed of light,  $c$ , and the electron radius,  $r_0$ , are equal to  $3.0 \times 10^{10}$  cm/sec and  $2.82 \times 10^{-13}$  cm, respectively. Also, the decay time, wavelength, and energy of the transitions are represented by  $\tau$ (sec),  $\lambda$  (cm), and  $E$  ( $\text{cm}^{-1}$ ), respectively. The factor representing the local field of the impurity atom arising from the local polarization effect is given by

$$\varepsilon = \frac{9n}{(n^2 + 2)^2}, \quad (30)$$

where  $n$  is the index of refraction.

The transition probability  $A$  is connected with the effective cross section  $Q$  according to the following formula:

$$A_{JJ'} = 8\pi c n^2 \frac{2J+1}{2J'+1} \int E^2 Q_{JJ'}(E) dE, \quad (31)$$

where  $E$  is frequency of the electron transition in  $\text{cm}^{-1}$  and  $Q_{JJ'}$  is the effective cross-section.

The oscillation strength for electro-dipole transitions induced by the crystal field is equal to

$$f_{JJ'} = E_{JJ'} a_2 U_{JJ'}^2 = 4.52 \frac{\varepsilon}{E_{JJ'}^2 \tau_{JJ'}}, \quad (32)$$

where  $a_2$  is an intensity parameter (in cm) which can be determined from eq. (32) and  $U_{JJ'}$  is the matrix element of the tensor operator between the state  $J$  and  $J'$ . For the theoretical calculation of the probability of the absorption transitions, matrix elements of the tensor operator are used:

$$a_2 [U_2^2(jj') + U_4^2(jj')] = a_2 U_{JJ'}^2, \quad (33)$$

where  $U_2(JJ')$  and  $U_4(JJ')$  are the matrix elements of the tensor operator for electric dipole transitions induced by a CF potential having an odd order. The intensity parameter may be calculated using the following formula:

$$a_2 = 4.52 \frac{\varepsilon}{E_{JJ'}^3 \tau_{JJ'} U_{JJ'}^2}. \quad (34)$$

Using a known value for  $a_2$  it is possible to calculate the oscillator strength and decay time:

$$f_{JJ'} = E_{JJ'} a_2 U_{JJ'}^2, \quad \tau_{JJ'} = 4.52 \frac{\varepsilon}{E_{JJ'}^2 f_{JJ'}} \quad (35)$$

### 3.8. Spectroscopic diagrams of $\text{Co}^{2+}$ in tetrahedral crystals of the type $A^{II}B^{VI}$

#### 3.8.1. Diagrams of the energy states of $\text{Co}^{2+}$ ions in tetrahedral semiconductors of the type $A^{II}B^{VI}$ .

To qualitatively describe the effect of the CF, electrostatic and spin-orbital interactions in  $A^{II}B^{VI}$  crystals, we have presented diagrams of the energy states of  $\text{Co}^{2+}$  in terms of units of the interaction parameters.

Figure 9 shows the energy levels of  $\text{Co}^{2+}$  in the relative units  $E/Dq$  and  $E/F_{22}$  versus the relative parameters  $F_{22}/Dq$  and  $Dq/F_{22}$  when  $\xi_{3d} = 0$ , and the Slater parameters  $F_{44} = F_{22}/12.5$ . The left hand side of the diagram corresponds to the case of a strong CF with the electrostatic interaction parameter,  $F_{22}/Dq$ , changing from 0 to 1. At  $F_{22}/Dq = 0$ , all energy levels combine into the four CF configurations:  $t^3$ ,  $t^2e^1$ ,  $t^1e^2$ , and  $e^3$  having the relative energies  $E/Dq = 0, 10, 20$ , and  $30$ .

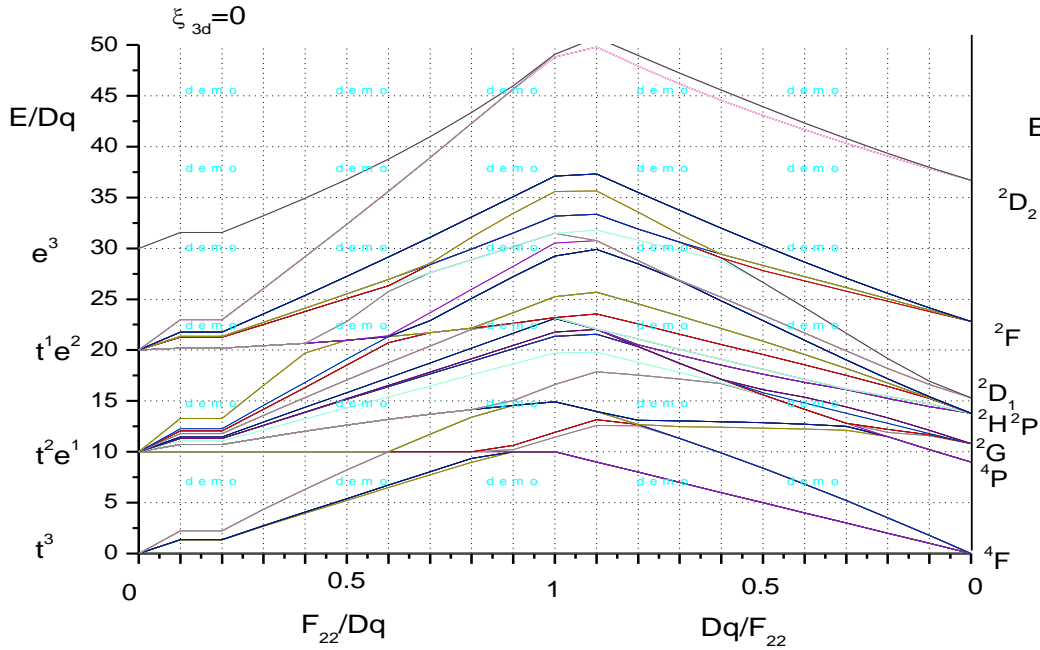


**Figure 9.** Energy level diagram  $\text{Co}^{2+}$ , showing  $E/Dq$  and  $E/F_{22}$  versus the relative parameters  $F_{22}/Dq$  and  $Dq/F_{22}$  when  $\xi_{3d} = 0$ .

The right hand side of the diagram corresponds to the case of a weak CF, where the electrostatic interaction parameter,  $Dq/F_{22}$ , changes from 0 to 1. When  $Dq/F_{22} = 0$ , the energy levels are equivalent to those of a free  $\text{Co}^{2+}$  ion.

In  $\text{A}^{\text{II}}\text{B}^{\text{VI}}$  crystals, the parameter  $Dq/F_{22}$  changes from 0.25 to 0.5. The energy states of  $\text{Co}^{2+}$  ions in terms of the relative parameter  $Dq/F_{22}$  are shown in Figure 10 and 11 over the range relevant for the three crystal types: ZnS, ZnSe, and ZnTe. We will analyze these in the sections which follow starting from the baseline case of  $\text{Co}^{2+}$  in CdS for illustrative purposes.

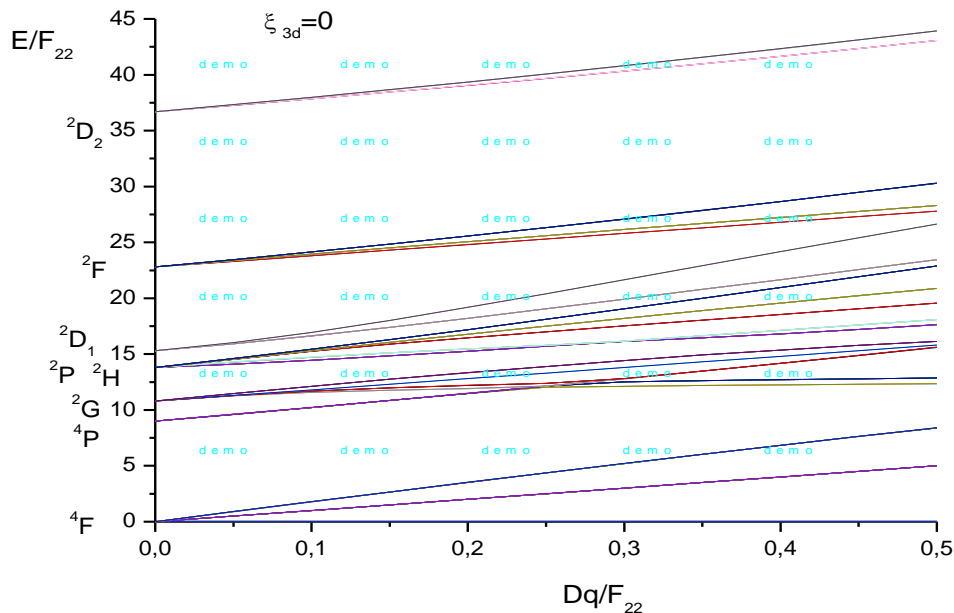


**Figure 10.** The energy levels of  $\text{Co}^{2+}$  in the relative units  $E/F_{22}$  versus the relative parameter  $Dq/F_{22} = 0-0.5$  at  $\xi_{3d} = 0$ .

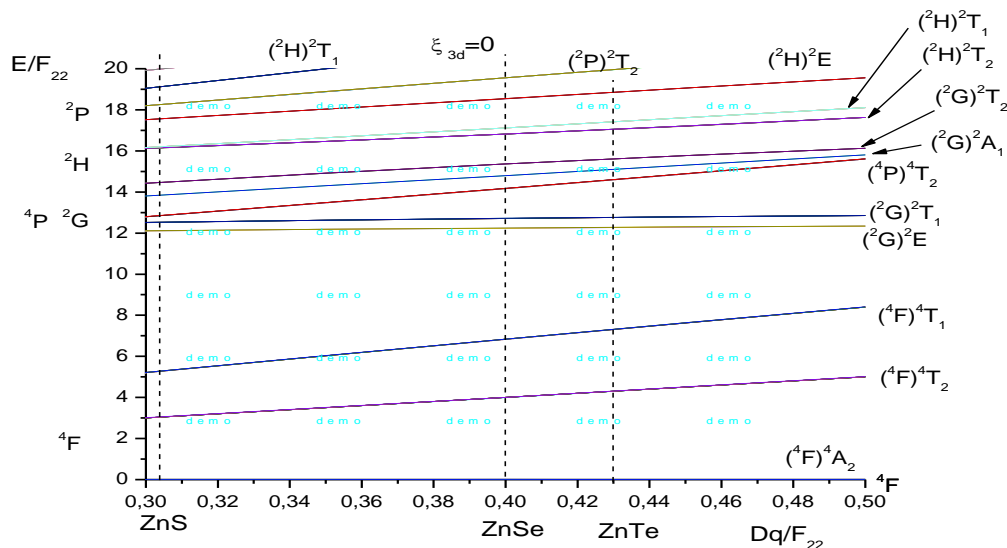


**Figure 11.** The energy levels (with labels) of  $\text{Co}^{2+}$  in the relative units  $E/F_{22}$  versus the relative parameter  $Dq/F_{22} = 0.3-0.5$  at  $\xi_{3d} = 0$ .

### 3.9. Spectra of $\text{Co}^{2+}$ in CdS

In order to obtain a simulation of the spectra of  $\text{Co}^{2+}$ , it is necessary to calculate the intensity parameter,  $a_2$ , for the  ${}^4\text{A}_2 - {}^4\text{F}_2$  luminescence transition having a degeneration factor  $2J+1 = 12$ , a decay time of 1115  $\mu\text{sec}$ , an energy  $E = 3000 \text{ cm}^{-1}$ , and an internal polarization factor of  $\varepsilon = 1/8$ . We derived the following value for the intensity parameter:  $a_2 = 2054682 \text{ cm}^2$ . Using this value of  $a_2$ , it is possible to calculate the cross section for any transition.

#### 3.9.1. Absorption spectra of $\text{Co}^{2+}$ in CdS

The Absorption spectra of both the  $\sigma$ - and  $\pi$ - transitions of  $\text{Co}^{2+}$  in CdS in the  $2000 - 14000 \text{ cm}^{-1}$  and  $2000 - 6000 \text{ cm}^{-1}$  energy region are shown in Figures 12 and 13, respectively. The major transitions are labeled in both diagrams.

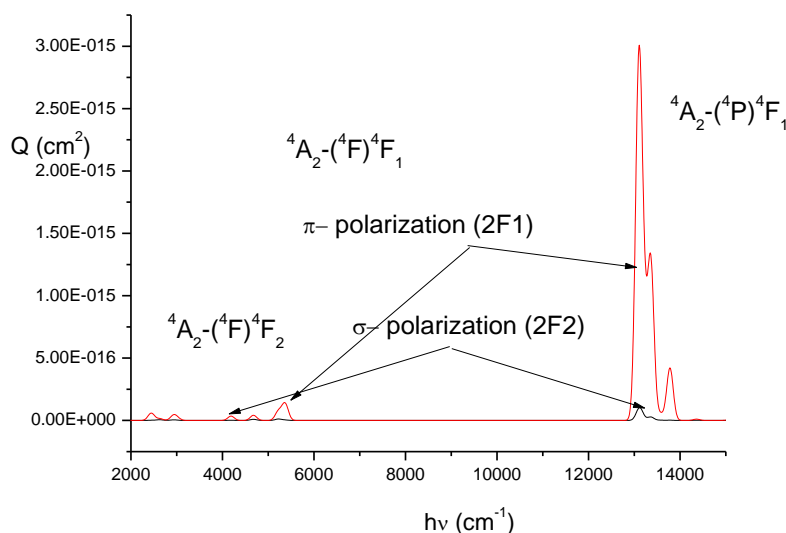


**Figure 12. The Absorption spectra of both the  $\sigma$ - and  $\pi$ - transitions of  $\text{Co}^{2+}$  in CdS in the  $2000 - 14000 \text{ cm}^{-1}$  energy region.**

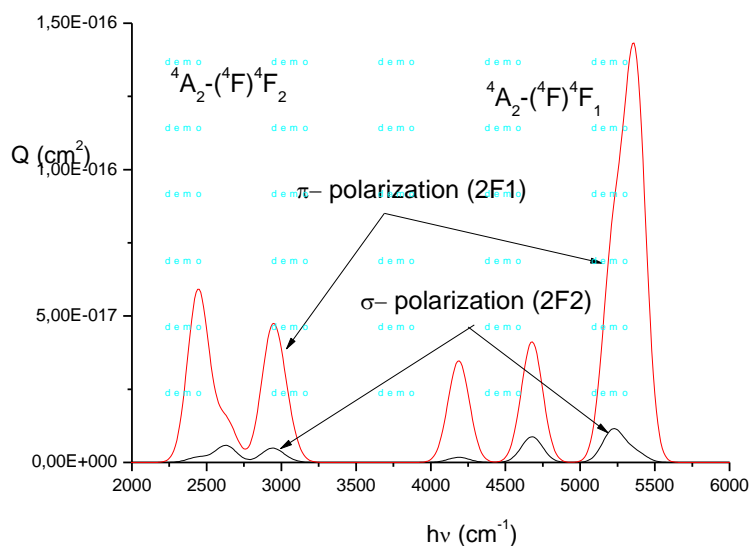


**Figure 13. The absorption spectra of both the  $\sigma$ - and  $\pi$ - transitions of  $\text{Co}^{2+}$  in CdS in the 2000 – 6000  $\text{cm}^{-1}$  energy region.**

### 3.9.2. Luminescence spectra of $\text{Co}^{2+}$ in CdS

The Luminescence spectra upon exciting both  $\pi$ - and  $\sigma$ - transitions of  $\text{Co}^{2+}$  in CdS are presented in Figures 14-19 over various spectral regions. Figures 14 and 15 show luminescence spectra of excitations on  $\pi$ - and  $\sigma$ -  ${}^4\text{A}_2$ - ${}^4\text{F}_1$  transitions of over the 0-6000  $\text{cm}^{-1}$  spectral range. Figures 16 and 17 show luminescence spectra of excitations on  $\pi$ - and  $\sigma$ -  ${}^4\text{A}_2$ -( ${}^4\text{P}$ ) ${}^4\text{F}_1$  transitions of over the 8000-14000  $\text{cm}^{-1}$  spectral range. Figures 18 and 19 show luminescence spectra of excitations on  $\pi$ - and  $\sigma$ -  ${}^4\text{A}_2$ -( ${}^2\text{D}$ ) ${}^2\text{F}_2$  transitions of over the 0-18000  $\text{cm}^{-1}$  spectral range.

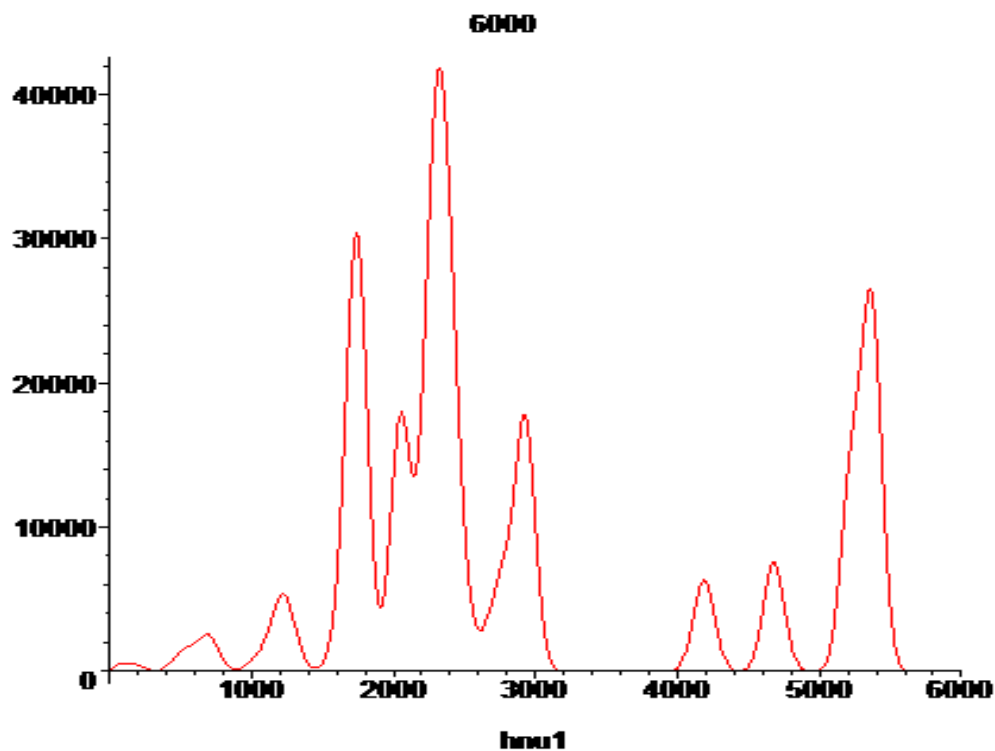


Figure 14. The luminescence spectra of  $\text{Co}^{2+}$  in CdS in the 0-6000  $\text{cm}^{-1}$  region upon excitation of the  $\pi$ - transition  ${}^4\text{A}_2$ - ${}^4\text{F}_1$ .

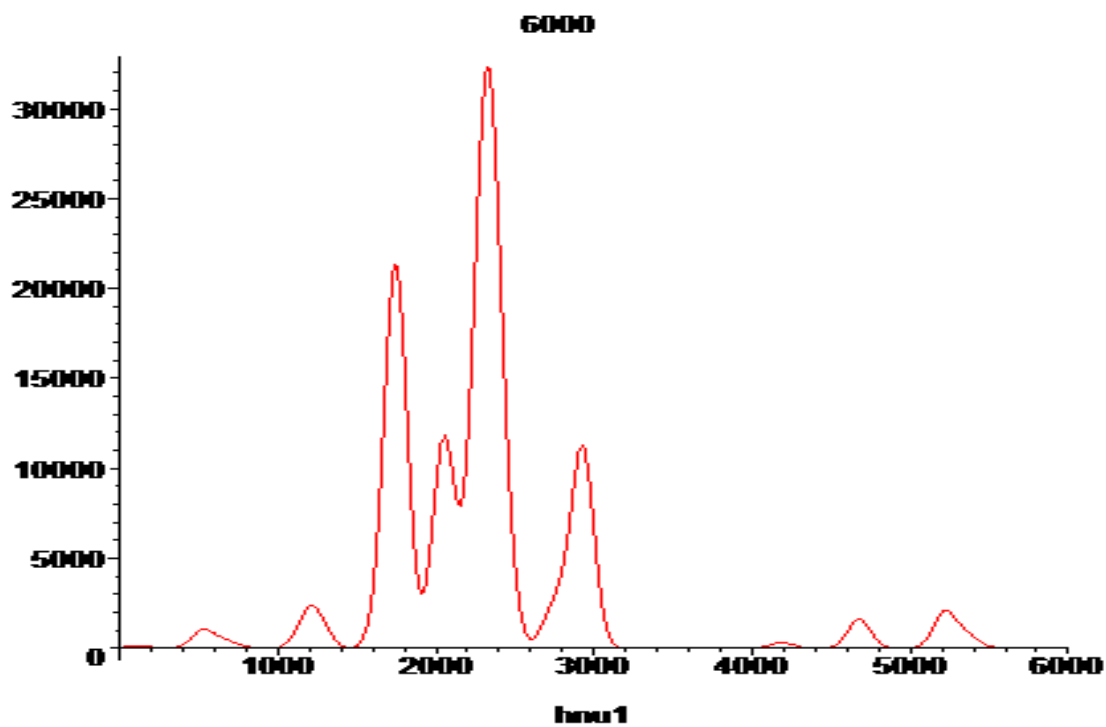


Figure 15. The luminescence spectra in the 0-6000  $\text{cm}^{-1}$  region of  $\text{Co}^{2+}$  in CdS upon excitation of the  $\sigma$ - transition  ${}^4\text{A}_2$ -( ${}^4\text{F}$ ) ${}^4\text{F}_1$ .

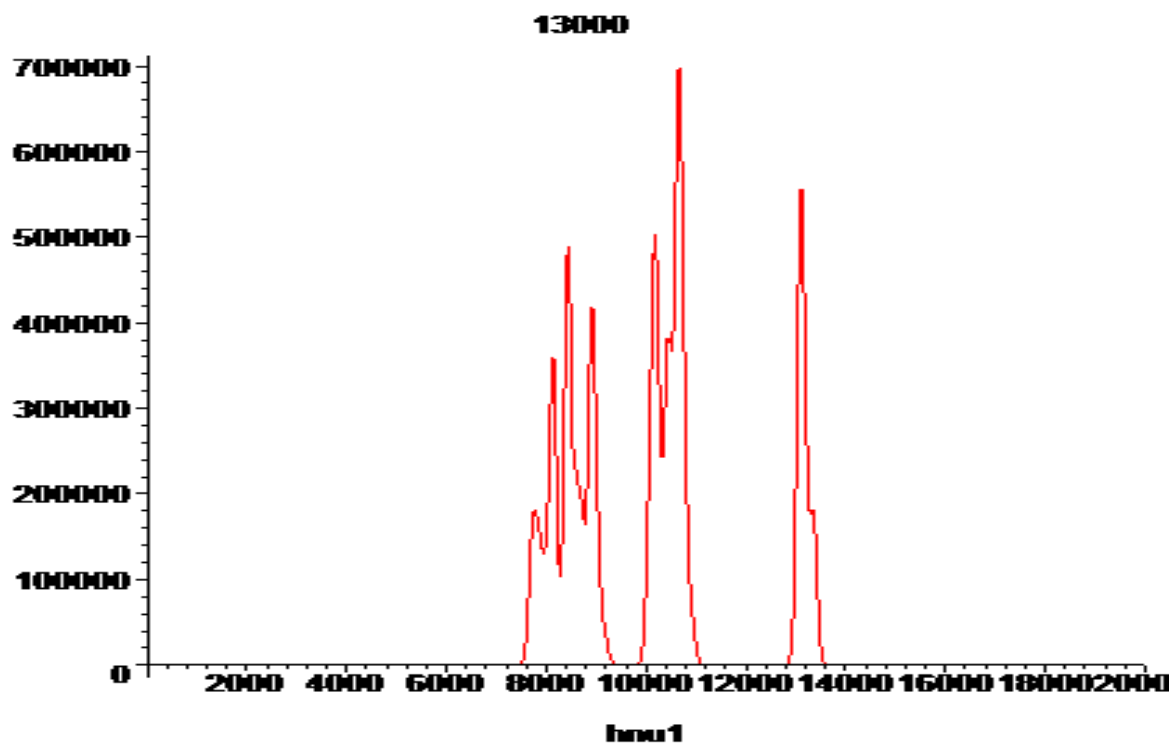


Figure 16. Luminescence spectra in the 8000-14000  $\text{cm}^{-1}$  region of  $\text{Co}^{2+}$  in CdS upon excitation of the  $\pi$ -transition  ${}^4\text{A}_2-({}^4\text{P}){}^4\text{F}_1$ .

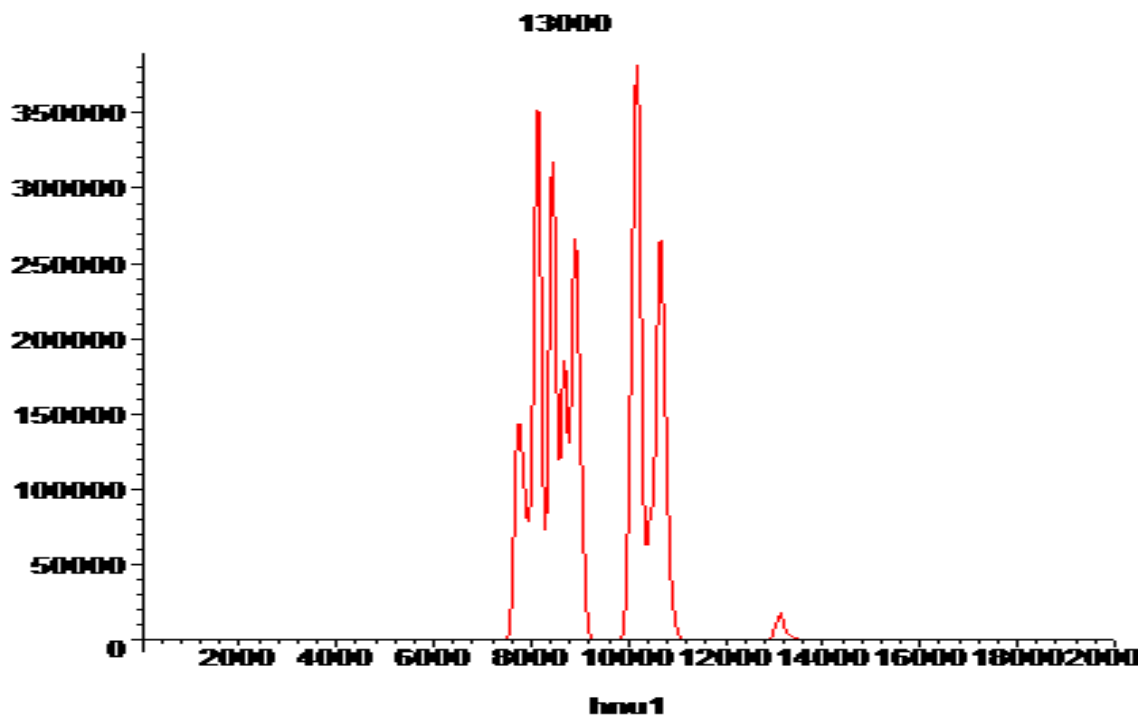


Figure 17. Luminescence spectra in the 8000-14000  $\text{cm}^{-1}$  region of  $\text{Co}^{2+}$  in CdS upon excitation of the  $\sigma$ -transition  ${}^4\text{A}_2-({}^4\text{P}){}^4\text{F}_1$ .

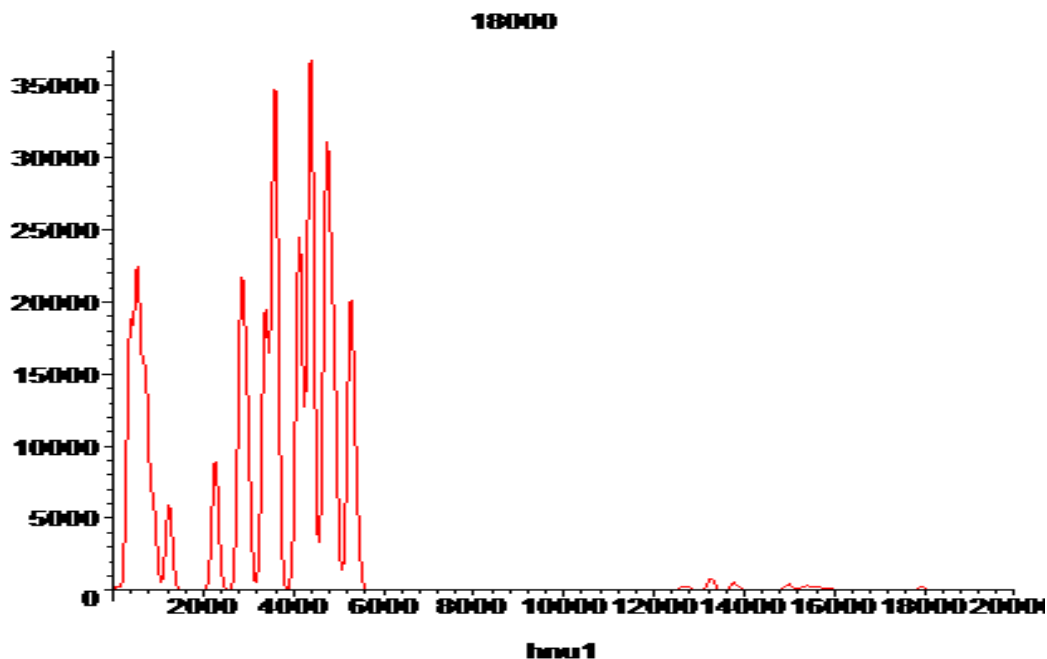


Figure 18. Luminescence spectra in the 0-18000  $\text{cm}^{-1}$  region of  $\text{Co}^{2+}$  in CdS upon excitation of the  $\pi$ - transition  ${}^4\text{A}_2-({}^2\text{D})^2\text{F}_2$ .

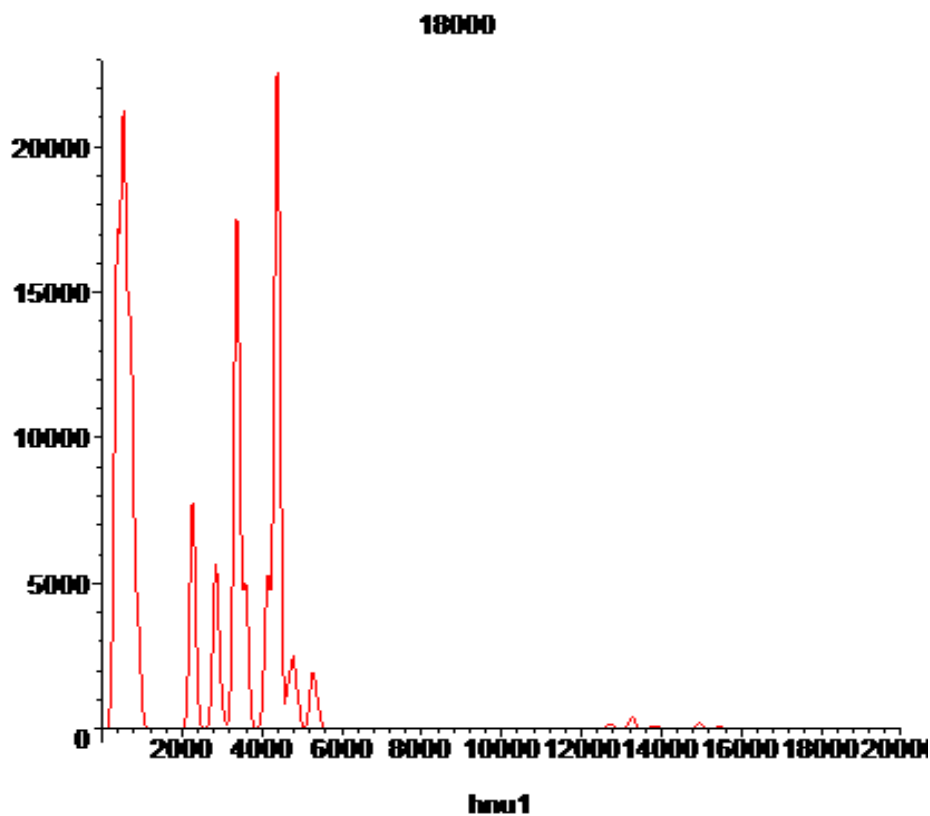


Figure 19. Luminescence spectra in the 0-18000  $\text{cm}^{-1}$  region of  $\text{Co}^{2+}$  in CdS upon excitation of the  $\sigma$ - transition  ${}^4\text{A}_2-({}^2\text{D})^2\text{F}_2$ .



### 3.10. Absorption spectra from excited states of the $(^4F)^4F_2$ multiplet

The absorption spectra of  $\text{Co}^{2+}$  in CdS for both the  $\sigma$ - and  $\pi$ - transitions from the excited states of the  $(^4F)^4F_2$  multiplet are presented in Fig. 20.

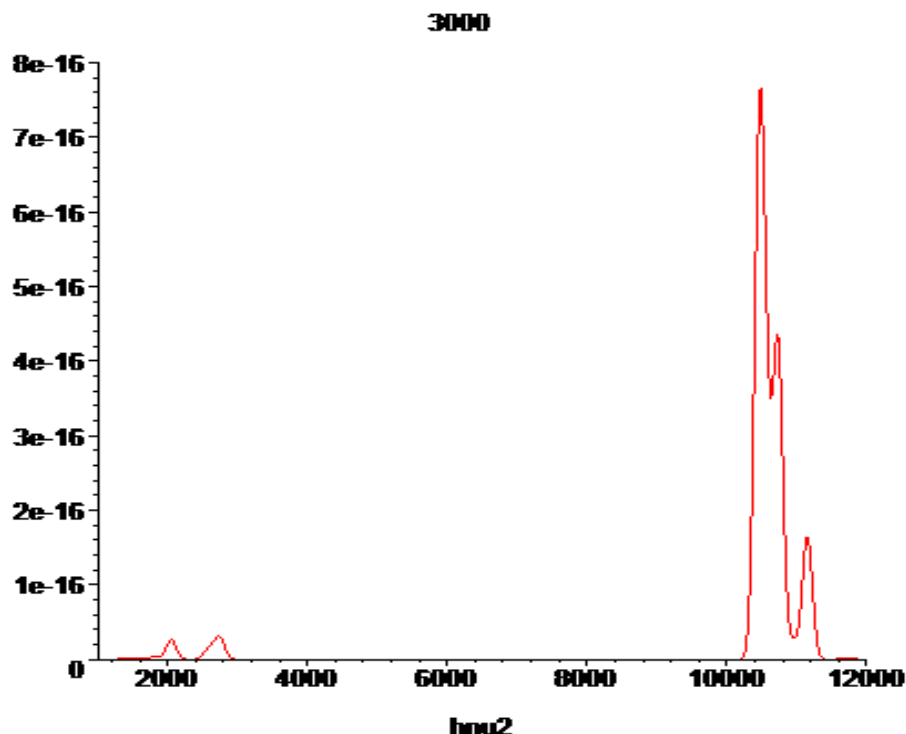


Figure 20. Absorption spectra of  $\text{Co}^{2+}$  in CdS for both the  $\sigma$ - and  $\pi$ - transitions from the excited states of the  $(^4F)^4F_2$  multiplet.

### 3.11 Selection rule for the transitions $(^4F)^4A_2-(^4F)^4F_2$ and $(^4F)^4A_2-(^4F)^4F_1$

The representation of the electric dipole operator in crystals with  $T_d$  CF symmetry is  $F_2$ . Transitions from the  $A_2$  initial state are only possible to the states having the representation  $A_2 \times F_2 = F_1$ . This is why the transition  $^4A_2-(^4F)^4F_1$  is allowed and the transition  $^4A_2-(^4F)^4F_2$  is forbidden. Yet, this rule holds only for the case of a strong CF. For the kind of CF commonly found in semiconductors, this rule is violated because of the spin – orbit interaction. A very interesting task is to investigate the dependence of the ratio of cross sections for the two transitions  $G = Q(^4A_2-(^4F)^4F_2)/Q(^4A_2-(^4F)^4F_1)$  on the ratio of the two main intensity parameters  $B_4/B_2$ . With an increase in the fourth order intensity parameter relative to the second order intensity parameter,  $B_{41}/B_{21}$ , from 0 to 0.8, the ratio  $G$  increases from 0.535 to 1.426 (see Table 6).

**Table 6. Dependence of the ratio of the cross section for the two transitions  $G=Q(^4A_2-^4F)^4F_2)/Q(^4A_2-^4F)^4F_1)$  on the ratio of the two main intensity parameters  $B_4/B_2$ .**

$B_{22}=B_{21}$	$B_{42}=B_{41}$	$B_{41}/B_{21}$	$G$
1	0.795	0.795	1.426
1	0.696	0.696	1.29
1	0.596	0.596	1.14
1	0.496	0.496	0.998
1	0.396	0.396	0.86
1	0.298	0.298	0.727
1	0.198	0.198	0.625
1	0	0	0.535

### 3.12 Configuration coordinate model of transition dynamics

To understand the dynamics of the electronic transitions and the influence of fluctuations of the atoms in the crystal lattice on these dynamics, a system of configuration coordinates is used to define the ion energy. The origin of the configuration coordinate,  $R$ , is defined to be where the minimum in the potential energy curve for the ground state of the active ion occurs. For excited states, there is a shift,  $R_0$ , associated with the minimum in the potential energy curve relative to the ground state.

$$U_g(r) = \frac{1}{2}k_g(r/R)^2 \quad (36)$$

$$U_e(r) = \frac{1}{2}k_e\left(\frac{r}{R} - \frac{R_0}{R}\right)^2 + U_0. \quad (37)$$

The potential functions for the ground ( $U_g(r)$ ) and excited state ( $U_e(r)$ ) in equations (36) and (37) have spherical symmetry and form one dimensional configuration curves for the ground and excited states of the active ions in semiconductors. These curves determine the dynamics of the transition.

In addition, crystal fluctuations will modulate the potential of a crystal field as well as the  $Dq$  parameter whose value can be represented as

$$Dq(R, r) = \frac{Dq(R)}{\left(1 - k\frac{r}{R}\right)^5} \quad (38)$$

where  $k$  is the coefficient of electron phonon coupling.

### 3.13 Spectra of $Co^{2+}$ in ZnSe

#### 3.13.1 Absorption spectra of $Co^{2+}$ in ZnSe

We calculated the absorption spectra of  $Co^{2+}$  ions using the following parameters:

Electrostatic and spin-orbital interactions:  $F_{22} = 965 \text{ cm}^{-1}$ ,  $F_{44} = 76 \text{ cm}^{-1}$ ,  $B = F_{22} - 5F_{44} = 585 \text{ cm}^{-1}$ ,  $C = 35F_{44} = 2660 \text{ cm}^{-1}$ ,  $\xi_{3d} = -535 \text{ cm}^{-1}$ ;

Crystal field parameters:  $Dq = 361 \text{ cm}^{-1}$ ,  $A_{40} = 3\sqrt{70}Dq = 9061 \text{ cm}^{-1}$ ,  $A_{44} = 15Dq = 5415 \text{ cm}^{-1}$ ;  $A_{20} = A_{21} = A_{2-1} = A_{22} = A_{2-2} = 0$ ,  $A_{41} = A_{4-1} = A_{42} = A_{4-2} = A_{43} = A_{4-3} = 0$ .

Intensity parameters for  $\sigma$  polarization:  $B_{20} = 0$ ,  $B_{22} = 1$ ,  $B_{40} = 0$ ,  $B_{41} = 0$ ,  $B_{42} = -2/\sqrt{5} B_{22} * 0.1$ ,  $B_{43} = 0$ ,  $B_{44} = 0$ .

Intensity parameters for  $\pi$  polarization:  $B_{20} = 0$ ,  $B_{21} = 1$ ,  $B_{22} = 0$ ,  $B_{41} = 1/\sqrt{10} B_{21} * 0.1$ ,  $B_{42} = 0$ ;  $B_{43} = -\sqrt{7}/\sqrt{10} * 0.1 B_{21}$ ,  $B_{44} = 0$ .

Parameter  $\varepsilon$  of the local polarization at  $n = 2.44$ :  $\varepsilon = 0.347$ .

Shown in Table 7 are the energy levels and oscillator strengths of the absorption spectra transitions of  $\text{Co}^{2+}$  in ZnSe (with polarizations  $\pi$ ,  $\sigma$ , and total polarization).

**Table 7. Energy levels and oscillator strengths of the absorption spectra transitions of  $\text{Co}^{2+}$  in ZnSe (with polarizations  $\pi$ ,  $\sigma$ , and total polarization).**

$N_2$	$J'$	$\Gamma'$	$E$	$f_g(\pi) * 10^7$	$f_g(\sigma) * 10^7$	$f_g(\sigma) + 2 f_g(\pi) * 10^7$
5	$(^4F)^4T_2$	$\Gamma_6$	3518	15	0,7	31
7		$\Gamma_8$	3593	161	1,4	323
11		$\Gamma_8$	3670	343	1,5	688
15		$\Gamma_7$	3732	40	1,8	82
17	$(^4F)^4T_1$	$\Gamma_6$	6030	1214	56,8	2486
19		$\Gamma_8$	6088	3436	26,1	6898
23		$\Gamma_8$	6418	630	44,9	1304
27		$\Gamma_6$	6609	277	8,8	562
29	$(^2G)^2E$	$\Gamma_8$	11655	24	3,4	52
33	$(^2G)^2T_1$	$\Gamma_8$	12192	542	27,1	1111
37		$\Gamma_6$	12243	309	27,8	645
39	$(^4P)^4T_1$	$\Gamma_6$	13208	20497	31,2	41025
41		$\Gamma_8$	13306	33632	174,6	67438
45		$\Gamma_8$	13598	22393	73,8	44860
49		$\Gamma_6$	13601	11912	182,6	24007
51	$(^2G)^2A_1$	$\Gamma_6$	14074	122	1,3	245
53	$(^2G)^2T_2$	$\Gamma_6$	14432	68	1,0	137
55		$\Gamma_8$	14596	47	0,3	94
59	$(^2H)^2T_2$	$\Gamma_8$	15967	14	0,2	28
63		$\Gamma_6$	16009	135	0,1	270

65	$(^2\text{H})^2\text{T}_1$	$\Gamma_6$	16172	19	0,0	38
67		$\Gamma_8$	16458	467	1,7	936
71	$(^2\text{H})^2\text{E}$	$\Gamma_8$	17660	63	0,0	125
75	$(^2\text{P})^2\text{T}_2$	$\Gamma_6$	18443	62	14,2	139
77		$\Gamma_8$	18631	223	10,7	457
81	$(^2\text{H})^2\text{T}_1$	$\Gamma_6$	19712	1	1,7	4
83		$\Gamma_8$	19797	19	1,0	39
87	$(^2\text{D})^2\text{T}_2$	$\Gamma_8$	20359	10	0,2	20
91		$\Gamma_6$	20585	6	0,3	12
93	$(^2\text{D})^2\text{E}$	$\Gamma_8$	22719	10	0,0	19
97	$(^2\text{F})^2\text{A}_2$	$\Gamma_6$	25683	0	0,0	0
99	$(^2\text{F})^2\text{T}_2$	$\Gamma_6$	25963	2	2,5	7
101		$\Gamma_8$	26129	3	1,5	7
105	$(^2\text{F})^2\text{T}_1$	$\Gamma_6$	27262	6	30,6	42
107		$\Gamma_8$	27369	36	34,3	107
111	$(^2\text{D})^2\text{E}$	$\Gamma_8$	39836	6	0,0	12
115	$(^2\text{D})^2\text{T}_2$	$\Gamma_8$	40477	111	0,4	222
119		$\Gamma_6$	40517	90	0,0	180

Shown in Figure 21-23 are the absorption spectra in the 3000-42000  $\text{cm}^{-1}$  region of  $\text{Co}^{2+}$  in ZnSe. The major absorptions are labeled in each figure

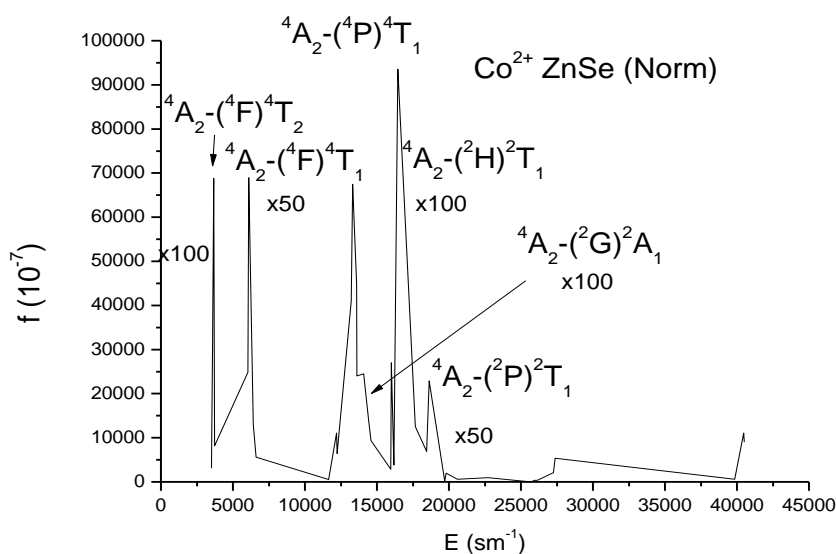


**Figure 21. Absorption spectra in the 3000-42000  $\text{cm}^{-1}$  range of  $\text{Co}^{2+}$  in ZnSe.**

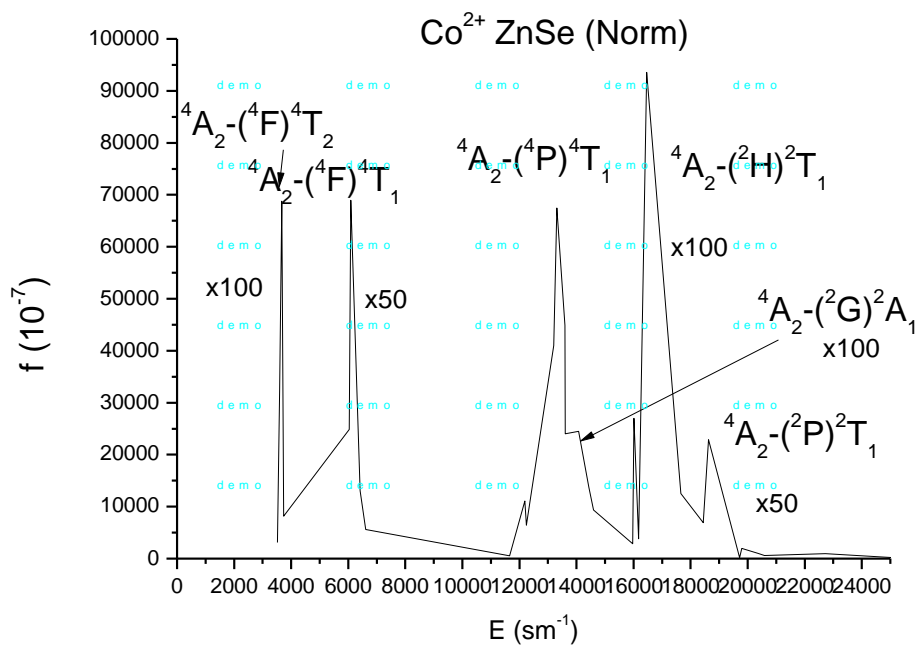


Figure 22. Absorption spectra in the 3000-24000  $\text{cm}^{-1}$  range of  $\text{Co}^{2+}$  in  $\text{ZnSe}$ .

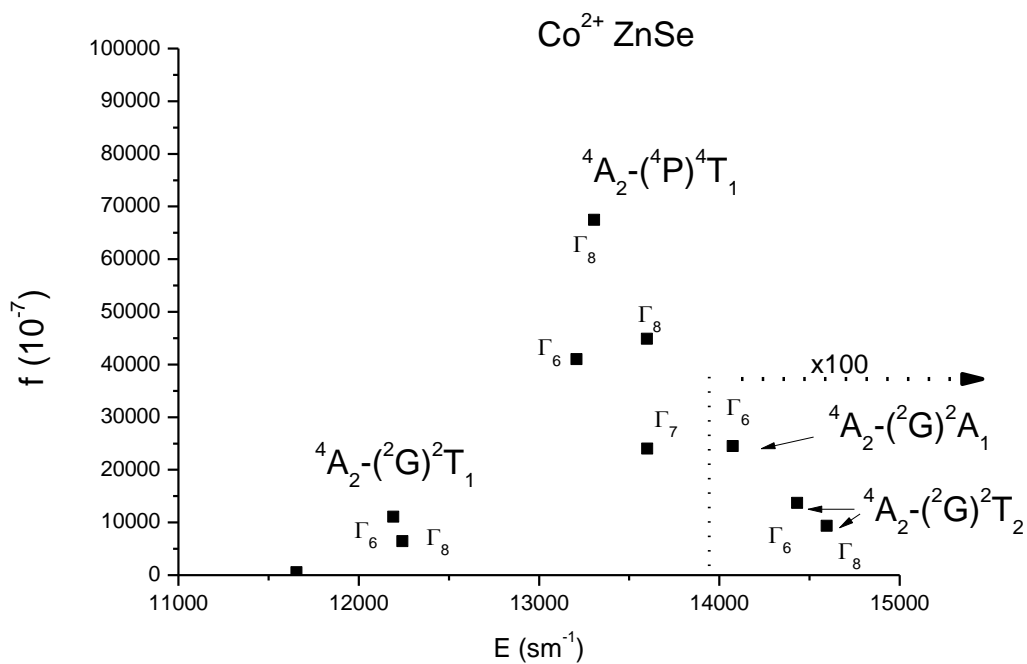
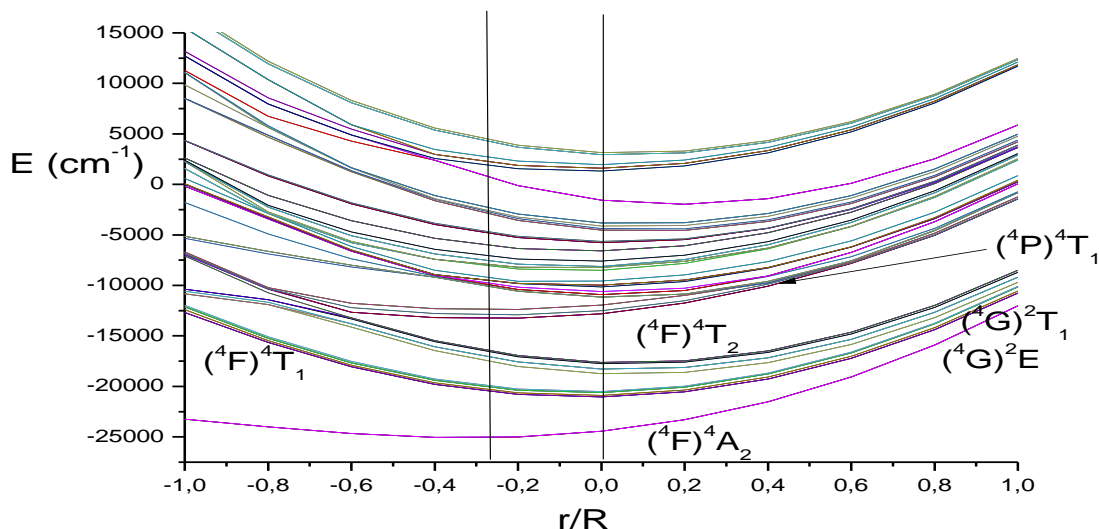


Figure 23. Absorption spectra in the 11000-15000  $\text{cm}^{-1}$  range of  $\text{Co}^{2+}$  in  $\text{ZnSe}$ .

### 3.14 Configuration coordinate model of the transition dynamics of $\text{Co}^{2+}$ in ZnSe

Shown in Figure 24 are the energy levels of  $\text{Co}^{2+}$  in ZnSe versus the relative configuration coordinate  $r/R$ . The major states are labeled in the diagram.



**Figure 24. Energy level diagram of  $\text{Co}^{2+}$  in ZnSe versus the relative configuration coordinate  $r/R$ .**

Parameters associated with the minima in the configuration curves (CC) for the ground and excited states as well as the absorption energies from the  $(^4\text{F})^4\text{T}_2$  ground state with  $k = 0.2$  are given in Table 8. These parameters were calculated using the formulas given in equations (36-38).

**Table 8. Parameters associated with the minimum in the configuration curves (CC) as well as the absorption energies from the  $(^4\text{F})^4\text{T}_2$  ground state with  $k = 0.2$ .**

Parameter of CC minimum			Absorption energies		
States	$r/R$	$E(\text{cm}^{-1})$	$(^4\text{F})^4\text{T}_2$	$(^2\text{G})^2\text{T}_1; ^2\text{E}$	$(^4\text{P})^4\text{T}_1$
$(^4\text{F})^4\text{A}_2$	-0.341	-25061	-20145	-16355	-12989
$(^4\text{F})^4\text{T}_2$	-0.03	-21034			
$(^2\text{G})^2\text{T}_1; ^2\text{E}$	0.11	-17875			
$(^4\text{P})^4\text{T}_1$	-0.338	-13367			

The dependence of configuration curve energies vs  $r/R$  for the ground level  $^4\text{A}_2(\Gamma_8)$  and the excited level  $^4\text{T}_2(\Gamma_8)$  are given by the following equations:

$$^4\text{A}_2(\Gamma_8): E_a = 1462x^3 + 6821x^2 + 4143x - 24383; \quad (39)$$

$$x_{\min} = -0.341; E_{a,\min} = -25061; E_a(x = -0.03) = -24501.$$

$$^4\text{T}_2(\Gamma_8): E_e = 394x^3 + 9336x^2 + 557.7x - 21026; \quad (40)$$

$$x_{\min} = -0.03; E_{e,\min} = -21034; E_e(x = -0.341) = -20145.$$

A diagram of the energy levels of the  ${}^4A_2(\Gamma_8)$  state (the lower curve) and the  ${}^4T_2(\Gamma_8)$  state (the upper curve) of  $\text{Co}^{2+}$  in ZnSe versus the relative configuration coordinate  $x = r/R$  are shown in Figure 25.

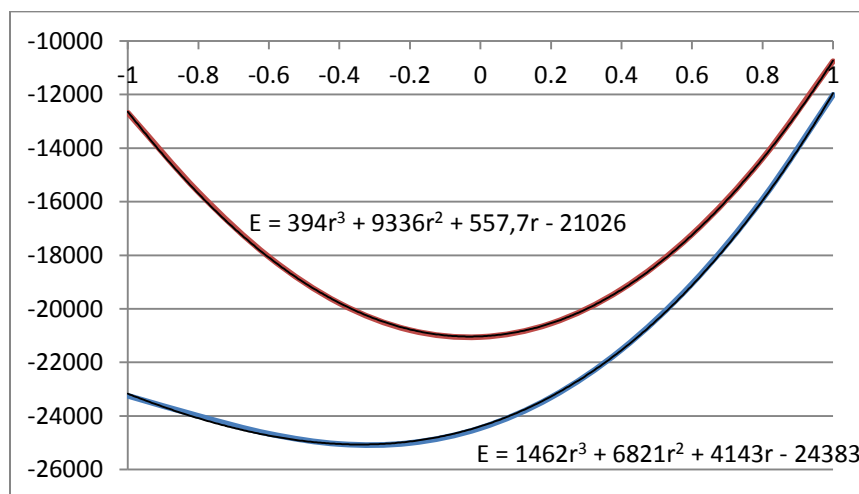


**Figure 25. Diagram of the energy levels of the  ${}^4A_2(\Gamma_8)$  state (the lower curve) and the  ${}^4T_2(\Gamma_8)$  state (the upper curve) of  $\text{Co}^{2+}$  in ZnSe versus the relative configuration coordinate  $x=r/R$ .**

Shown in Figure 26 is a diagram of the energy levels  ${}^4A_2(\Gamma_8)$  (the lower curve) and  ${}^4T_2(\Gamma_8)$  (the upper curve) of  $\text{Co}^{2+}$  in ZnSe with the energies and configuration coordinate values for the absorption and emission transitions.

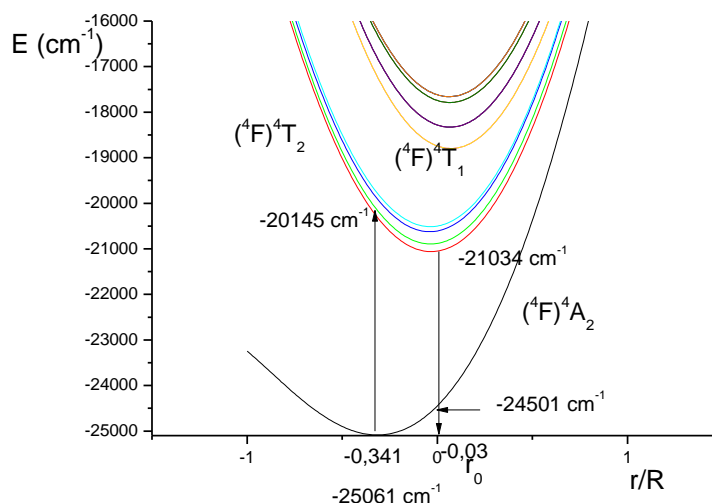


**Figure 26. Diagram of the energy levels  ${}^4A_2(\Gamma_8)$  (the lower curve) and  ${}^4T_2(\Gamma_8)$  (the upper curve) of  $\text{Co}^{2+}$  in ZnSe with the energies and configuration coordinate values for the absorption and emission transitions.**

Generally, the configuration curve may be represented as a polynomial line as shown in Fig 27 for ground and upper states.

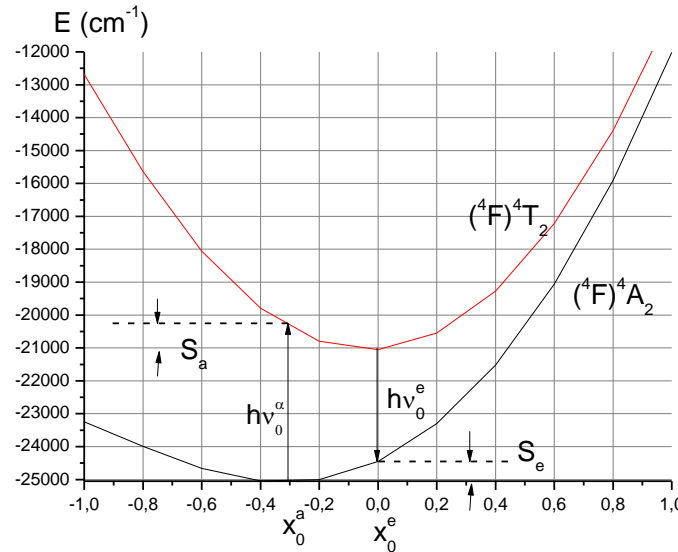


**Figure 27. Diagram of the energy levels  ${}^4A_2(\Gamma_8)$  (the lower curve) and  ${}^4T_2(\Gamma_8)$  (the upper curve) of  $\text{Co}^{2+}$  in ZnSe along with the photon and phonon parameters of the absorption and emission transitions.**

The energies of the ground and excited states in the parabolic case may be represented by following formula:

$$E_a(x) = k_a(x - x_0^a)^2 \text{ and } E_e(x) = k_e(x - x_0^e)^2, \quad (41)$$

where  $k_a$  and  $k_e$  are the coefficients of the harmonic vibrations (CHV) associated with the absorption and emission transitions in  $\text{cm}^{-1}$ .

The eigenfunctions of the absorption and emission states are given by the following eigenfunctions for harmonic oscillations

$$\psi_m^a(x) = N_m \exp\left[-\frac{\left[\frac{x - x_0^a}{4A_a}\right]^2}{2}\right] H_m(x/A_a) \quad (42)$$

where  $H_m$  and  $N_m$  are Hermite functions and  $N$  is the normalization factor. The vibration amplitude  $A_a$  at the point of the energy minimum for the ground state is equal to:

$$A_a^2 = \frac{\hbar}{R\sqrt{Mk_a}} = \frac{\hbar}{R^2M\omega_a}, \quad (43)$$

the vibration amplitude  $A_e$  at the point of the energy minimum for the excited state is equal to:

$$A_e^2 = \frac{\hbar}{R\sqrt{Mk_e}} = \frac{\hbar}{R^2M\omega_e}, \quad (44)$$

where  $R$  is the  $M$  – ligand distance.

The phonon frequencies for the absorption and emission transitions are equal to



$$\nu_a = \frac{1}{2\pi R} \sqrt{\frac{k_a}{M}}, \quad \nu_e = \frac{1}{2\pi R} \sqrt{\frac{k_e}{M}}. \quad (45)$$

The energies of an optical phonon are defined as  $0.031\text{eV} = 250\text{cm}^{-1}$  for longitudinal phonons and  $0.0263\text{eV} = 212\text{cm}^{-1}$  for transverse phonons in [13].

The Gaussian form of the absorption band around the central frequency  $\nu_0^a$  is described by

$$I(\nu) = \frac{1}{\sqrt{2\pi}\sigma_a} \exp[-(\nu-\nu_0^a)/2\sigma_a^2], \quad (46)$$

where the bandwidths are

$$\sigma_a^2 = \frac{(x_0^a R)^2}{2\pi h} \frac{k_e^2}{R^3 \sqrt{k_a M}} = \frac{(x_0^a)^2}{2\pi h} \frac{k_e^2}{R \sqrt{k_a M}}, \quad \sigma_e^2 = \frac{(x_0^e R)^2}{2\pi h} \frac{k_a^2}{R^3 \sqrt{k_e M}} = \frac{(x_0^e)^2}{2\pi h} \frac{k_a^2}{R \sqrt{k_e M}}, \quad (47)$$

and  $M = 4(M_{Se} + \alpha^2 M_{Zn})$ ,  $\alpha$  is the coefficient of a chemical bond Zn-Se (0.2-0.4), and  $k_a$  and  $k_e$  are the parabolic coefficients of the vibration–electron coupling of the absorption and emission bands, respectively.

The energies  $S_a$  and  $S_e$  are defined as:

$$S_a = N_a h \nu_e, \quad S_e = N_e h \nu_a, \quad (48)$$

where  $N_a$  is the average number of quanta (of heat energy or phonons) with energy  $h\nu_e$  emitted after photon absorption; and  $N_e$  is the average number of phonons with energy  $h\nu_a$  which are absorbed after photon emission.

The bandwidths of the emission and absorption transitions are equal to

$$\sigma_e^2 = N_e \frac{\nu_a^3}{\nu_e}, \quad \sigma_a^2 = N_a \frac{\nu_e^3}{\nu_a}. \quad (49)$$

According to equations (39) and (40) for  $\text{Co}^{2+}$ , the CHV coefficients of the emission and absorption transitions are equal to:  $k_a = 6824 \text{ cm}^{-1}$  and  $k_e = 9336 \text{ cm}^{-1}$ . The coordinates of the energy minimums of the absorption and emission transitions are  $x_0^a = -0.341$ , and  $x_0^e = -0.03$ . Therefore, starting with our parameters, the energy of the phonons for the absorption and emission transitions is calculated to be  $\nu_a = 43 \text{ cm}^{-1}$  and  $\nu_e = 51 \text{ cm}^{-1}$ .

### 3.15 Spectral properties of $\text{Ni}^{2+}$ in ZnSe

#### 3.15.1 $\text{Ni}^{2+}$ energy state diagrams in tetrahedral semiconductors of the type $A^{II}B^{VI}$ .

To qualitatively find the parameter range of the crystal field as well as the electrostatic and spin-orbital interactions in  $A^{II}B^{VI}$  crystals, we calculated energy state diagrams of  $\text{Ni}^{2+}$  in terms of the relative units of the interaction. An energy level diagram for  $\text{Ni}^{2+}$  in ZnSe is shown in Figure 28.

The energy level diagram of  $\text{Ni}^{2+}$  in ZnSe in terms of the relative units  $E/Dq$  and  $E/F_{22}$  versus the relative units of the  $F_{22}/Dq$  and  $Dq/F_{22}$  parameters with zero spin-orbital interaction  $\xi_{3d} = 0$ , and  $F_{44} = F_{22}/12.5$  is shown in Figure 29. The left side of the diagram corresponds to a strong crystal field where electrostatic interaction parameters  $F_{22}/Dq$  changes from 0 to 1. When  $F_{22}/Dq = 0$  all of the energy levels converge to three crystal field configurations having relative energies  $E/Dq = 0, 10$ , and  $20$ .

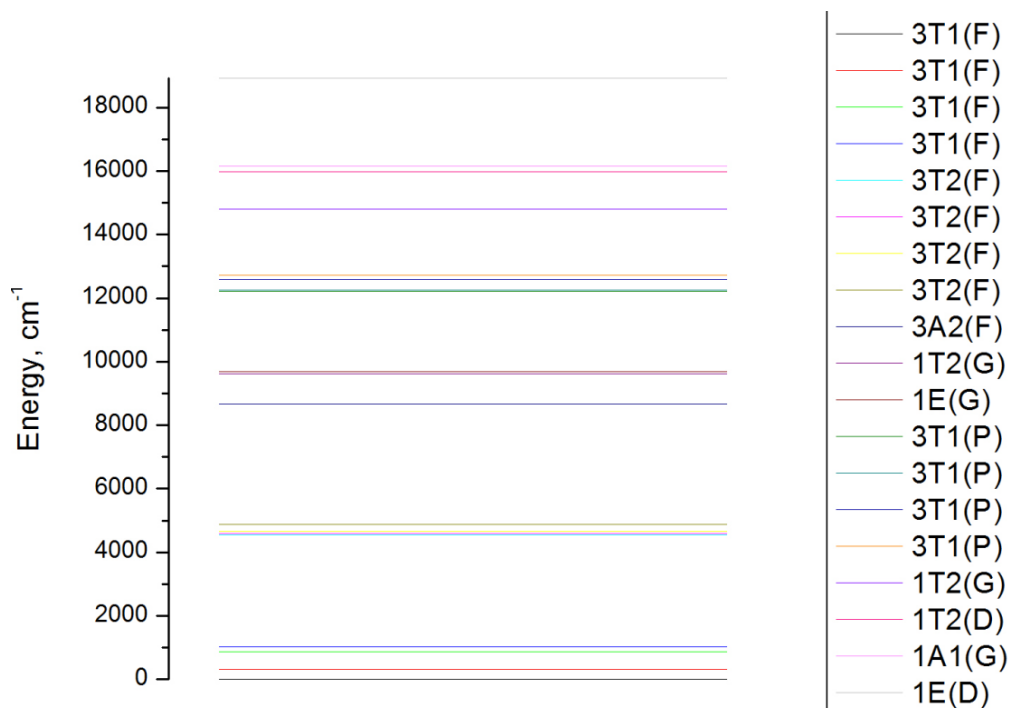


Figure 28. Diagram of  $\text{Ni}^{2+}:\text{ZnSe}$  energy levels (in  $\text{cm}^{-1}$ ).

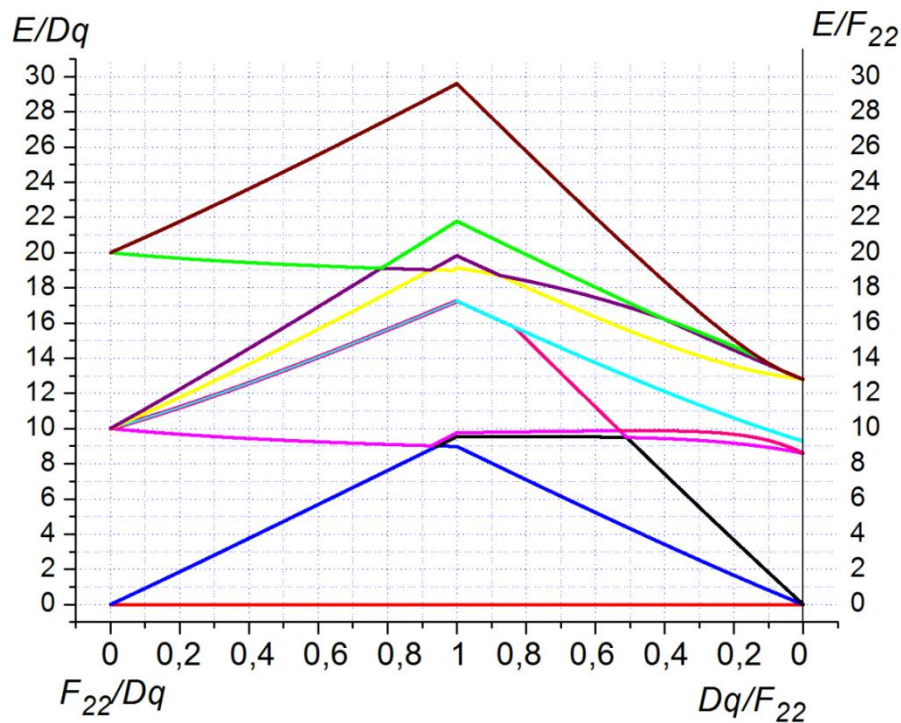
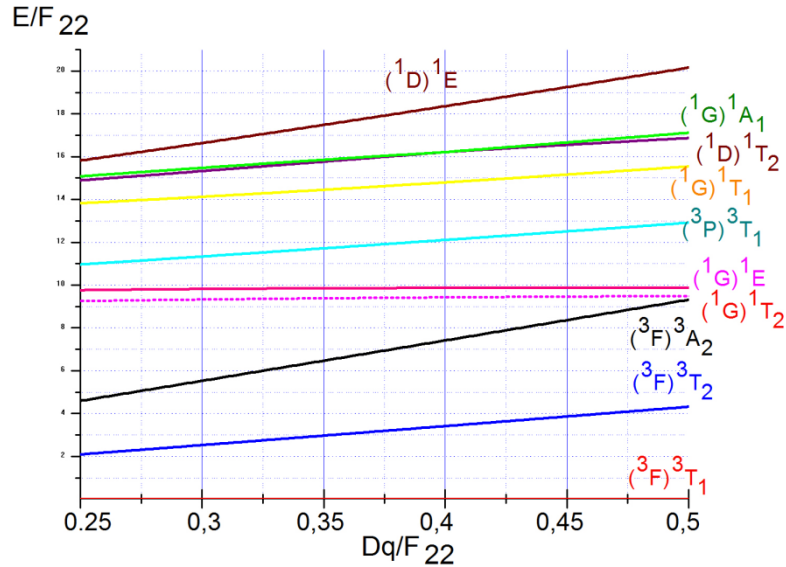


Figure 29.  $\text{Ni}^{2+}:\text{ZnSe}$  energy level diagram of  $E/Dq$  and  $E/F_{22}$  versus the relative parameter values  $F_{22}/Dq$  and  $Dq/F_{22}$  with no spin-orbital interaction  $\xi_{3d} = 0$ .

The right hand side of the diagram shown in Figure 29 corresponds to a weak crystal field where the electrostatic interaction parameters  $Dq/F_{22}$  changes from 0 to 1. At  $Dq/F_{22} = 0$ , the energy levels are equal to the energy levels of a free  $\text{Ni}^{2+}$  ion.

Because the parameter  $Dq/F_{22}$  changes from 0.25 to 0.5 in crystals of the type  $\text{A}^{\text{II}}\text{B}^{\text{VI}}$ , we plotted this region separately, see Figure 30.



**Figure 30. Energy levels of  $\text{Ni}^{2+}:\text{ZnSe}$  in terms of  $E/F_{22}$  versus the relative parameter  $Dq/F_{22} = 0.25\text{--}0.5$  at  $\xi_{3d} = 0$ .**

Shown in Table 9 are the strengths of the absorption transitions of  $\text{Ni}^{2+}$  in  $\text{ZnSe}$  for both the  $\pi$  and  $\sigma$  polarizations as well as the total polarization. State nominations are given in the following form:  $(^{2S+1}L)(^{2S+1}\Gamma_{J1})^{2S+1}\Gamma$ . A quantum number of the form  $^{2S+1}L$  for the state of a free  $\text{Ni}^{2+}$  ion is given in first parentheses in Table 9. Quantum numbers of the form  $^{2S+1}\Gamma_{J1}$  for a state of  $\text{Ni}^{2+}$  ion in a crystal field with consideration of the spin – orbit interaction is given in second parentheses of Table 9 and the resulting states  $^{2S+1}\Gamma$  are given without parentheses.

**Table 9. Strengths ( $f \cdot 10^7$ ) of the absorption transitions ( $J \rightarrow J'$ ) of  $\text{Ni}^{2+}$  in  $\text{ZnSe}$  for both  $\pi$  and  $\sigma$  polarizations as well as the total polarization (transitions occur from the base state  $J = ({}^3F)({}^3T_1){}^3A_1$ ).**

$N$	$J'$	$g$	$E(\text{cm}^{-1})$	$f-\pi (B_{21})$	$f-\sigma (B_{22})$	$f-(\sigma+2\pi)$
1	$({}^3F)({}^3T_1){}^3A_1$	1	0	0	0	0
2	$({}^3F)({}^3T_1){}^3T_1$	3	309	16387	19131	51905
5	$({}^3F)({}^3T_1){}^3E$	2	870	22288	34966	79542
7	$({}^3F)({}^3T_1){}^3T_2$	3	1020	81867	60862	224596
10	$({}^3F)({}^3T_2){}^3T_1$	3	4555	99376	53359	252112
13	$({}^3F)({}^3T_2){}^3E$	2	4593	178213	36583	393009
15	$({}^3F)({}^3T_2){}^3T_2$	3	4658	222948	24919	470815
18	$({}^3F)({}^3T_2){}^3A_2$	1	4882	88633	9449	186715

19	( <sup>3</sup> F) <sup>3</sup> A <sub>2</sub>	3	8593	182096	23538	387730
22	( <sup>1</sup> G) <sup>1</sup> E	2	9482	32908	7358	73173
24	( <sup>1</sup> G) <sup>1</sup> T <sub>2</sub>	3	9640	298994	36078	634066
27	( <sup>3</sup> P) <sup>3</sup> T <sub>1</sub>	2	11806	356359	438772	1151490
29	( <sup>3</sup> P) <sup>3</sup> T <sub>1</sub>	3	11858	688707	601059	1978473
32	( <sup>3</sup> P) <sup>3</sup> T <sub>1</sub>	3	12175	968688	492849	2430224
35	( <sup>3</sup> P) <sup>3</sup> T <sub>1</sub>	1	12308	316133	134627	766892
36	( <sup>1</sup> G) <sup>1</sup> T <sub>1</sub>	3	14603	19210	11303	49724
39	( <sup>1</sup> G) <sup>1</sup> A <sub>1</sub>	1	15730	5914	2790	14618
40	( <sup>1</sup> D) <sup>1</sup> T <sub>2</sub>	3	15930	5700	2071	13471
43	( <sup>1</sup> D) <sup>1</sup> E	2	18741	2715	3825	9255
45	( <sup>1</sup> S) <sup>1</sup> A <sub>1</sub>	1	34011	3152	7647	13951

The energies  $E$  and the oscillator strength  $f$  of the absorption spectra of  $\text{Ni}^{2+}$  in ZnSe for the total polarization are shown in Figure 31. Also shown in the figure are the transitions involved. Shown in Figure 32 are the energies  $E$  and oscillator strength  $f$  of the absorption spectra of  $\text{Ni}^{2+}$  in ZnSe for the  $\pi$  and  $\sigma$  polarizations.

The oscillator strength  $f$  is given by:

$$f = \sum_{m=1}^{m=45} h\nu f_m 10^4 \exp[-(h\nu - E_m^2)/s^2] \quad (50)$$

where  $s = 350 \text{ cm}^{-1}$ ,  $f_m = Q_m E_m$ ,  $Q_m = a_2 \sum_{n=1}^9 [U_2^2(n, m) + U_4^2(n, m)]$ , and  $a_2 = 3.56 \times 10^{-5}$ . Shown in Figure 33 is the oscillator strength  $f$  of the theoretical spectra for the  $\pi$  polarization (the upper red line) and the experimental spectra (the lower black line) in arbitrary units [14] for the absorption of  $\text{Ni}^{2+}$  in ZnSe in the wavelength region 0 – 2500 nm. Shown in Figure 34 is the oscillator strength  $f$  of the theoretical spectra for the  $\pi$  polarization (the upper red line) and the experimental spectra (the lower black line) in arbitrary units [14] for the absorption of  $\text{Ni}^{2+}$  in ZnSe in the wavelength  $\lambda$  region of 1000 – 2600 nm.

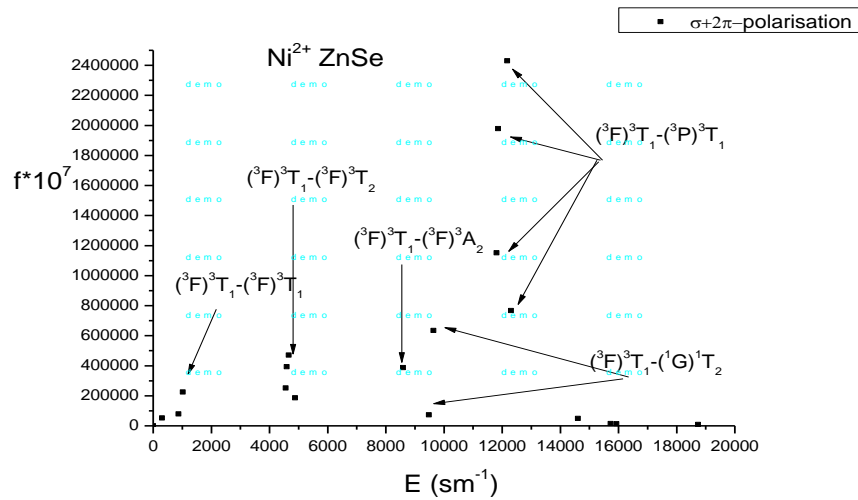


**Figure 31. The energies  $E$  and oscillator strength  $f$  for the absorption spectra of  $\text{Ni}^{2+}$  in ZnSe for the total polarization.**

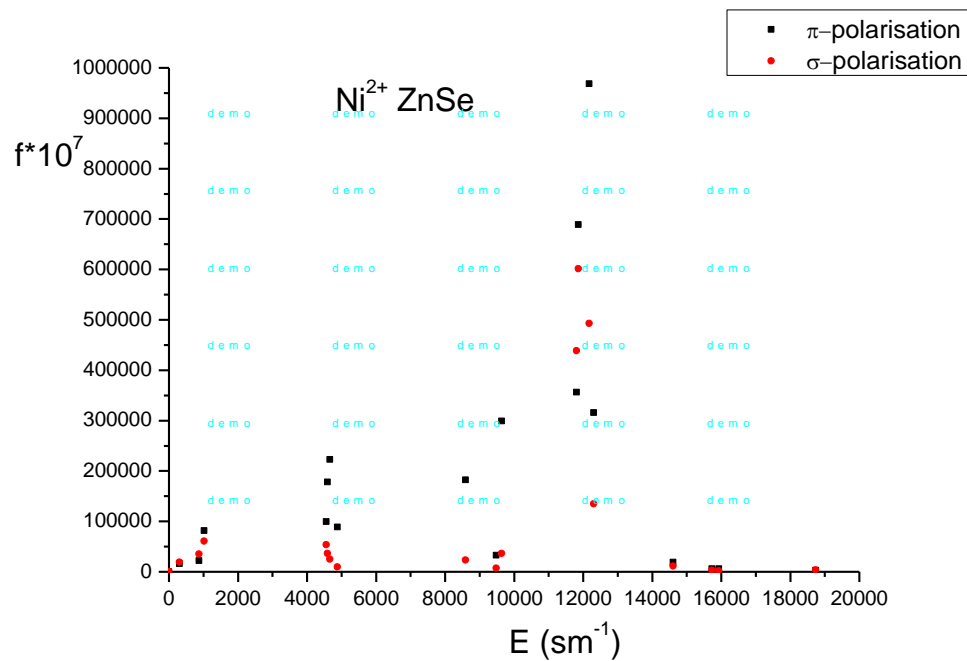


**Figure 32.** The energies  $E$  and oscillator strength  $f$  of the absorption spectra of  $\text{Ni}^{2+}$  in  $\text{ZnSe}$  for the  $\pi$  and  $\sigma$  polarizations.

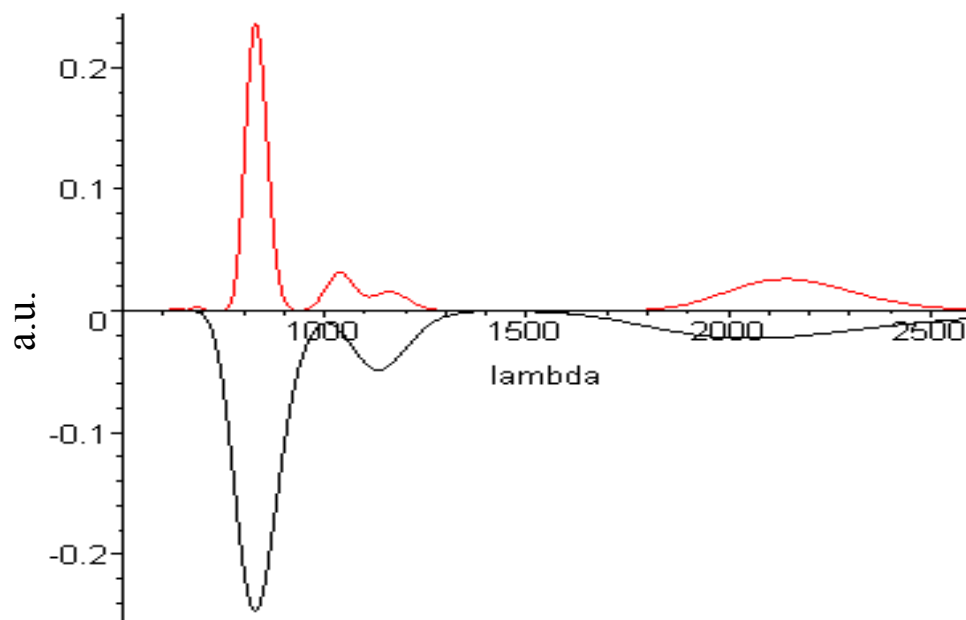


**Figure 33.** Oscillator strength  $f$  of the theoretical spectra for the  $\pi$  polarization (the upper red line) and the experimental spectra (the lower black line) in arbitrary units [14] for the absorption of  $\text{Ni}^{2+}$  in  $\text{ZnSe}$  in the wavelength region 0 – 2500 nm.

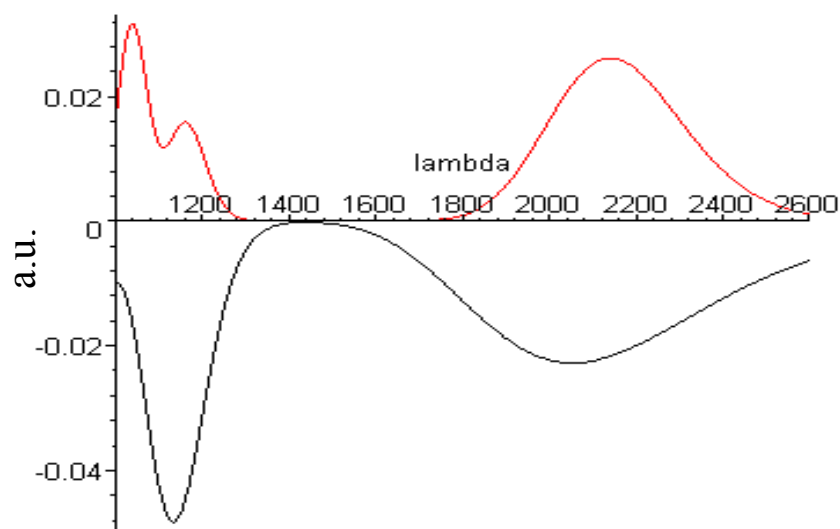


**Figure 34. Oscillator strength  $f$  of the theoretical spectra for the  $\pi$  polarization (the upper red line) and the experimental spectra (the lower black line) in arbitrary units [14] of absorption of  $\text{Ni}^{2+}$  in ZnSe in the wavelength  $\lambda$  region of 1000 – 2600 nm.**

### 3.16 Configuration coordinate model for the transition dynamics of $\text{Ni}^{2+}$ in ZnSe

The energy levels of  $\text{Ni}^{2+}$  in ZnSe versus the relative configuration coordinate  $r/R$  is presented in Figures 35-36. The major states are labeled in the diagram.

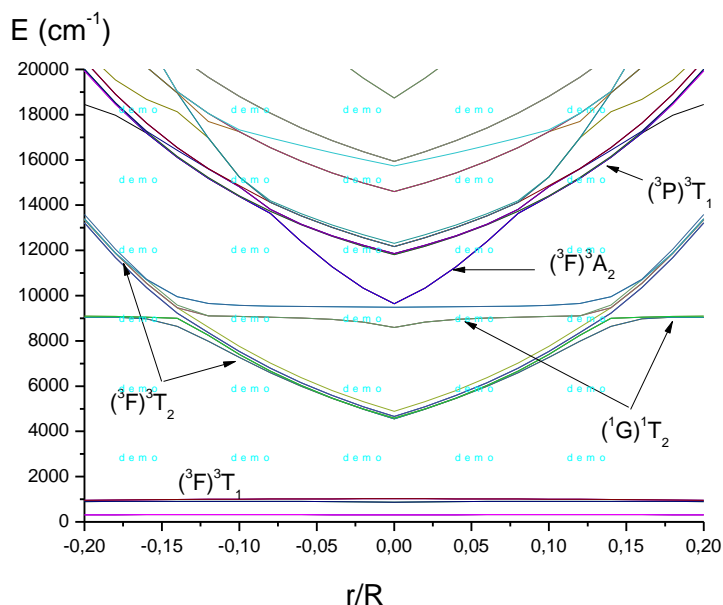


**Figure 35. Energy level diagram of  $\text{Ni}^{2+}$  in ZnSe versus the relative configuration coordinate  $r/R$ .**

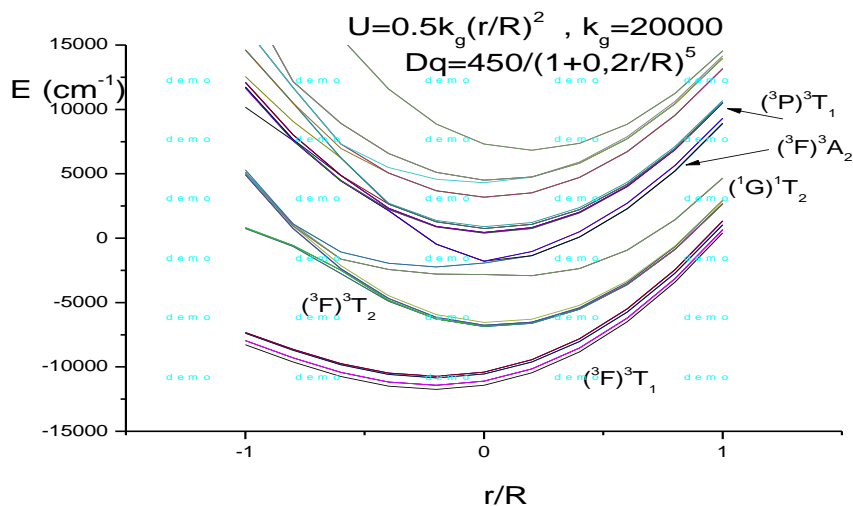


**Figure 36. Energy level diagram of  $\text{Ni}^{2+}$  in ZnSe versus the relative configuration coordinate  $r/R$ .**

To get a true picture of the influence of fluctuations on the energy characteristics of active ions, it is necessary to include in the Hamiltonian an operator representing the spherically symmetric interaction energy of the fluctuations according to formulas (36) and (37). In addition, it is necessary to include a modulation multiplier (38) in the crystal field parameter  $Dq$ .

Minimum values for the energies of the states and the associated configuration coordinates  $r/R$ , Table 10, were calculated using the electron phonon parameters  $k_g = 2000 \text{ cm}^{-1}$  and  $k = 0.2$ .

**Table 10. Minimum values of the energies of the states and the associated configuration coordinates  $r/R$  calculated with the following electron phonon parameters:  $k_g = 2000 \text{ cm}^{-1}$  and  $k = 0.2$**

$N$	States	$g$	$r/R$	$E_v(\text{cm}^{-1})$
1	$(^3F)(^3T_1)^3A_1$	1	-0.198	-11907
2	$(^3F)(^3T_1)^3T_1$	3	-0.198	-11907
5	$(^3F)(^3T_1)^3E$	2	-0.198	-11907
7	$(^3F)(^3T_1)^3T_2$	3	-0.198	-11907
10	$(^3F)(^3T_2)^3T_1$	3	0.0725	-6883
13	$(^3F)(^3T_2)^3E$	2	0.0725	-6883
15	$(^3F)(^3T_2)^3T_2$	3	0.0725	-6883
18	$(^3F)(^3T_2)^3A_2$	1	0.0725	-6883
19	$(^3F)^3A_2$	3	0.198	-2914
22	$(^1G)^1E$	2	0.0437	-1591
24	$(^1G)^1T_2$	3	0.0437	-1591
27	$(^3P)^3T_1$	2	0.0338	536
29	$(^3P)^3T_1$	3	0.0338	536
32	$(^3P)^3T_1$	3	0.0338	536
35	$(^3P)^3T_1$	1	0.0338	536

Shown in Figure 37 are the energy levels of  $\text{Ni}^{2+}$  in ZnSe for various  $k_g$  (quoted in the figure as “diag”) and  $k$  values.

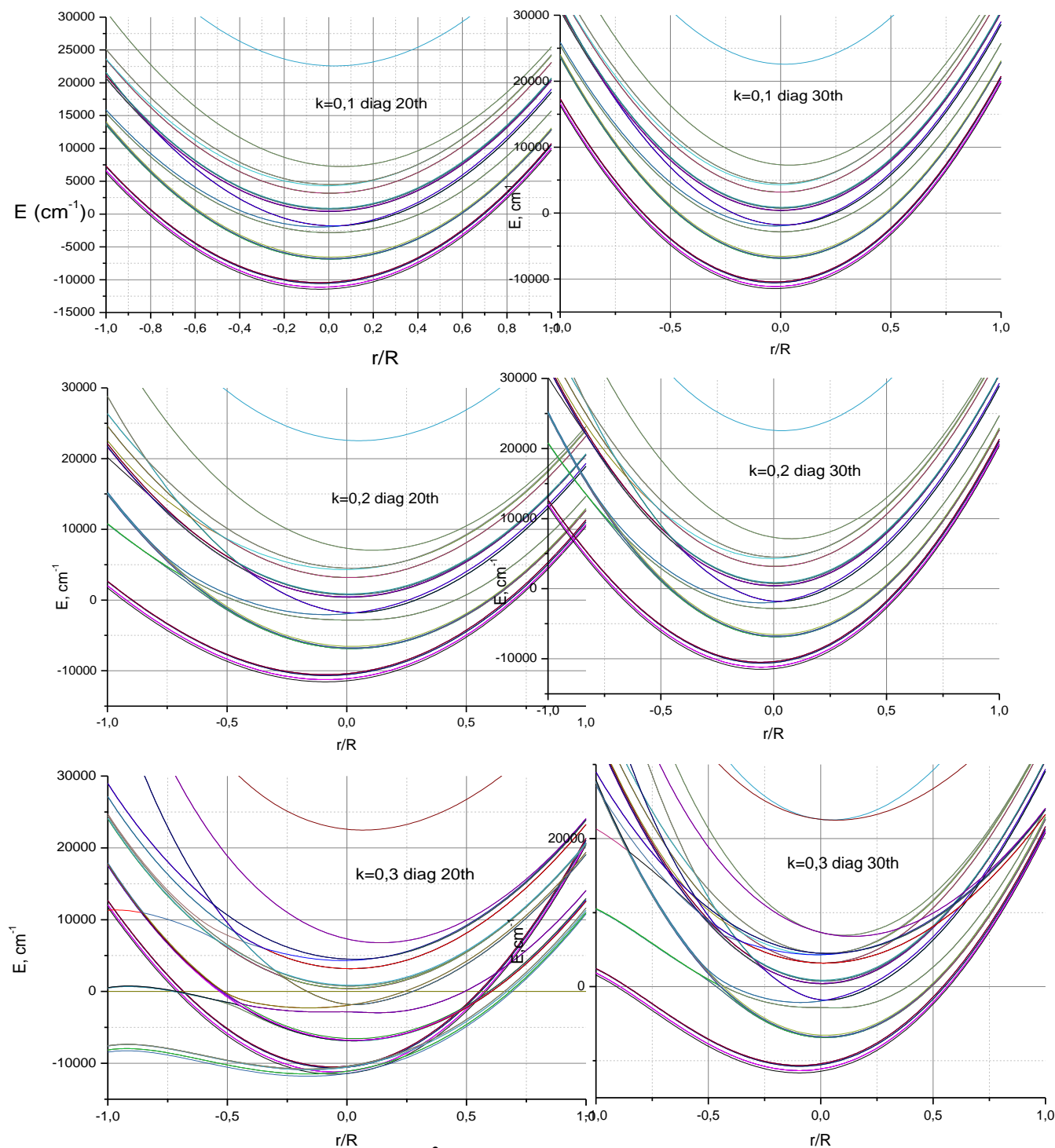


**Figure 37. Energy levels of  $\text{Ni}^{2+}$  in ZnSe for various  $k_g$  (quoted in the Fig. as “diag”) and  $k$  values.**



Finally, shown in Table 11 are the values for the energy levels of  $\text{Ni}^{2+}$  in ZnSe for the minimas of the relative configuration coordinate  $x_0$  of two states.

**Table 11. Values for the energy levels of  $\text{Ni}^{2+}$  in ZnSe for the minimas of the relative configuration coordinate  $x_0$  of the two states  $(^3\text{F})(^3\text{T}_1)\text{A}_1$ , and  $(^3\text{F})(^3\text{T}_2)\text{T}_1$ .**

$N$	SO levels	$g$	$x_0 = -0.218$	$x_0 = 0.186$
1	$(^3\text{F})(^3\text{T}_1)\text{A}_1$	1	-11703	-10523
10	$(^3\text{F})(^3\text{T}_2)\text{T}_1$	3	-5411	-7129

### 3.17 Spectral properties of $\text{Fe}^{2+}$ in ZnSe

The full interaction matrix of  $\text{Fe}^{2+}$  in ZnSe has a dimension of  $210 \times 210$ . Eigenvalues of this matrix and the intensity matrix are solved with the following parameters values:

Electrostatic and spin-orbital interactions:  $F_2 = 965$ ;  $F_4 = 76$ ;  $\xi_{3d} = -480$ ;  $B = F_2 - 5F_4$ ;  $C = 35F_4 = 2660$ ;  $C/B = 4.547$ ;

Crystal field parameters:  $Dq = 300$ ;  $A_{40} = 3\sqrt{70}Dq = 7530$ ;  $A_{44} = 15Dq = 4500$ ;  $A_{20} = A_{21} = A_{22} = A_{41} = A_{42} = A_{43} = 0$ ;

The intensity parameters:  $B_{20} = 0$ ;  $B_{40} = 0$ ;  $B_{44} = 0$ ;  $s_2 = 10$ ;  $s_3 = 100$ ;  $\varepsilon = 9n/(n^2+2)^2$ ;  $g = 12$ ;  $\tau = 108/10^6$ ;  $n = 2.44$ ;

Intensity parameters for  $\pi$  polarization:  $B_{21} = 1$ ;  $B_{41} = -2/\sqrt{40}B_{21} = -0.316$ ;  $B_{43} = \sqrt{7/\sqrt{10}}B_{21} = 0.837$ ;

Intensity parameters for  $\sigma$  polarization:  $B_{22} = 1$ ;  $B_{42} = 2/\sqrt{5}B_{22} = 0.894$ ;

Shown in Table 12 are the absorption energies and strengths of  $\text{Fe}^{2+}$  in ZnSe for both the total and ( $\pi$  and  $\sigma$ ) polarizations. The upper state excited along with its degeneracy is shown when known. Also, the transitions are assumed to occur from the base state  $(^5\text{D}_4)^5\text{A}_1$ .

**Table 12. Absorption spectra of  $\text{Fe}^{2+}$  ZnSe for both the total and ( $\pi$  and  $\sigma$ ) polarizations (transitions occur from the base state  $(^5\text{D}_4)^5\text{A}_1$ )**

$N$	States	$g$		$E(\text{cm}^{-1})$	$f(\pi) \cdot 10^7$	$f(\sigma) \cdot 10^7$	$f(2\pi+\sigma) \cdot 10^7$
1	$^5\text{D}_4$	1	$\text{A}_1$	0	0	0	0
2		3	$\text{T}_1$	29	35	82	153
5		2	E	57	46	107	198
7		3	$\text{T}_2$	97	122	275	519
10	$^5\text{D}_3$	1	$\text{A}_2$	139	59	133	250
11		3	$\text{T}_1$	2770	3131	52	6315
14		3	$\text{T}_2$	3029	2585	150	5319
17	$^5\text{D}_2$	2	E	3051	790	159	1740
19		3	$\text{T}_2$	3372	1964	30	3958

22	$^5D_1$	3	$T_1$	3402	1522	145	3190
25	$^5D_0$	1	$A_1$	3430	156	86	399
26	$^3H_6$	3	$T_2$	11600	21	46	87
29		1	$A_1$	11674	11	35	56
30		2	$E$	11682	20	51	91
32		3	$T_1$	11719	33	80	147
35		3	$T_2$	13437	12	0	24
38		3		13473	15	1	31
41	$^3H_6$	3		14050	22	27	72
44		2	$E$	14060	11	24	47
46		1	$A_2$	14280	10	7	26
47		3		14366	52	22	125
50	$^3H_4$	2	$E$	14500	15	19	48
52		3		14614	45	17	107
55		3		14675	16	19	51
58		1	$A_1$	14696	6	8	20
59	$^3P_2$	3		15464	100	0	200
62		3		15917	26	1	52
65	$^3F_4$	3		16394	12	7	30
68		1		16402	5	5	14
69		1		16403	2	2	7
70		3		16849	20	14	54
73	$^3F_3$	1		16934	3	7	12
74		1		16987	8	5	21
75		3		17001	18	7	43
78		3		17020	30	6	66
81	$^3F_2$	3		17157	9	10	28
84		1		17276	5	5	16
85	$^3G_5$	1		17278	8	6	22
86		3		17552	32	7	71
89		1		17708	11	2	24
90		1		18193	6	7	19

Shown in Figure 38 are the energy  $E$  and the oscillator strength  $f$  for the absorption spectra of  $\text{Fe}^{2+}$  in ZnSe for the  $\pi$  and  $\sigma$  polarizations as well as the total polarization. The transitions involves are labeled when known. In Figure 39, the energy  $E$  and oscillator strength  $f$  of the absorption spectra of  $\text{Fe}^{2+}$  in ZnSe are shown for only the total polarization. Known transitions are labeled in the figure. Shown in Figure 40 are the energy  $E$  and oscillator strength  $f$  of the absorption spectra of  $\text{Fe}^{2+}$  in ZnSe for the  $\sigma$  polarization. In Figure 41 are the energies  $E$  and oscillator strength  $f$  of the absorption spectra of  $\text{Fe}^{2+}$  in ZnSe for the  $\pi$  polarization. Finally, Figure 42 shows the oscillator strength  $f$  of the theoretical spectra for the  $\sigma$  polarization (the upper, red line) and the experimental data in arbitrary units (the lower, black line) [15] for the absorption spectra in the 2500 – 3500 nm spectral region of  $\text{Fe}^{2+}$  in ZnSe.

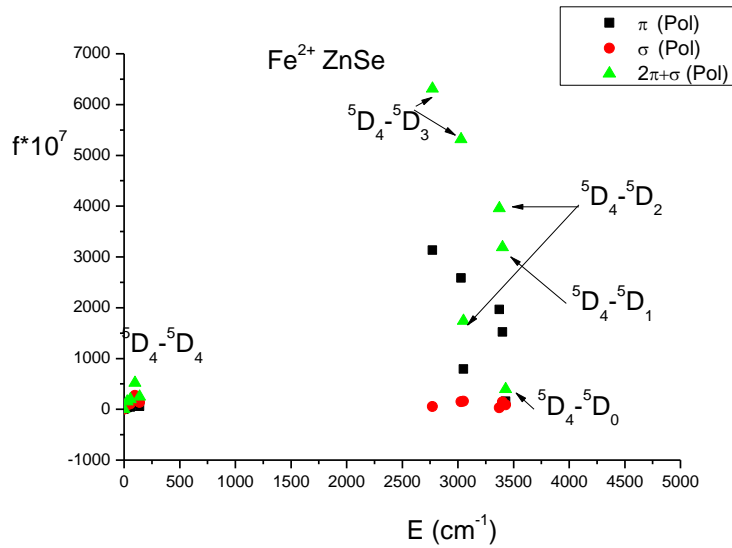


**Figure 38. The energy  $E$  and oscillator strength  $f$  of the absorption spectra of  $\text{Fe}^{2+}$  in ZnSe for the  $\pi$  and  $\sigma$  polarizations as well as the total polarization.**

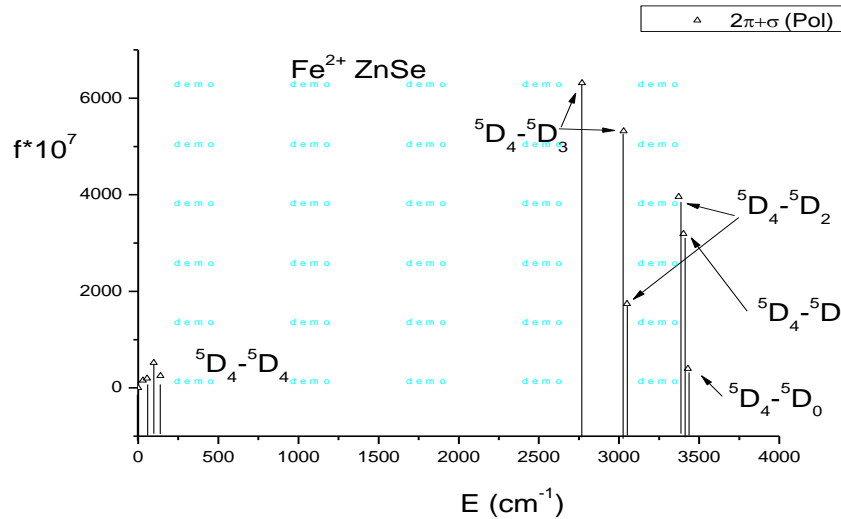


**Figure 39. Energy  $E$  and oscillator strength  $f$  of the absorption spectra of  $\text{Fe}^{2+}$  in ZnSe for the total polarization.**

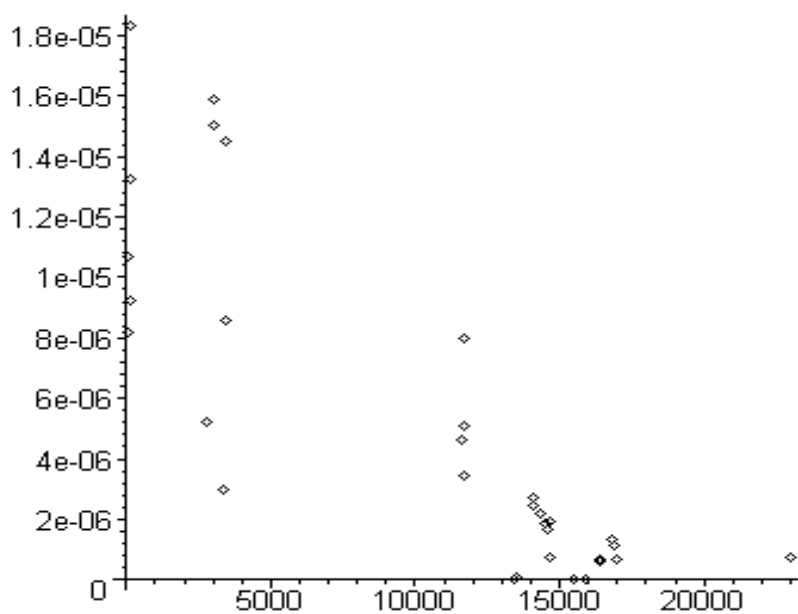


**Figure 40. Energy  $E$  and oscillator strength  $f$  of the absorption spectra of  $\text{Fe}^{2+}$  in ZnSe for the  $\sigma$  polarization.**

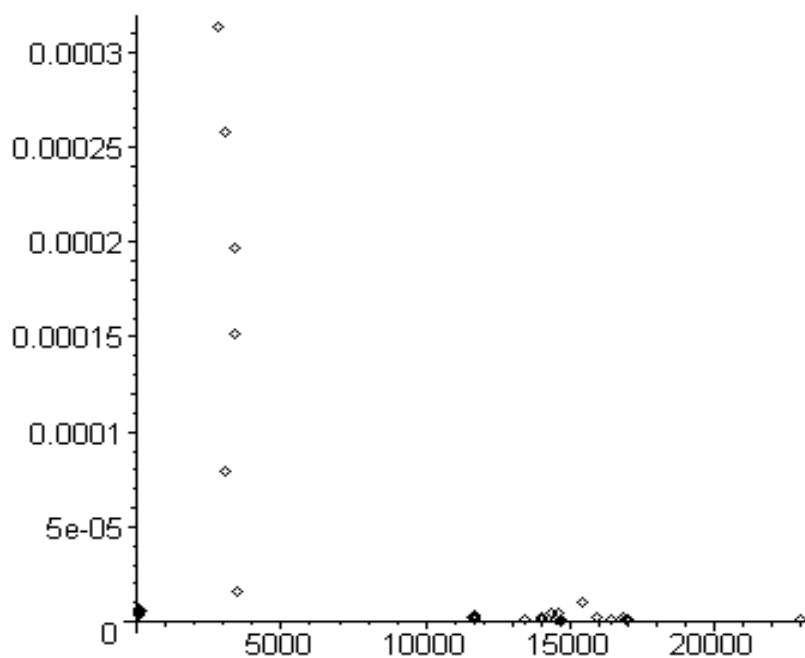


**Figure 41. Energy  $E$  and oscillator strength  $f$  of the absorption spectra of  $\text{Fe}^{2+}$  in ZnSe for the  $\pi$  polarization.**

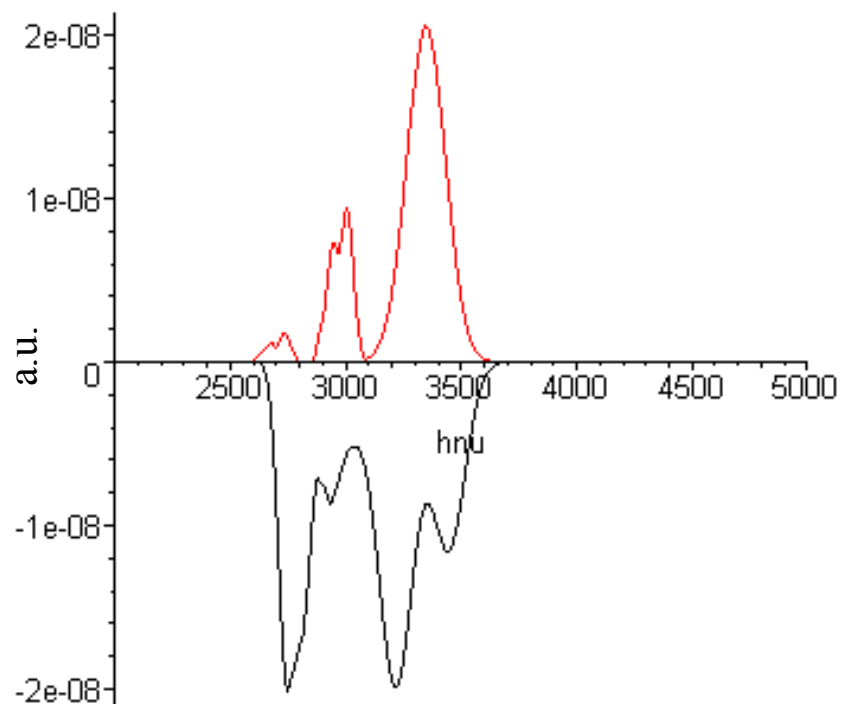


**Figure 42.** The oscillator strength  $f$  of the theoretical spectra for the  $\sigma$  polarization (the upper, red line) and the experimental data in arbitrary units (the lower, black line) [15] for the absorption spectra in the 2500 – 3500 nm region of  $\text{Fe}^{2+}$  in ZnSe.

### 3.18 Configuration coordinate model of transition dynamics of $\text{Fe}^{2+}$ in ZnSe

Shown in Figure 43 is a diagram of the energy levels of  $\text{Fe}^{2+}$  in ZnSe versus the relative configuration coordinate  $r/R$ . In Figure 44 is a diagram of the energy levels:  ${}^5\text{D}_4(\Gamma_8)$ ,  ${}^5\text{D}_3(\Gamma_8)$  and  ${}^3\text{H}_6(\Gamma_8)$  of  $\text{Fe}^{2+}$  in ZnSe versus the relative configuration coordinate  $x = r/R$ .

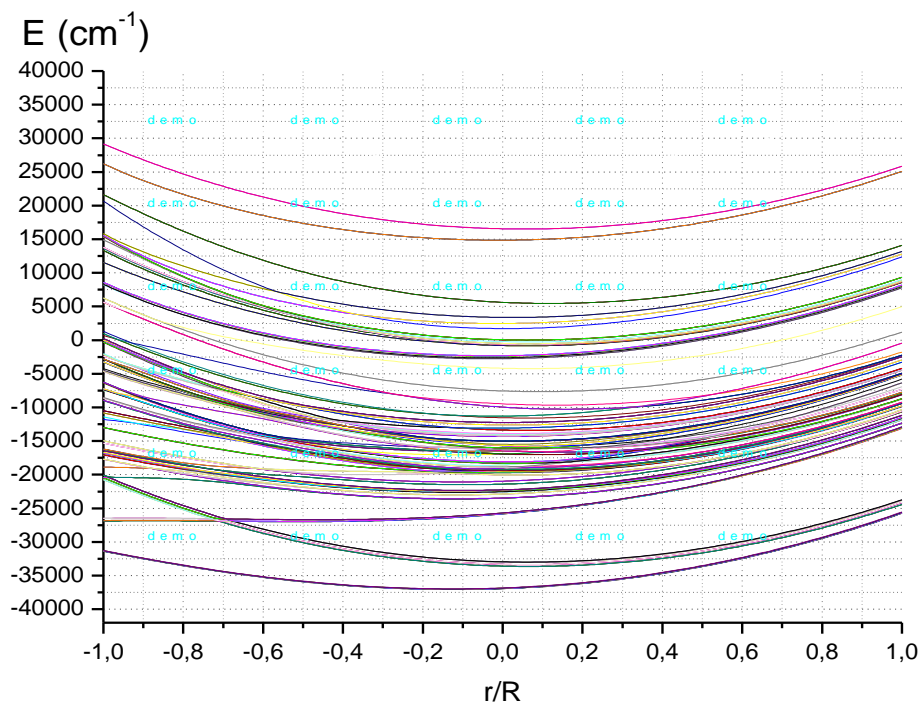


**Figure 43.** Diagram of the energy levels of  $\text{Fe}^{2+}$  in ZnSe versus the relative configuration coordinate  $r/R$ .

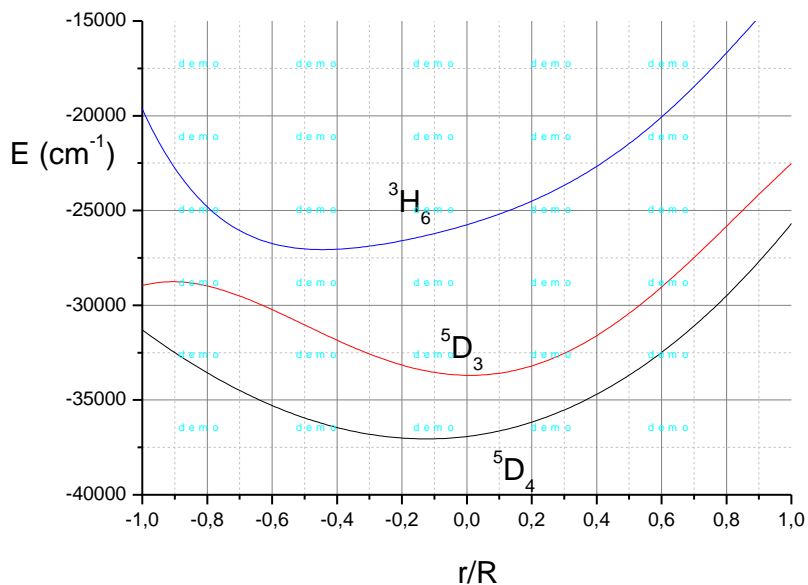


**Figure 44.** Diagram of the energy levels:  ${}^5\text{D}_4(\Gamma_8)$  (the lower curve),  ${}^5\text{D}_3(\Gamma_8)$  and  ${}^3\text{H}_6(\Gamma_8)$  (the upper curve) of  $\text{Fe}^{2+}$  in ZnSe versus the relative configuration coordinate  $x = r/R$ .

Shown in Table 13 are equations describing the energy levels of  $\text{Fe}^{2+}$  in ZnSe as a function of the relative configuration coordinate  $x = r/R$  when  $k = 0.2$ . In addition, the coordinates  $x_0$  and values of the energy minima  $E(x_0)$  for these levels are also shown in Table 13. Finally, shown in Table 14 are values of the energy levels of  $\text{Fe}^{2+}$  in ZnSe for the minima of the relative configuration coordinate  $x_0$  of three states  ${}^5\text{D}_4$ ,  ${}^5\text{D}_3$ , and  ${}^3\text{H}_6$ .

**Table 13. Equations of the energy levels of  $\text{Fe}^{2+}$  in ZnSe versus the relative configuration coordinate  $x = r/R$  when  $k = 0.2$ . Also shown are the coordinates  $x_0$  and values of the energy minimums  $E(x_0)$  for these levels.**

SO levels	Energies ( $\text{cm}^{-1}$ )	$x_0$	$E(x_0)$
${}^5\text{D}_4$	$735.2x^3+8430x^2+2069x-36924$	-0.125	-37052
${}^5\text{D}_3$	$-5204x^4+3485x^3+13155x^2-2622x-33695$	-0.096	-33322
${}^3\text{H}_6$	$-4666x^5+4648x^4+2927x^3+4448x^2+5113x-25752$	-0.461	-27143

**Table 14. Values of the energy levels of  $\text{Fe}^{2+}$  in ZnSe for the minima of the relative configuration coordinate  $x_0$  of the three states  ${}^5\text{D}_4$ ,  ${}^5\text{D}_3$ , and  ${}^3\text{H}_6$ .**

SO levels	$x_0 = -0.125$	$x_0 = -0.096$	$x_0 = -0.461$
${}^5\text{D}_4$	-37052	-37046	-36158
${}^5\text{D}_3$	-33171	-33322	-30267
${}^3\text{H}_6$	-26326	-26207	-27143

### 3.19 Overview of experimental data in literature

The goal of this section is to compare spectra from different sources in order to obtain values of the energy levels and linewidths. These values were then used in calculations throughout section 3 and the resulting spectra are given in the main body of the report.

We have considered the spectral properties of  $\text{Co}^{2+}$ ,  $\text{Ni}^{2+}$  and  $\text{Fe}^{2+}$  in ZnSe from a number of experimental works and have decided to digitize and plot them together on the same graph to enable a detailed analysis.

#### 3.19.1 Experimental spectra of $\text{Co}^{2+}$ in ZnSe.

For  $\text{Co}^{2+}$  ions in ZnSe, the experimental data as well as fits of this data are shown across various wavelength ranges in Figure 45.

For the lowest energy range, see Figure 45, we can see one peak at  $3420\text{-}3450\text{ cm}^{-1}$  (orange and green lines - data from ref. [1]). The black line (ref. [16]) has a main peak at  $3300\text{ cm}^{-1}$  and some smaller ones at  $3400$ ,  $3500$  and  $3660\text{ cm}^{-1}$ . Similarly, the violet line (ref. [17]) has a main peak at  $3280\text{ cm}^{-1}$  and three smaller ones at  $3350$ ,  $3580$  and  $3700\text{ cm}^{-1}$ .

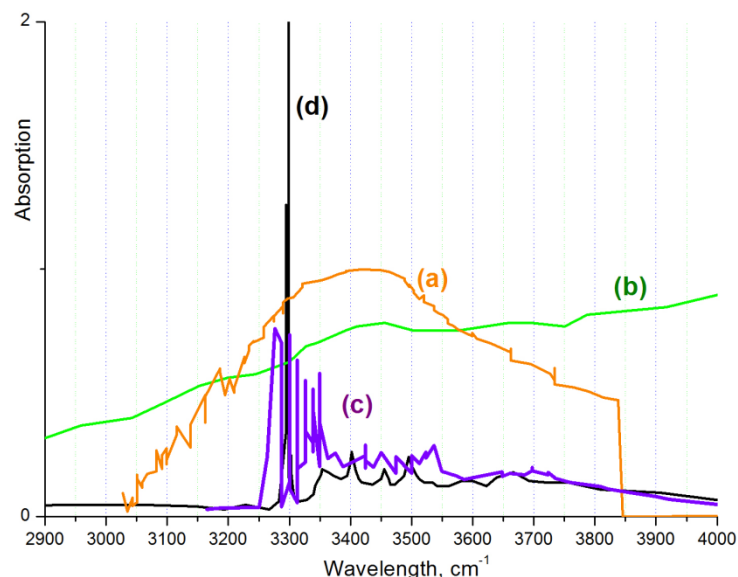


**Figure 45. Low energy experimental absorption spectra of  $\text{Co}^{2+}$  in ZnSe: orange line, (a) – ref. [1]; green line, (b) – ref. [1]; black line, (c) – ref. [16]; and violet line, (d) – ref. [17].**

In the next region,  $5000 - 7500 \text{ cm}^{-1}$ , see Figure 46, one more experimental curve appears, i.e., the cyan line which is data from ref. [18]. However, this data displays a flat behavior because of the lack of cooling. This is quite a bit different from the other work where there was cooling, i.e., the temperature was  $77^\circ\text{K}$  in the work of ref. [1], and the temperature was  $10^\circ\text{K}$  in the work of ref. [16] and [17].

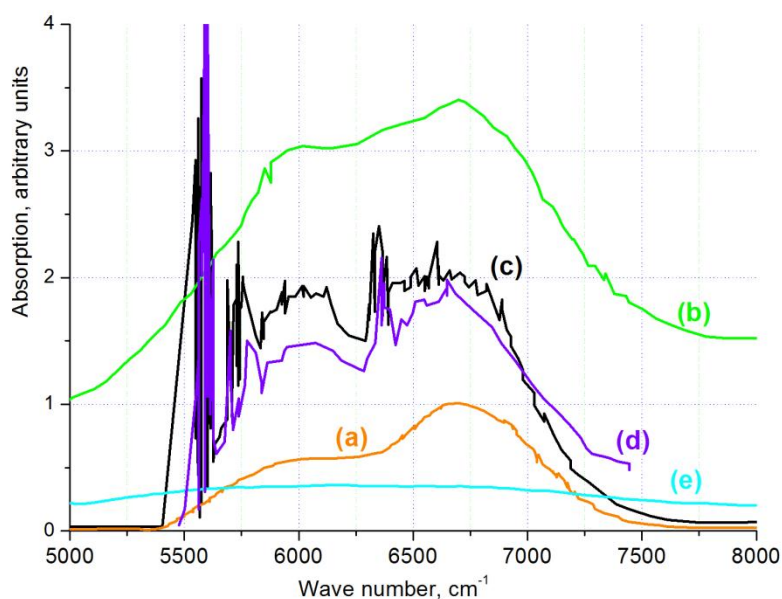


**Figure 46. Infrared absorption spectra in the  $5000\text{-}7500 \text{ cm}^{-1}$  spectral region of  $\text{Co}^{2+}$  in ZnSe: orange line, (a) – ref. [1]; green line, (b) – ref. [1]; black line, (c) – ref. [16]; violet line, (d) – ref. [17]; cyan line, (e) – ref. [18].**



We start with fitting the experimental curves (a) and (b) in Figure 46. In Figure 47, the experimental curves (a) and (b) are shown together with curves obtained by fitting the data with the sum of two Gaussian functions. The expressions used in the fits are:

$$\text{Fit(a, [1])} = 0.00538 + 0.5123 \cdot \text{Exp}(-0.5 \cdot [(x - 5935)/255]^2) + 0.9941 \cdot \text{Exp}(-0.5 \cdot [(x - 6724)/312]^2) \quad (51)$$

$$\text{Fit(b, [1])} = 1.2278 + 0.9433 \cdot \text{Exp}(-0.5 \cdot [(x - 5854)/267]^2) + 2.1111 \cdot \text{Exp}(-0.5 \cdot [(x - 6640)/498]^2) \quad (52)$$

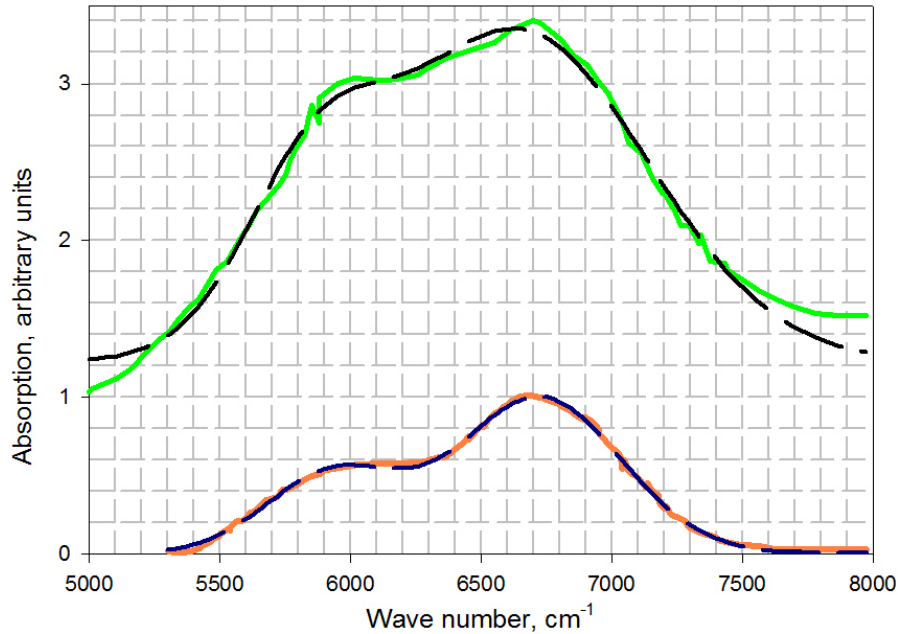


**Figure 47. Infrared absorption spectra in the 5000-7500 cm<sup>-1</sup> spectral region of Co<sup>2+</sup> in ZnSe: orange line, (a) – ref. [1]; green line, (b) – ref. [1]; together with curve fits (black dashes).**

Now we separately present fit results for the data in curves (c) and (d), see Figure 48 and 49, respectively. In Figures 48 and 49, we show the fit of the experimental data in reference [16] (Figure 46, curve (c)). We also demonstrate the similarity of the spectra from reference [16], curve (c) and reference [17], curve (d) in Figure 49. The expressions used in the fits are:

$$\text{Fit(c, [16])} = 0.0532 + 1.8245 \cdot \text{Exp}(-0.5 \cdot [(x - 5574)/42]^2) + 0.8648 \cdot \text{Exp}(-0.5 \cdot [(x - 5744)/46]^2) + 1.6035 \cdot \text{Exp}(-0.5 \cdot [(x - 5963)/193]^2) + .5057 \cdot \text{Exp}(-0.5 \cdot [(x - 6347)/25]^2) + 2.0427 \cdot \text{Exp}(-0.5 \cdot [(x - 6642)/330]^2) \quad (53)$$

$$\text{Fit(d, [17])} = 0.409 + 2.077 \cdot \text{Exp}(-0.5 \cdot [(x - 5588)/13]^2) + 0.54 \cdot \text{Exp}(-0.5 \cdot [(x - 5635)/68]^2) + 0.99 \cdot \text{Exp}(-0.5 \cdot [(x - 5792)/14]^2) + 0.9124 \cdot \text{Exp}(-0.5 \cdot [(x - 5966)/174]^2) + 0.50 \cdot \text{Exp}(-0.5 \cdot [(x - 6364)/20]^2) + 1.46 \cdot \text{Exp}(-0.5 \cdot [(x - 6654)/323]^2) \quad (54)$$

Summarizing, in this infrared interval, we observe two peaks (at about 5580 and 6650  $\text{cm}^{-1}$ ) with greater intensity plus 3 – 4 peaks of lesser intensity.

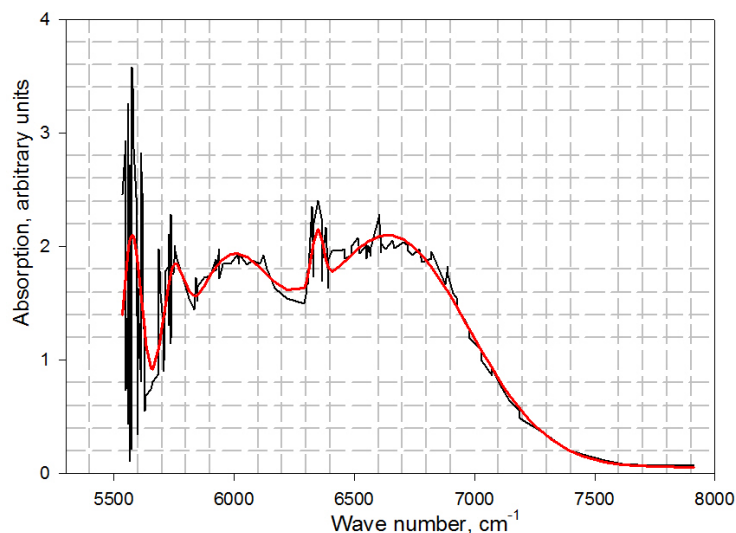


**Figure 48. Infrared absorption spectra in the 5000-7500  $\text{cm}^{-1}$  spectral region of  $\text{Co}^{2+}$  in ZnSe. Experimental data is taken from ref. [16] and is represented by the black line and the curve fit is represented by the red line.**

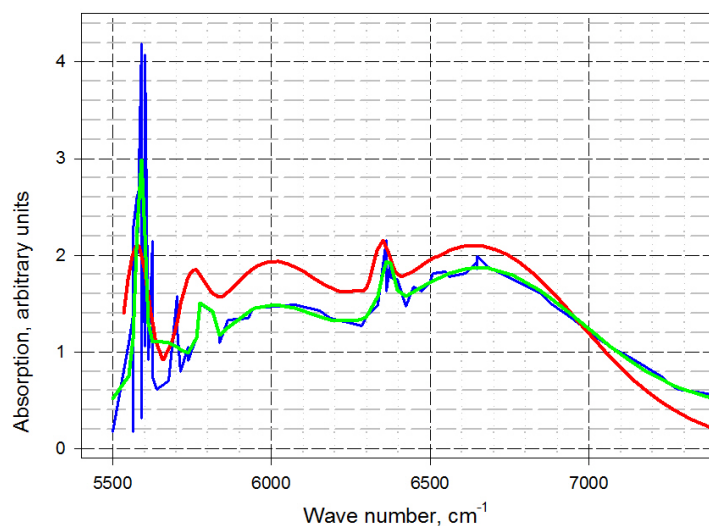


**Figure 49. Infrared absorption spectra in the 5000-7500  $\text{cm}^{-1}$  spectral range of  $\text{Co}^{2+}$  in ZnSe. The experimental data from ref. [17] is represented by the blue line with its fit represented by the green line. The experimental data from ref. [16] (curve c) is also fit and is represented by the red line.**

There is also some evidence of a peak found only in paper [17], see Figure 50, where the Gaussian fit is defined to be:

$$\text{Fit}([17]) = 0.005 + 0.011 \cdot \exp(-0.5 \cdot [(x - 11550)/40]^2). \quad (55)$$

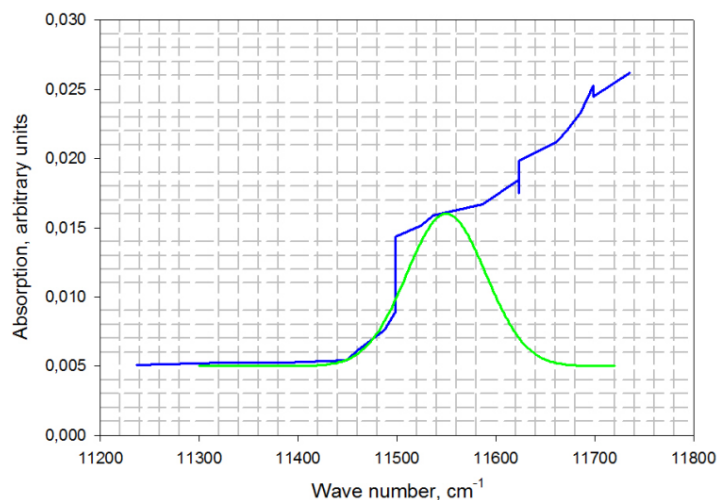


**Figure 50. Spectra of  $\text{Co}^{2+}$  in ZnSe from 11200 to 11800  $\text{cm}^{-1}$  from ref. [17] (blue line) and the Gaussian fit to the peak (green line).**

Further, there are two more peaks that are only found in refs. [16] and [17], see Figure 51. The fits to these peaks are as follows:

$$\begin{aligned} \text{Fit}(c, [16]) = & 0.3246 + 0.0584 \cdot \exp(-0.5 \cdot [(x - 12151)/27]^2) \\ & + 0.0908 \cdot \exp(-0.5 \cdot [(x - 12361)/134]^2) \end{aligned} \quad (56)$$

$$\begin{aligned} \text{Fit}(d, [17]) = & 0.04 + 0.0337 \cdot \exp(-0.5 \cdot [(x - 12145)/31]^2) \\ & + 0.0908 \cdot \exp(-0.5 \cdot [(x - 12386)/207]^2) \end{aligned} \quad (57)$$

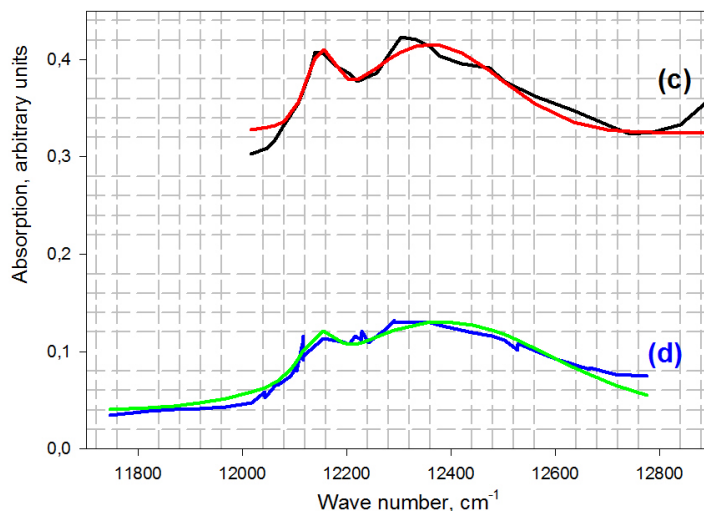


**Figure 51. Spectra of  $\text{Co}^{2+}$  in ZnSe from 1180 to 12800  $\text{cm}^{-1}$ : (c), black line – experimental data from ref. [16] and its fit (red line); (d) – experimental data from ref. [17] (blue line) and its fit (green line).**

Shown in Figure 52 are various experimental absorption spectra in the visible region from the scientific literature. In order to visualize all of the spectra on one graph, part of the spectrum from ref. [17] was divided by a factor of ten. The spectrum in ref. [17] demonstrates the richest behavior, and thus in the next two figures, we present a mathematical fit to it.

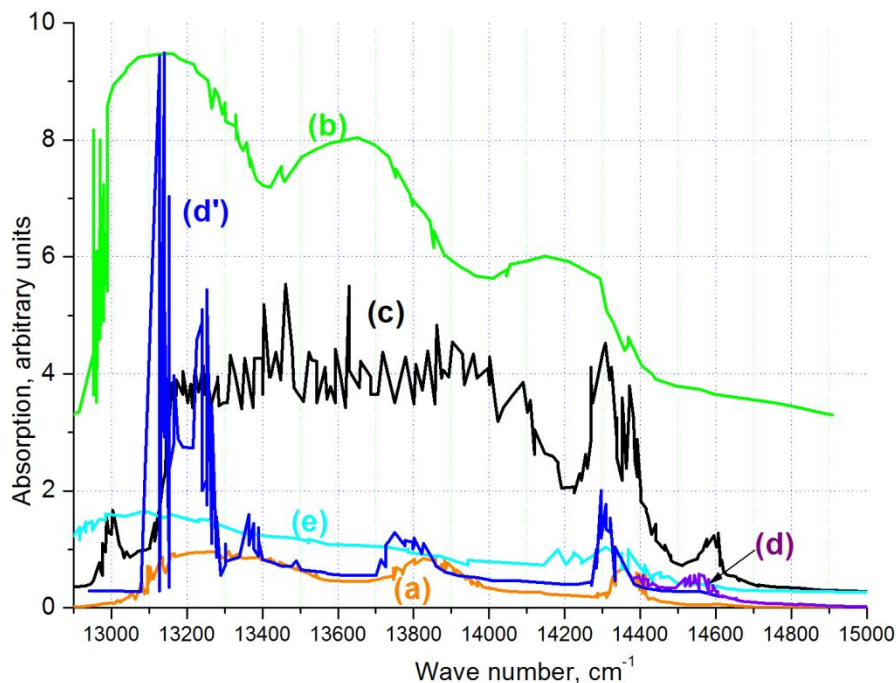


**Figure 52. Absorption spectra of  $\text{Co}^{2+}$  in ZnSe in visible region: orange line, (a) – ref. [1]; green line, (b) – ref. [1]; black line, (c) – ref. [16]; violet line, (d) – ref. [17], blue line (d') – data from ref. [17] multiplied by a factor of 0.1; cyan line, (e) – ref. [18].**

For the spectrum shown in Figure 53 between  $13000$  and  $14600 \text{ cm}^{-1}$ , five main peaks are identified and the fit to these peaks is described as:

$$\begin{aligned} \text{Fit}([17]) = & 0.0275 + 0.2871 * \text{Exp}(-0.5 * [(x - 13137)/12]^2) + \\ & 0.1663 * \text{Exp}(-0.5 * [(x - 13227)/38]^2) + 0.0413 * \text{Exp}(-0.5 * [(x - 13371)/23]^2) + \\ & 0.0316 * \text{Exp}(-0.5 * [(x - 13778)/51]^2) + 0.0640 * \text{Exp}(-0.5 * [(x - 14306)/14]^2), \end{aligned} \quad (58)$$

For the spectrum shown in Figure 54 between  $14400$  and  $15400 \text{ cm}^{-1}$ , two peaks have been identified and their fit is described as:

$$\begin{aligned} \text{Fit}([17]) = & 0.02 + 0.4722 * \text{Exp}(-0.5 * [(x - 14382)/44]^2) + 0.4411 * \\ & \text{Exp}(-0.5 * [(x - 14538)/67]^2). \end{aligned} \quad (59)$$

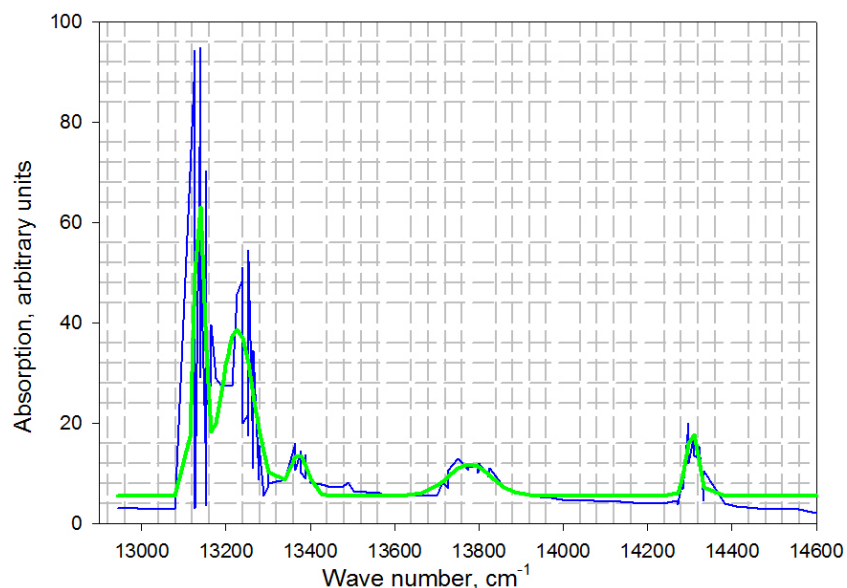


**Figure 53. Absorption spectra of  $\text{Co}^{2+}$  in ZnSe in the visible region from 13000 to 14600  $\text{cm}^{-1}$ : experimental data from ref. [17] (blue line) and its fit by the sum of five Gaussian functions (green line).**

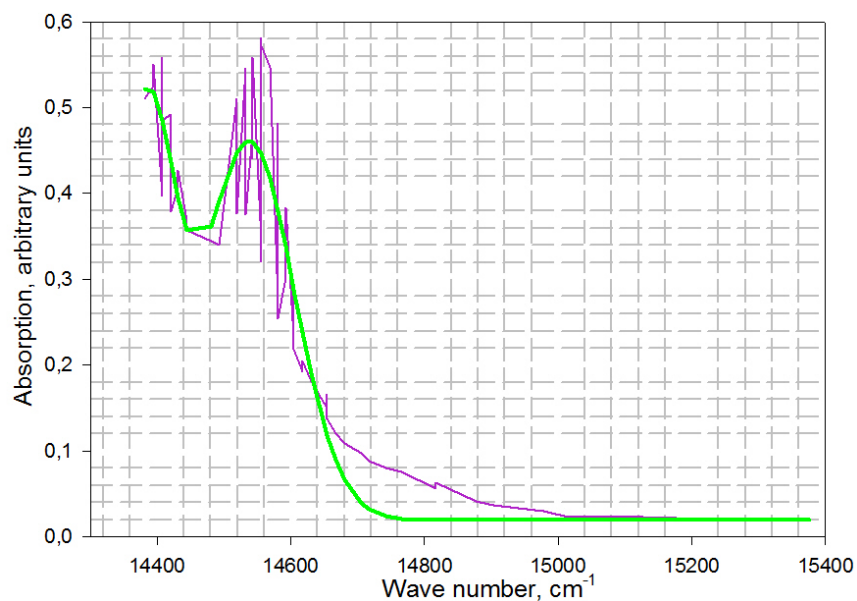


**Figure 54. Absorption spectra of  $\text{Co}^{2+}$  in ZnSe in visible region from 14400 to 15400  $\text{cm}^{-1}$ : experimental data from ref. [17] (violet line) and its fit by the sum of two Gaussian function (green line).**

Absorption spectra are given in references [16] and [17] for the next frequency range from 15000 – 18000  $\text{cm}^{-1}$ . For the experimental data from reference [16] shown in Figure 55, the mathematical fit is described by:

$$\text{Fit}([16]) = 0.2702 + 0.0742 \exp(-0.5 * [(x - 16076)/111]^2) + 0.0311 * \exp(-0.5 * [(x - 16580)/221]^2) + 0.0211 \exp(-0.5 * [(x - 17123)/111]^2); \quad (60)$$

and the mathematical fit to similar data from reference [17], shown in Figure 56, is given by:

$$\text{Fit}([17]) = 0.0083 + 0.0535 \exp(-0.5 * [(x - 16067)/118]^2) + 0.0247 * \exp(-0.5 * [(x - 16602)/284]^2) + 0.0122 \exp(-0.5 * [(x - 17096)/103]^2). \quad (61)$$

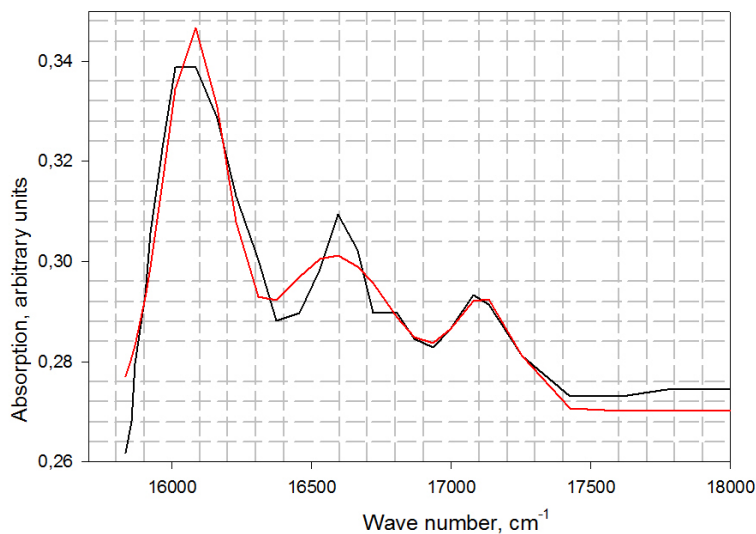


**Figure 55. Absorption spectra of  $\text{Co}^{2+}$  in ZnSe from 15500 to 18000  $\text{cm}^{-1}$ : experimental data from ref. [16] (black line) and its fit by the sum of three Gaussian functions (red line).**

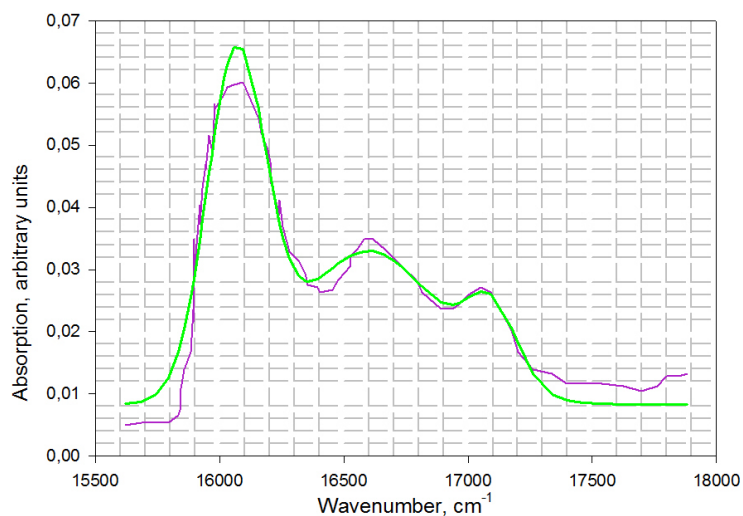


**Figure 56. Absorption spectra of  $\text{Co}^{2+}$  in ZnSe from 15500 to 18000  $\text{cm}^{-1}$ : experimental data from ref. [17] (violet line) and its fit by the sum of three Gaussian functions (green line).**

The experimental spectra of the high energy region from 18750 to 20750  $\text{cm}^{-1}$  is given in references [1, 16, 17] and is shown in Figure 57.

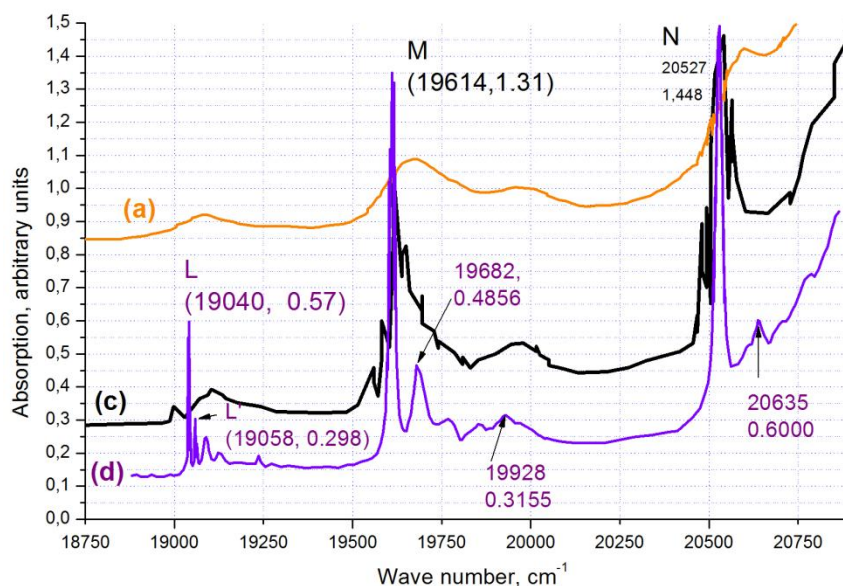


**Figure 57. High-energy absorption spectra of  $\text{Co}^{2+}$  in ZnSe from 18750 to 20750  $\text{cm}^{-1}$ : orange line, (a) – ref. [1]; black line, (c) – ref. [16]; violet line, (d) – ref. [17].**

We have separately fit the three experimental lines presented in Figure 57 and have obtained the following expressions for the fits:

For line (a), ref. [1] (see Figure 58):

$$\begin{aligned} \text{Fit(a, [1])} = & 0.8414 + 0.065 \text{Exp}(-0.5 * [(x - 19099)/104]^2) + \\ & 0.1418 \text{Exp}(-0.5 * [(x - 19660)/70]^2) + 0.1514 * \text{Exp}(-0.5 * [(x - \\ & 19986)/362]^2) + 0.5602 \text{Exp}(-0.5 * [(x - 20629)/111]^2); \end{aligned} \quad (62)$$

For line (c) – ref. [16] (see Figure 59):

$$\begin{aligned} \text{Fit(c, [16])} = & 0.2843 + 0.089 \text{Exp}(-0.5 * [(x - 19124)/85]^2) + 0.4457 * \\ & \text{Exp}(-0.5 * [(x - 19634)/38]^2) + 0.2351 \text{Exp}(-0.5 * \\ & [(x - 19933)/286]^2) + 0.8643 \text{Exp}(-0.5 * [(x - 20572)/82]^2); \end{aligned} \quad (63)$$

For line (d) – ref. [17] (see Figure 60):

$$\begin{aligned} \text{Fit(d, [17])} = & 0.0678 + 0.3308 \text{Exp}(-0.5 * [(x - 19041)/2]^2) + 0.9657 * \\ & \text{Exp}(-0.5 * [(x - 19611)/7]^2) + 0.1465 * \text{Exp}(-0.5 * \\ & [(x - 19700)/105]^2) + 1.0048 \text{Exp}(-0.5 * [(x - 20528)/9]^2). \end{aligned} \quad (64)$$



Due to the sharp peaks in the last spectrum (line (d)), it is probably more accurate to use the peaks as specified in Figure 57: **19040**, **19058**, **19614**, **19682**, **19928**, **20527**, and **20635** rather than the maximums of the fit.

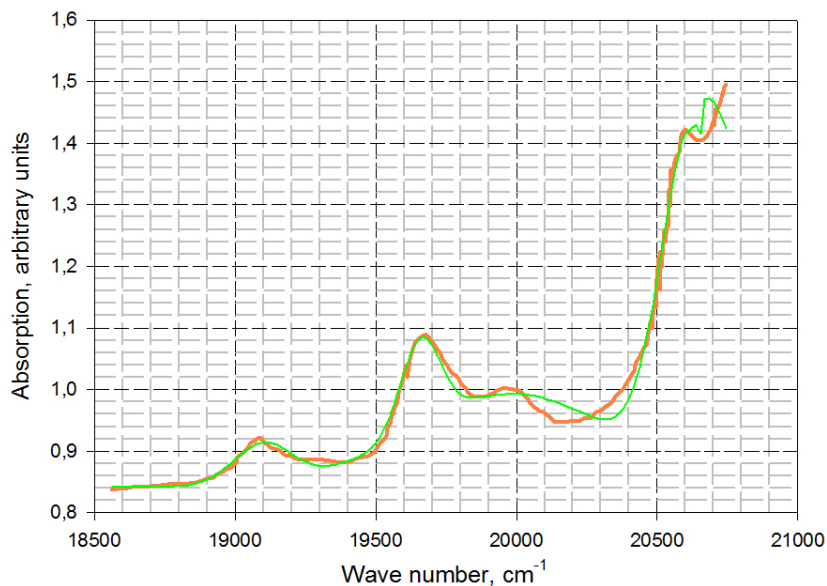


**Figure 58.** Absorption spectra of  $\text{Co}^{2+}$  in ZnSe from 18500 to 21000  $\text{cm}^{-1}$ : orange line – experimental data taken from ref. [1]; green line – the mathematical fit.

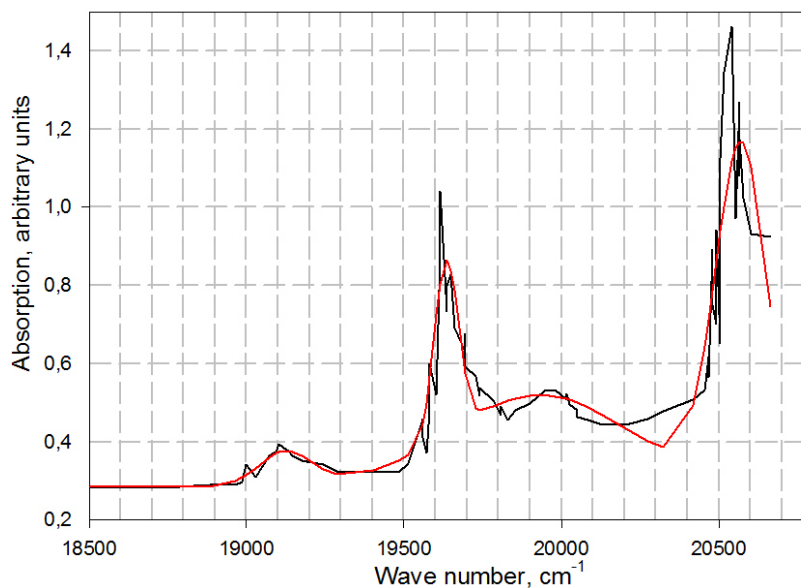


**Figure 59.** Absorption spectra of  $\text{Co}^{2+}$  in ZnSe from 18500 to 21000  $\text{cm}^{-1}$ : black line – experimental data taken from ref. [16]; red line – the mathematical fit.



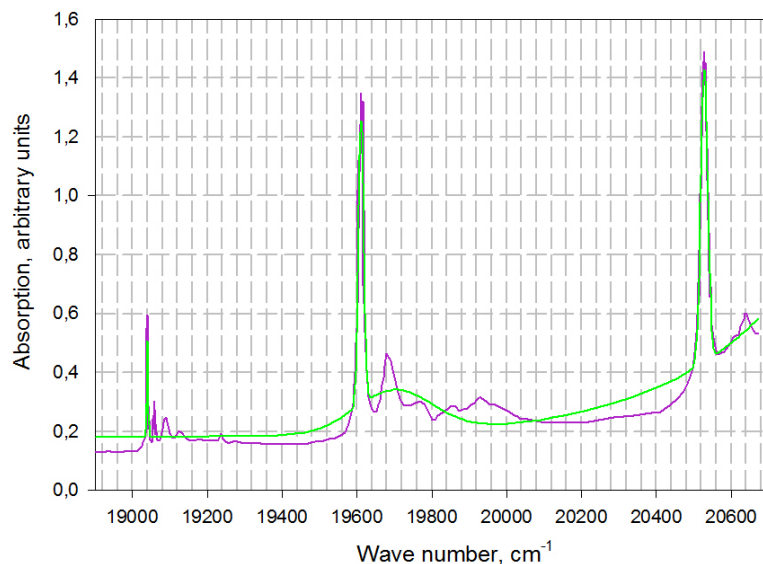


**Figure 60. Absorption spectra of  $\text{Co}^{2+}$  in ZnSe from 18500 to 21000  $\text{cm}^{-1}$ : violet line – experimental data taken from ref. [17]; green line – the mathematical fit.**

And finally, we digitized and converted the experimental data on luminescence taken from reference [16] to  $\text{cm}^{-1}$ , see Figure 61, where the maximum values for each peak are shown. (The red plus signs signify the location of the maximum of each peak.).

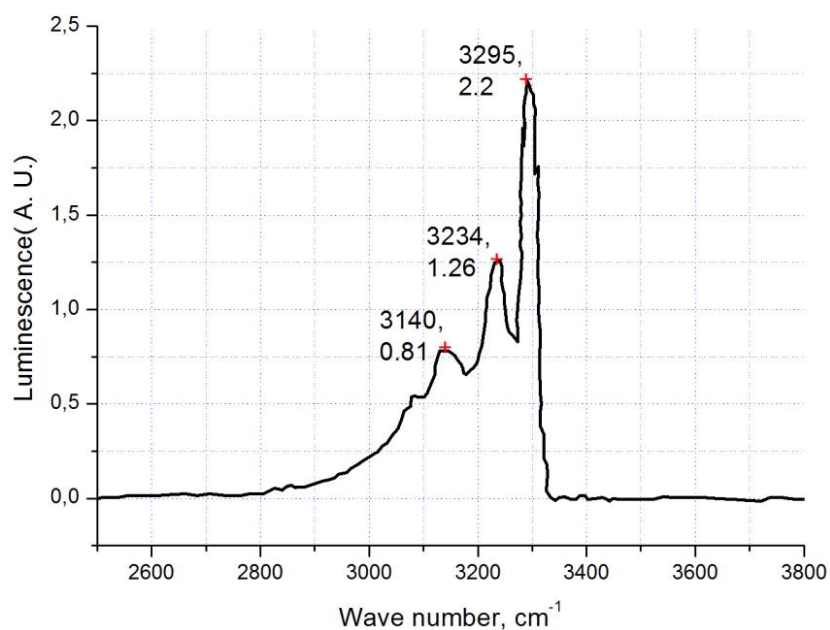


**Figure 61. Luminescence spectra of  $\text{Co}^{2+}$  in ZnSe over the 2500 to 2800  $\text{cm}^{-1}$  spectral range (experimental data were taken from paper [16]).**

### 3.19.2 Experimental spectra of $\text{Ni}^{2+}$ in ZnSe.

Unfortunately, the literature does not contain much experimental absorption and luminescence spectral data for  $\text{Ni}^{2+}$  in ZnSe. Of the three ions in this study, the smallest amount of experimental work has been performed on  $\text{Ni}^{2+}:\text{ZnSe}$ .

Let us consider an experimental spectrum from the classical work in reference [14] on  $\text{Ni}^{2+}:\text{ZnSe}$ , see Figure 62. As before, we performed a fit, in this case, by the summation of three Gaussian curves, see Figure 63.

$$\text{Fit} = 7.97 \cdot \text{Exp}(-0.5 \cdot [(x - 4871)/639]^2) + 16.98 \cdot \text{Exp}(-0.5 \cdot [(x - 8827)/523]^2) + 86.54 \cdot \text{Exp}(-0.5 \cdot [(x - 12083)/767]^2) \quad (65)$$

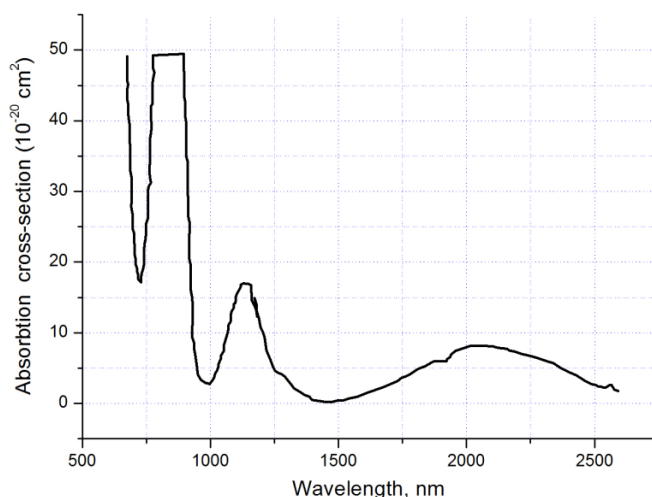


**Figure 62.** Absorption spectra of  $\text{Ni}^{2+}$  in ZnSe over the 500 to 2500  $\text{nm}^{-1}$  spectral range, taken from reference [14].

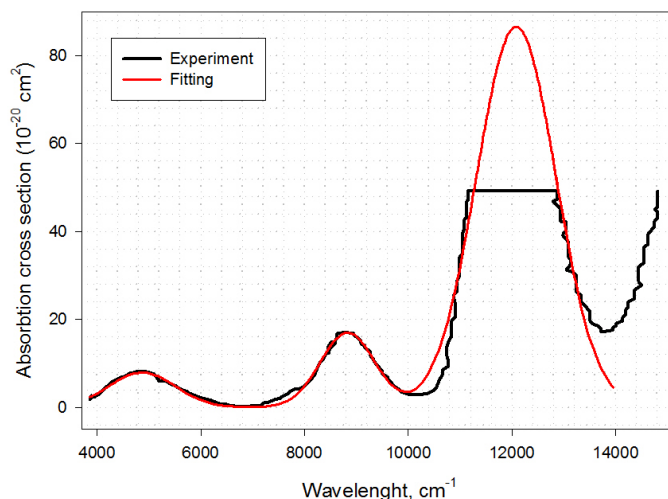


**Figure 63.** Absorption spectra of  $\text{Ni}^{2+}$  in ZnSe from 4000 to 14000  $\text{cm}^{-1}$  taken from reference [14] in  $\text{cm}^{-1}$  (black line) and its mathematical fit (red line).

### 3.19.3 Experimental spectra of $\text{Fe}^{2+}$ in ZnSe.

In [19], a source material involved in the creation of  $\text{Fe}^{2+}:\text{ZnSe}$  was 99.9% FeSe. In this reference, data are presented for two samples of  $\text{Fe}^{2+}:\text{ZnSe}$  having Fe concentrations of  $3 \times 10^{17}$  and  $4 \times 10^{19} \text{ cm}^{-3}$ . The concentrations of iron were calculated by using absorption data at  $3.15 \text{ }\mu\text{m}$  and  $14^\circ\text{K}$  along with the corresponding absorption cross section of  $\sigma = 1.5 \times 10^{-18} \text{ cm}^2$  [2]. For our present analysis, we chose to digitize experimental data for the sample having the greater concentration of iron since it demonstrated a somewhat richer behavior relative to the other sample. Reference [19] also contained spectra of the shorter wavelength region which indicated that the incorporation of Fe in ZnSe does not produce any significant shift of the absorption edge in the visible region relative to the absorption edge of pure bulk ZnSe which occurs around  $440 \text{ nm}$ . The absorption spectrum of the sample with the smaller concentration of iron showed a small “bump” near  $540 \text{ nm}$  at low temperature of an allegedly unknown nature. And, finally, in both samples, there were absorption band peaks around  $1.5 \text{ }\mu\text{m}$  in the temperature region from  $5$  to  $300^\circ\text{K}$ . The authors attributed this to either Fe or Ni, deducing that the samples were contaminated with Ni from the PL data which showed a  $2.6 \text{ }\mu\text{m}$  ( $3850 \text{ cm}^{-1}$ ) band that the authors assigned to the internal transition  ${}^3\text{T}_2(\text{F}) \rightarrow {}^3\text{T}_1(\text{F})$  and a  $3 \text{ }\mu\text{m}$  ( $3340 \text{ cm}^{-1}$ ) band that was assigned to the transition  ${}^3\text{E}_2(\text{D}) \rightarrow {}^2\text{T}_2(\text{D})$  of  $\text{Ni}^{2+}$  in ZnSe.

We also have digitized the absorption and luminescence spectra presented in reference [2] (see Figure 64). The luminescence spectral region in this work is much shorter than that presented in [19] with the peak being located at about  $3.75 \text{ }\mu\text{m}$  ( $2660 \text{ cm}^{-1}$ ). One of the advantages of this

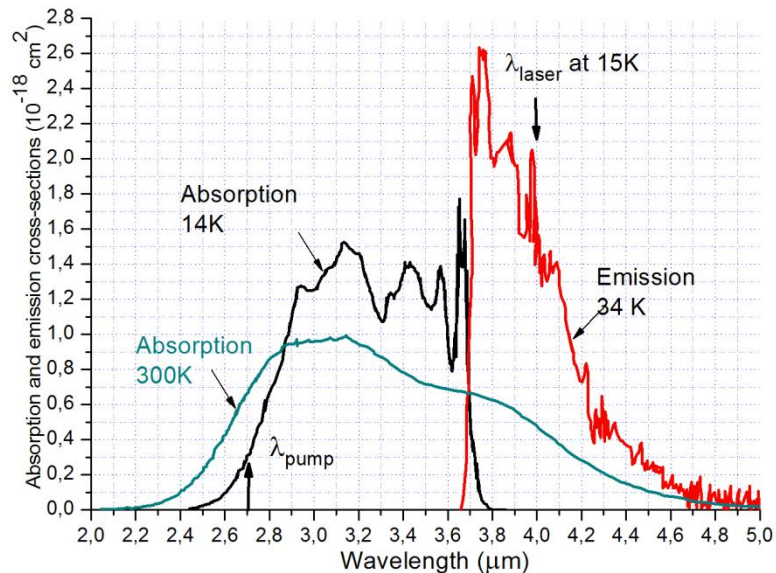


**Figure 64. Absorption and luminescence spectra of  $\text{Fe}^{2+}$  in ZnSe taken from [2].**

work is that there are absorption spectra at room temperature as well as at  $14^\circ\text{K}$  presented in absolute values rather than arbitrary ones, which allows us to compare the area under the spectral curves.

Shown in Figure 65 are the absorption spectra of  $\text{Fe}^{2+}$  in ZnSe over the 2600 to 4000  $\text{cm}^{-1}$  spectral range taken from the following references [1, 2, and 19]. The locations of the maxima of the peaks for the data from reference [1] are shown.

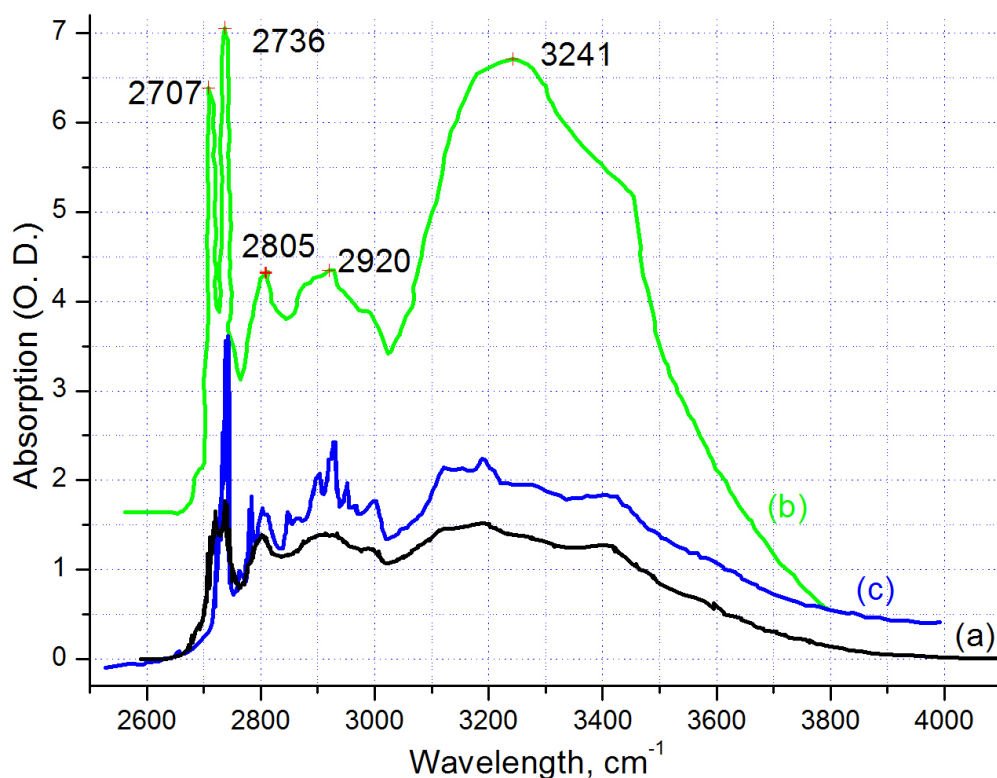


**Figure 65.** Absorption spectra of  $\text{Fe}^{2+}$  in ZnSe over the 2600 to 4000  $\text{cm}^{-1}$  spectral range: (a) ref. [2], (b) – ref. [1], (c) – ref. [19].

We have fit the absorption spectra from reference [2] by the sum of Gaussian functions, and obtained the following expression for the mathematically generated spectral curve:

$$\text{Fit(a,[2])} = 1.3\text{Exp}(-0.5*[(x-2728)/17]^2) + 0.58\text{Exp}(-0.5*[(x-2796)/18]^2) + \quad (66)$$

$$1.26\text{Exp}(-0.5*[(x-2900)/101]^2) + 0.70*\text{Exp}(-0.5*[(x-3145)/77]^2) + 1.24\text{Exp}(-0.5*[(x-3350)/202]^2).$$

The fit along with the experimental data are shown in Figure 66.

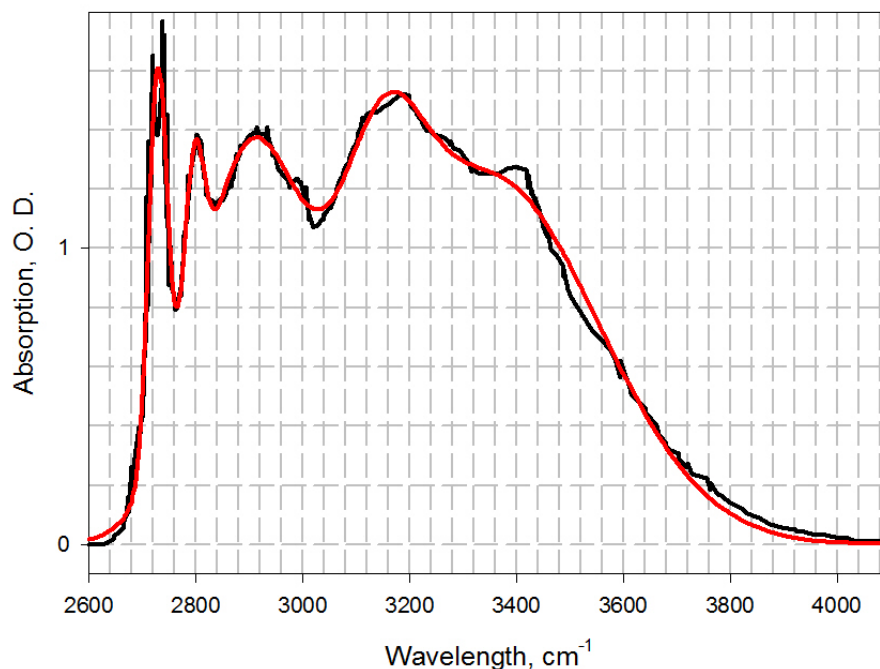


**Figure 66. Absorption spectra of  $\text{Fe}^{2+}$  in ZnSe over the 2600 to 4100  $\text{cm}^{-1}$  spectral range: experiment from ref. [2] – black line and its fit – red line.**

Finally, the location of the peaks of the emission spectra of  $\text{Fe}^{2+}:\text{ZnSe}$  are shown for the data from references [2, 19] in Figure 67.

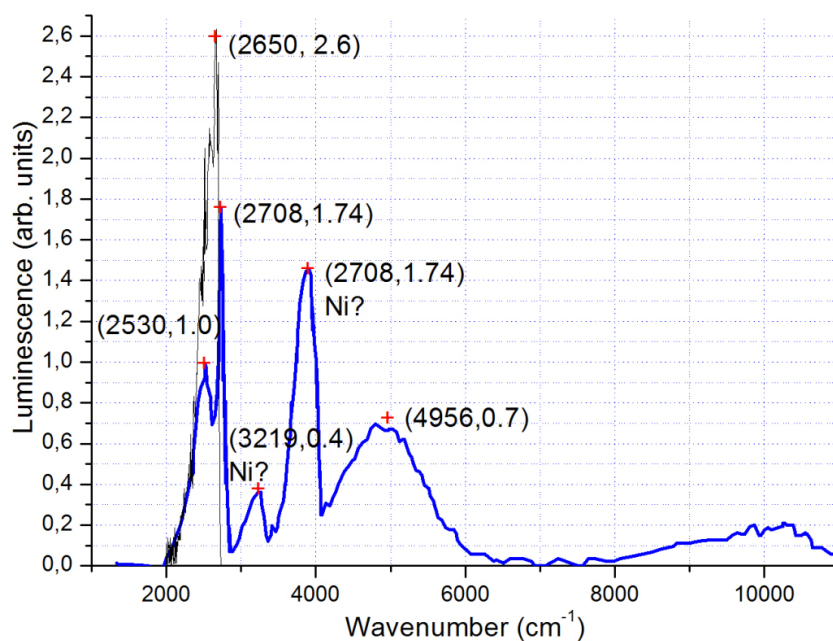


**Figure 67. Luminescence spectra of  $\text{Fe}^{2+}$  in ZnSe, blue line – ref. [19], black line – ref. [2].  
Spectroscopic characterization of TM doped samples**

## 4.0 SPECTROSCOPIC CHARACTERIZATION OF TM DOPED SAMPLES

### 4.1 Concentration and temperature quenching of mid-IR photoluminescence in Fe:ZnSe and Fe:ZnS crystals

In this project, we also focused on concentration and temperature quenching of mid-IR luminescence in Fe:ZnS and Fe:ZnSe crystals. Parameters associated with these processes are very important for the application of these materials in lasers.

Iron doped ZnSe and ZnS crystals were prepared using the thermo-diffusion method [1, 20]. The thickness of the metallic layer and the diffusion procedure were optimized to provide a uniform distribution of iron in the samples studied. Iron doped ZnS and ZnS samples having an Fe concentration of  $0.1\text{--}112 \times 10^{18} \text{ cm}^{-3}$  were prepared for spectroscopic experiments. The concentration of Fe ions in the samples was estimated using a value for the absorption cross-section of  $\sigma_{\text{ab}} = 0.65 \times 10^{18} \text{ cm}^{-2}$  at  $2.698 \text{ }\mu\text{m}$ .

An actively Q-switched Er:Cr:YSGG laser operating at  $2.78 \text{ }\mu\text{m}$  with a 80 ns pulse duration was utilized for optical excitation of the studied samples. The Fe:ZnSe and Fe:ZnS samples were placed in a closed-cycle refrigerator system (Janis Research Co., Inc., Model CCS-450) for temperature dependent spectroscopic measurements over the 14-300°K temperature range. The photoluminescence spectra were measured using an Acton Research ARC-300i spectrometer. The kinetics of luminescence for the given samples were measured with an InSb detector (Teledyne Judson J10D-M204-R250) equipped with a Perry amplifier which provides a 10 ns (10/90%) rise time and DC to 50 MHz response.

Room temperature absorption and luminescence spectra on the  ${}^5E \leftrightarrow {}^5T_2$  transition of  $\text{Fe}^{2+}$  ions in ZnSe and ZnS crystals are shown in Figure 68. A dip in the photo-luminescence curves at 4300 nm is caused by absorption of atmospheric  $\text{CO}_2$  in the experimental setup.

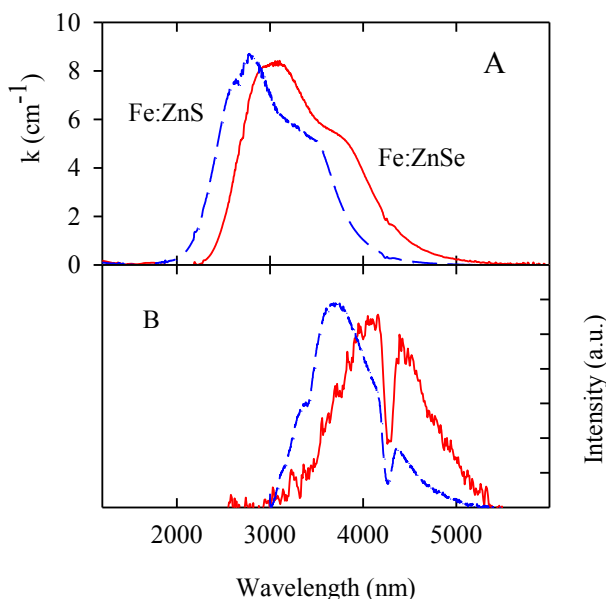


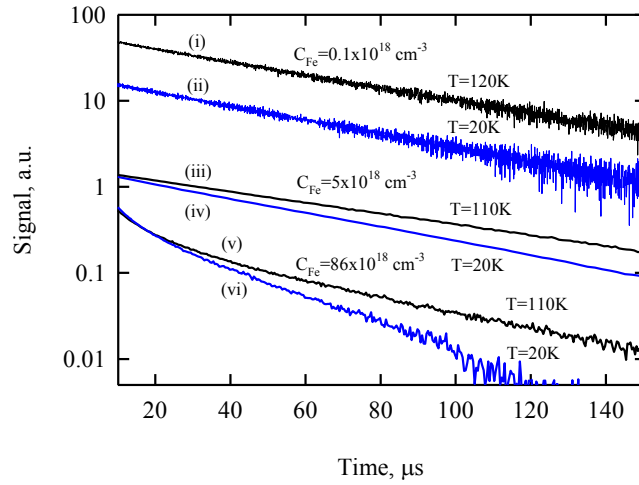
**Figure 68. Room temperature absorption (A) and emission (B) spectra of Fe:ZnSe (solid line) and Fe:ZnS (dashed line) crystals.**

#### 4.1.1 Fe:ZnSe crystal.

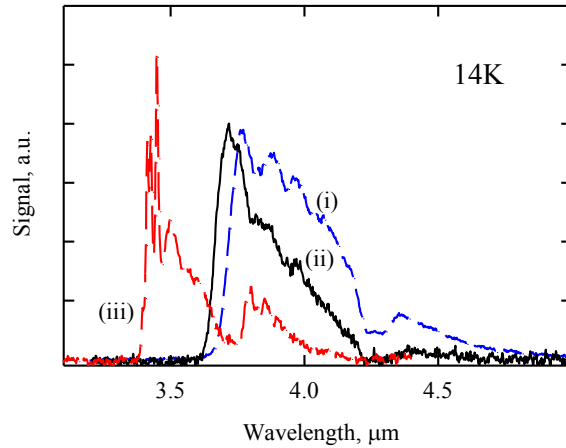
Luminescence lifetime studies over the 15-300°K temperature range were reported in [21] and [3]. In [21], Fe:ZnSe single-crystal samples with an iron concentration from  $3.4$  to  $6.5 \times 10^{19} \text{ cm}^{-3}$  were reported. In the temperature range from 12 to 120°K, the lifetime unexpectedly increased initially from 33 to 105  $\mu\text{s}$  and then decreased as the temperature was further increased due to temperature induced non-radiative processes. Similarly, an unusual growth of the luminescence lifetime with an increase in temperature from 14 to 120°K was also reported in [3] where it was attributed to the thermal population of iron sub-levels having a smaller oscillator strength. In the current study, we also observed an increase in the luminescence lifetime with an increase in temperature from 14 to 120°K in an Fe:ZnSe sample having an iron concentration of  $C_{\text{Fe}} = 5 \times 10^{18} \text{ cm}^{-3}$ . The luminescence kinetics of this sample at 20 and 77°K are shown in the Figure 69 (curve iii and iv). As one can see from the Figure 69, the luminescence decay reveals a single exponential behavior with luminescence lifetimes of  $\tau = 54 \mu\text{s}$  at  $T = 20^\circ\text{K}$  and  $\tau = 68 \mu\text{s}$  at  $T = 77^\circ\text{K}$ . However, in the crystal having the smallest iron concentration  $C_{\text{Fe}} = 0.1 \times 10^{18} \text{ cm}^{-3}$ , the kinetics of the luminescence at low temperature were similar in the 14-110°K temperature range with the luminescence lifetime being  $\sim \tau = 57 \pm 4 \mu\text{s}$  (see Figure 69, curves i and ii). Therefore, we consider the unusual increase in the fluorescence lifetime between 14 and 110°K reported in the papers [3, 21] to be attributed to iron-iron interactions as well as luminescence re-absorption at low temperatures. The highly doped sample ( $C_{\text{Fe}} = 86 \times 10^{18} \text{ cm}^{-3}$ ) also revealed an asymptotic decay at  $T = 110^\circ\text{K}$  (curve v) which is longer than that at  $T = 20^\circ\text{K}$  (curve vi), but the low temperature kinetics of this sample were essentially non-exponentials. One of the reasons behind the non-exponential behavior could be related to multi-center formation in highly doped crystals.

Figure 70 shows the low temperature ( $T = 14^\circ\text{K}$ ) luminescence spectra of samples having iron concentrations of  $C_{\text{Fe}} = 5 \times 10^{18} \text{ cm}^{-3}$  and  $C_{\text{Fe}} = 86 \times 10^{18} \text{ cm}^{-3}$ . The spectrum of the sample with an iron concentration of  $C_{\text{Fe}} = 5 \times 10^{18} \text{ cm}^{-3}$  is similar to what has been published before. The luminescence spectrum of the highly doped sample ( $C_{\text{Fe}} = 86 \times 10^{18} \text{ cm}^{-3}$ ) is slightly red-shifted and demonstrates profound peaks on the long wavelength slope of the luminescence spectra. The nature of multi-center formation in a highly doped Fe:ZnSe crystal is a subject for separate studies.





**Figure 69. Luminescence kinetics of Fe:ZnSe samples having iron concentrations of:  $C = 0.1 \times 10^{18} \text{ cm}^{-3}$  (i,ii);  $C = 5 \times 10^{18} \text{ cm}^{-3}$  (iii,iv); and  $C = 86 \times 10^{18} \text{ cm}^{-3}$  (v,vi); at  $T = 20^\circ\text{K}$  (ii;iv;vi),  $T = 110^\circ\text{K}$  (iii,v); and  $T = 120^\circ\text{K}$  (i).**



**Figure 70. Luminescence spectra of Fe:ZnSe samples at  $T = 14^\circ\text{K}$  having the following iron concentrations: (i)  $C_{\text{Fe}} = 112 \times 10^{18} \text{ cm}^{-3}$  and (ii)  $C_{\text{Fe}} = 5 \times 10^{18} \text{ cm}^{-3}$ ; and an Fe:ZnS sample at  $T = 14^\circ\text{K}$  having an iron concentration of: (iii)  $C_{\text{Fe}} = 5 \times 10^{18} \text{ cm}^{-3}$ .**

The temperature dependence of the luminescence lifetime of a low doped ( $C_{\text{Fe}} = 0.1 \times 10^{18} \text{ cm}^{-3}$ ) Fe:ZnSe sample is shown in the Figure 71. As it was mentioned earlier, in the 14-120°K temperature range, the luminescence lifetime was unchanged initially at  $\tau = 57 \pm 4 \text{ μs}$  and then decreased with temperature due to thermally activated non-radiative decay. We utilized two models of the non-radiative process to fit the experimental data. Initially, we used a model describing thermally activated radiationless processes based on the intersection of the configuration coordinates of the upper and low levels. These processes are typical for non-radiative relaxation in optical centers having a strong electron-phonon coupling.



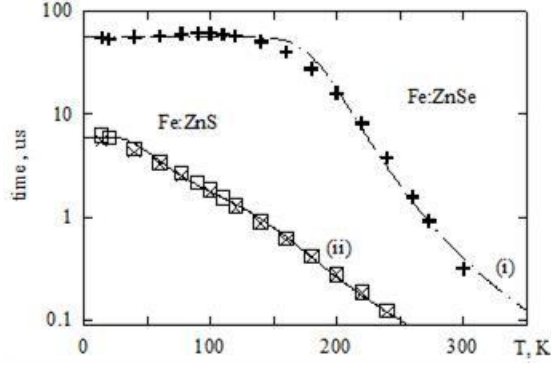


**Figure 71. Luminescence lifetime versus temperature for Fe:ZnSe (+ -  $C_{Fe} = 0.1 \times 10^{18} \text{ cm}^{-3}$ ) and for Fe:ZnS crystals ( $\times$ - $C_{Fe} = 3 \times 10^{18} \text{ cm}^{-3}$ ,  $\square$ -  $C_{Fe} = 73 \times 10^{18} \text{ cm}^{-3}$ ); curves describing the fits are described in the text.**

This approach leads to a temperature dependence of the upper level lifetime given by the following equations (see [22]):

$$\tau^{-1}(T) = \tau_{rad}^{-1} + W_{nr} \quad (67)$$

$$W_{nr} = W_0 \exp(-\Delta E_a/kT), \quad (68)$$

where  $\tau_{rad}$  is the radiative lifetime,  $W_{nr}$  is the nonradiative relaxation rate,  $\Delta E_a$  is the energy gap (activation energy) between the intersection of the adiabatic potentials of the ground and excited states and the minimum of the adiabatic potential of the excited state,  $W_0$  is the relaxation parameter; and  $k_B$  is the Boltzmann constant, Figure 72. The best fit was obtained using the parameters  $\Delta E_a = 2500 \text{ cm}^{-1}$  and  $1/W_a = 0.1 \text{ ns}$  (see Figure 69, curve i).

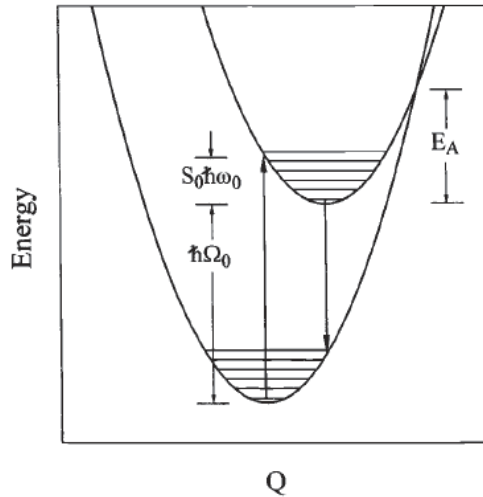


**Figure 72. Configuration coordinate diagram for linear coupling [23]**

Temperature measurements of the low doped sample allow us to estimate the radiation lifetime of the  ${}^5E \leftrightarrow {}^5T_2$  transition to be  $\tau_{rad} = 57 \pm 4 \mu\text{s}$ . Using this value for the radiative lifetime, the emission cross sections at RT were calculated from the *Füchtbauer-Ladenburg* equation [1] with the emission cross section equaling  $\sigma_{em} = 1.2 \times 10^{-18} \text{ cm}^2$  at  $4.3 \mu\text{m}$ .

Figure 73 shows the room temperature luminescence kinetics of a Fe:ZnSe crystal with an iron concentration varying from  $0.1 \times 10^{18}$  to  $112 \times 10^{18} \text{ cm}^{-3}$ . Luminescence kinetics of the low doped Fe:ZnSe crystal (curve 1) was single exponential at RT with a luminescence lifetime  $\tau_{RT} = 382 \text{ ns}$ . This decay time is significantly smaller than the radiative lifetime ( $\tau_{rad}$ ) of the  ${}^5E \leftrightarrow {}^5T_2$  transition and is determined by thermally induced non-radiative processes. The photoluminescence kinetics of the highly doped crystal reveals a non-exponential decay (curve 4). However, asymptotic decay curves were exponential with a small decrease of the lifetime to  $309 \text{ ns}$  for a sample having an iron concentration of  $C_{Fe} = 112 \times 10^{18} \text{ cm}^{-3}$  in comparison with  $382 \text{ ns}$  for a sample having an iron concentration of  $C_{Fe} = 0.1 \times 10^{18} \text{ cm}^{-3}$ . Decreases in the asymptotic decay rate of highly doped crystals relative to lower doped crystals as well as the non-exponential decay feature are characteristics of the energy migration process. The decay rate ( $W_q$ ) induced by concentration quenching can be calculated from the difference of the asymptotic decay rates of the low and highly doped samples. But, even for the highly doped sample,  $W_q = 0.6 \mu\text{s}^{-1}$  is still smaller than that associated with temperature quenching of the luminescence. Simulation of the photoluminescence decay of highly doped samples requires a numerical simulation of the energy migration processes to include those associated with the multi-center complexes of the iron in the highly doped crystal (a good approximation can be obtained through the double exponential decay fit of the photoluminescence decay curve with time constants of  $\tau_1 = 309 \text{ ns}$  and  $\tau_2 = 138 \text{ ns}$ ). However, it is more convenient for laser applications such as passive Q-switching, mode-locking and gain-switching to estimate the average relaxation time  $\langle \tau_{av} \rangle$  as  $\int I(t)/I_{max} dt$ .

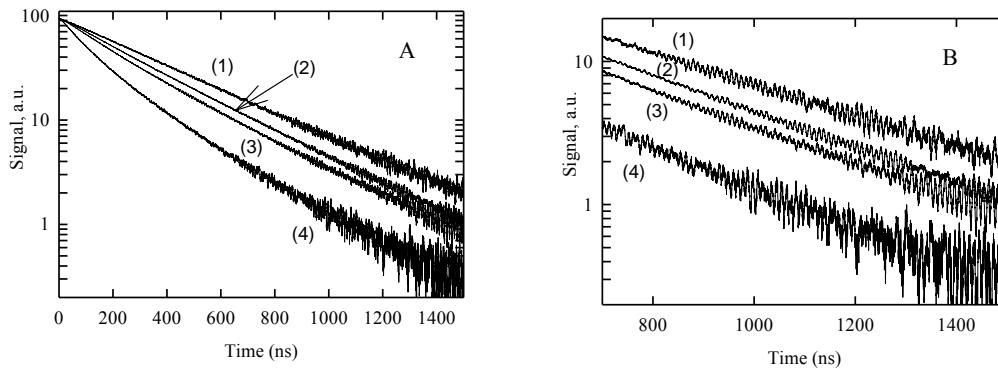


**Figure 73. A) Luminescence kinetics of Fe:ZnSe samples with different iron concentrations: (1)-  $C_{Fe} = 0.1 \times 10^{18} \text{ cm}^{-3}$ ; (2)- $C_{Fe} = 14 \times 10^{18} \text{ cm}^{-3}$ ; (3)- $C_{Fe} = 45 \times 10^{18} \text{ cm}^{-3}$ ; and (4)-  $C_{Fe} = 112 \times 10^{18} \text{ cm}^{-3}$ , B) same luminescence kinetics with an expanded time scale.**

Figure 74 shows the dependence of the average relaxation rate on the iron concentration. As shown in Figure 74, the decay rate decreases from  $382 \text{ ns}$  for a lower concentration Fe:ZnSe

sample to 186 ns for a Fe:ZnSe sample having an iron concentration of  $C_{Fe} = 112 \times 10^{18} \text{ cm}^{-3}$ . The concentration dependence of the average decay time can be fit with the empirical equation;

$$\langle \tau_{av} \rangle = \frac{\tau_r}{1 + N_{Fe}/N_0} \quad (69)$$

where,  $N_{Fe}$  is the concentration of  $Fe^{2+}$  ions, and  $N_0$  is the critical concentration parameter where the decay time is reduced by a factor of 2. A least squares fit of the experimental lifetime data is also shown in Figure 72 (dashed curve). The best-fit value for  $N_0$  was determined to be  $106 \times 10^{18} \text{ cm}^{-3}$ . Since these decay times are longer than the typical pulse duration for Q-switched lasers ( $\sim 100 \text{ ns}$ ), lasers based on Fe:ZnSe crystals are able to lase at room temperature under short-pulse gain-switched excitation.

We observed a decrease in the average relaxation time for highly doped samples due to concentration quenching at low temperature. The average relaxation time of the lower doped sample ( $C_{Fe} = 0.1 \times 10^{18} \text{ cm}^{-3}$ ) was equal to the decay time obtained from a single exponential fit ( $57 \mu\text{s}$ ) at  $T = 20^\circ\text{K}$ . The sample having an iron concentration of  $C_{Fe} = 5 \times 10^{18} \text{ cm}^{-3}$  had a slightly faster relaxation time of  $50 \mu\text{s}$ . A further increase in the concentration results in a shortening of the relaxation time to  $7 \mu\text{s}$  when the iron concentration reaches  $86 \times 10^{18} \text{ cm}^{-3}$ .

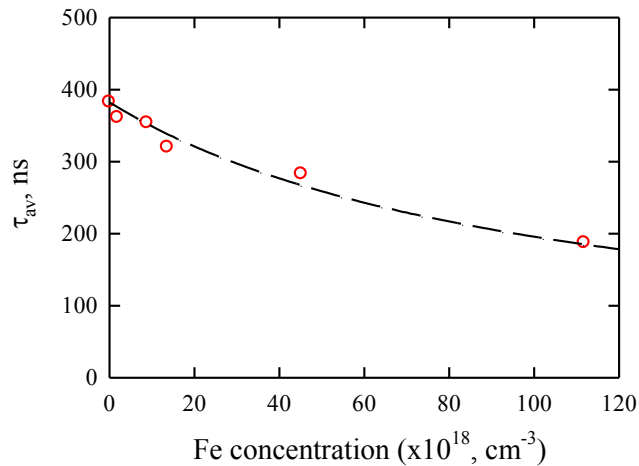


**Figure 74. Average relaxation time of the  $^5T_2 \rightarrow ^5E$  transition versus iron concentration in Fe:ZnSe samples measured at room temperature (dashed line shows least square fit using eq. 70).**

#### 4.1.2 Fe:ZnS crystal

The Zinc Selenide crystal is one of the most frequently used active element hosts for  $Cr^{2+}$  and  $Fe^{2+}$  based mid-IR lasers. However, the iron doped Zinc Sulfide crystal is also very attractive for mid-IR laser applications. First of all, due to the larger crystal field splitting of the  $^5D$  ground state in the Fe:ZnS crystal, the absorption and emission spectra are shifted to a shorter wavelength in comparison with the ZnSe host (see Figures 68 and 70). As a result, the room temperature luminescence spectra of Fe:ZnS cover the 3-5  $\mu\text{m}$  spectral range. Due to the strong

absorption bands of hydrocarbons and other organic molecules in this spectral range, Fe:ZnS lasers are very promising for sensing applications. In this work, we report the temperature dependence of the mid-IR photoluminescence of Fe:ZnS samples having iron concentrations which vary over the  $(3-73) \times 10^{18} \text{ cm}^{-3}$  range. Figure 75A shows the luminescence kinetics of Fe:ZnS crystals measured at  $T = 220^\circ\text{K}$  for three different iron concentrations. The luminescence kinetics were found to be single exponential with a luminescence lifetime of  $\tau = 182 \text{ ns}$  for all of the studied samples. Due to limitations in the duration of the pump source (80 ns), the lifetime of the Fe:ZnS samples could not be obtained above  $250^\circ\text{K}$ . Decreasing the sample temperature to  $14^\circ\text{K}$  was found to result in a monotonous increasing of the luminescence lifetime to  $\tau = 6.2$  and  $5.5 \mu\text{s}$  for iron concentrations of  $C_{\text{Fe}} = 3 \times 10^{18} \text{ cm}^{-3}$  and  $C_{\text{Fe}} = 73 \times 10^{18} \text{ cm}^{-3}$ , respectively (see Figure 71). These results are close to what was reported earlier in [23] where a lifetime of  $5.5 \mu\text{s}$  and a quantum yield of 10% were measured for this transitions at low temperature. Using these results, we can estimate a radiative lifetime of  $\tau_{\text{rad}} = 62-55 \mu\text{s}$  for the Fe:ZnS crystal.

The temperature dependence of the luminescence cannot be fit by a thermally activated radiationless relaxation model based on a single configuration coordinate. A more accurate model should consider the additional physical processes along with a more accurate energy

structure. Since it is known that the *Jahn-Teller* interaction results in additional splitting of the upper and ground state  $^5D$  levels, a more accurate model should therefore include several radiationless processes having different relaxation parameters. The solid curve in the Figure 71 shows a fit using the two relaxation processes described by equation (68) with the following parameters:  $\Delta E_{a1} = 818 \text{ cm}^{-1}$ ;  $I/W_{01} = 1 \text{ ns}$ ; and  $\Delta E_{a2} = 126 \text{ cm}^{-1}$ ; and  $I/W_{02} = 420 \text{ ns}$ . At high temperature, a relaxation model should also include multi-phonon processes [22]. A more accurate model will require additional experimental study of the luminescence lifetime at high temperatures under short pulse excitation. Extrapolation of the luminescence lifetime to room temperature allow us to estimate the lifetime as  $\tau = 50 \text{ ns}$ .

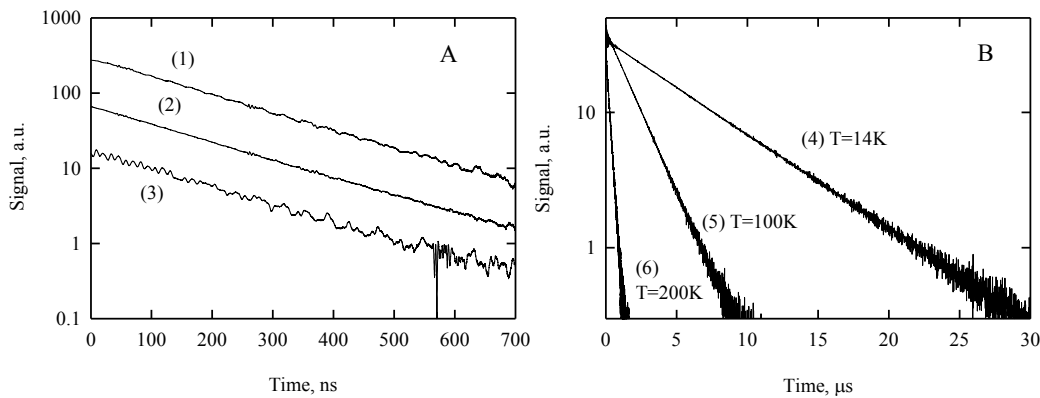


**Figure 75. A) Luminescence kinetics of Fe:ZnS samples having different iron concentrations: (1)-  $C_{\text{Fe}} = 3 \times 10^{18} \text{ cm}^{-3}$ ; (2)-  $C_{\text{Fe}} = 15 \times 10^{18} \text{ cm}^{-3}$ ; (3)-  $C_{\text{Fe}} = 73 \times 10^{18} \text{ cm}^{-3}$  at  $T = 220^\circ\text{K}$ ; B) Luminescence kinetics of Fe:ZnS having an iron concentration of  $C_{\text{Fe}} = 3 \times 10^{18} \text{ cm}^{-3}$  at different temperatures (4-6)**

## 4.2 Cobalt doped samples

The cobalt concentration gradient was measured using an Er-fiber laser operating at 1.56  $\mu\text{m}$ . To measure the concentration gradient with high spatial resolution, a 1 mm output beam from an Er-fiber laser was focused by lens with a focal length of  $F = 5 \text{ cm}$  to a beam with a waist diameter of  $d_{1/e^2} = 1.23 \cdot \lambda \cdot F / D_{1/e^2} = 97 \mu\text{m}$  and a confocal depth of  $Z_R = \pi d_{1/e^2}^2 / \lambda = 1.9 \text{ cm}$ . To calculate the concentration gradient, we measured the variation of the transmission of the laser beam through a 1 cm long crystal as shown in Figure 76. The cobalt concentration gradient of a Co:ZnSe sample annealed for 7 days is also shown in the figure and is found to be negligible.

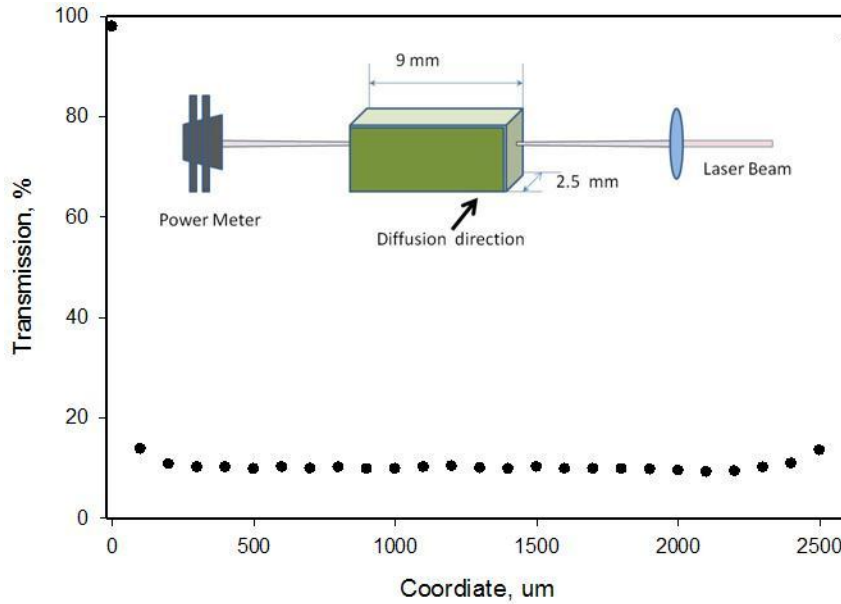


**Figure 76. Experimental setup and results for the measurement of the cobalt concentration gradient in a Co:ZnSe crystal.**

Most of previous studies of cobalt doped ZnSe and ZnS crystals were focused on the  $^4A_2(F) \rightarrow ^4T_1(F)$  transition near 1.6  $\mu\text{m}$ . This particular transition of  $\text{Co}^{2+}$  has attracted significant interest due to possible utilization in saturable absorber crystals in  $\text{Er}^{3+}$  lasers operating at 1.5  $\mu\text{m}$ . Several authors have reported the absorption cross-section of this transition (see Table 6 for details). Based on reported values for the absorption cross-sections of  $\text{Co}^{2+}$ , we used absorption cross-sections of  $7.5 \times 10^{-19} \text{ cm}^2$  at 1625 nm and  $7.8 \times 10^{-19} \text{ cm}^2$  at 1500 nm for the ground state absorption  $^4A_2(F) \rightarrow ^4T_1(F)$  transition in ZnSe and ZnS crystals, respectively.

The  $^4A_2(F) \rightarrow ^4T_2(P)$  near infrared transition has an absorption cross-section approximately one order of magnitude bigger (e.g.  $64 \times 10^{-19} \text{ cm}^2$  at 768 nm for Co:ZnSe). It should be noted that because the absorption cross-sections for the entire 700-800 nm band are higher than the absorption cross-section at 1625 nm, this band could be used for optical excitation. However, because of the high absorption coefficient associated with this band, only a side-pumping configuration is feasible.

Another absorption band of practical importance is the  ${}^4A_2(F) \rightarrow {}^4T_2(F)$  mid-IR transition around 3000 nm. First, this transition could be used to enable passive Q-switching of Er-lasers operating at 3  $\mu\text{m}$ . Second, this transition is promising for the development of tunable lasers operating over the 3-4  $\mu\text{m}$  range. Third, the  ${}^4T_2(F)$  upper level is the donor level in Co-Fe co-doped gain elements. However, this transition is symmetry forbidden for the electric-dipole interaction and the maximum value of the absorption cross section was estimated to be  $5.2 \times 10^{-20} \text{ cm}^{-2}$  at 2956 nm in Co:ZnSe samples. This is more than order of magnitude less than the value of the absorption cross-section values for the  ${}^4A_2(F) \rightarrow {}^4T_1(F)$  transition near 1.6  $\mu\text{m}$ . The experimentally measured absorption cross-sections for  $\text{Co}^{2+}$  ions in ZnSe and ZnS crystals on the A)  ${}^4A_2(F) \rightarrow {}^4T_2(P)$ ; B)  ${}^4A_2(F) \rightarrow {}^4T_1(F)$ ; and C)  ${}^4A_2(F) \rightarrow {}^4T_2(F)$  transitions are depicted in Figures 77 and 78, respectively and are summarized in Table 15.

**Table 15. Summary of the spectroscopic characteristics of Co:ZnSe and Co:ZnS.**

Crystal	Transition	Wavelength, [nm]	Ground state absorption cross section	maximum cross-section	Ref
Co:ZnSe	${}^4A_2(F) \rightarrow {}^4T_1(P)$	768		$64 \times 10^{-19} \text{ cm}^{-2}$	[cs]
	${}^4A_2(F) \rightarrow {}^4T_1(F)$	1535	$6.5 \times 10^{-19} \text{ cm}^{-2}$		[24]
	${}^4A_2(F) \rightarrow {}^4T_1(F)$	1598	$5.3 \times 10^{-19} \text{ cm}^{-2}$		[25]
	${}^4A_2(F) \rightarrow {}^4T_1(F)$	1534	$11.5\text{-}9.7 \times 10^{-19} \text{ cm}^{-2}$		[26]
	${}^4A_2(F) \rightarrow {}^4T_1(F)$	1540	$7.6 \times 10^{-19} \text{ cm}^{-2}$		[27]
	${}^4A_2(F) \rightarrow {}^4T_1(F)$	1573	$5.7 \times 10^{-19} \text{ cm}^{-2}$		[28]
	${}^4A_2(F) \rightarrow {}^4T_1(F)$	1625		$7.5 \times 10^{-19} \text{ cm}^{-2}$	[1]
	${}^4A_2(F) \rightarrow {}^4T_2(F)$	2956		$7.8 \times 10^{-20} \text{ cm}^{-2}$	[1]
	${}^4A_2(F) \rightarrow {}^4T_2(F)$	2790		$11 \times 10^{-20} \text{ cm}^{-2}$	[19]
	${}^4A_2(F) \rightarrow {}^4T_2(F)$	2956		$5.2 \times 10^{-20} \text{ cm}^{-2}$	[cs]
Co:ZnS	${}^4A_2(F) \rightarrow {}^4T_1(P)$	726		$56 \times 10^{-19} \text{ cm}^{-2}$	[cs]
	${}^4A_2(F) \rightarrow {}^4T_1(F)$	1534	$10\text{-}8 \times 10^{-19} \text{ cm}^{-2}$		[26]
	${}^4A_2(F) \rightarrow {}^4T_1(F)$	1540	$7.7 \times 10^{-19} \text{ cm}^{-2}$		[27]
	${}^4A_2(F) \rightarrow {}^4T_1(F)$			$7.5 \times 10^{-19} \text{ cm}^{-2}$	[1]
	${}^4A_2(F) \rightarrow {}^4T_2(F)$			$7.8 \times 10^{-20} \text{ cm}^{-2}$	[1]
	${}^4A_2(F) \rightarrow {}^4T_2(F)$	2790	$5.6 \times 10^{-20} \text{ cm}^{-2}$		[19]
	${}^4A_2(F) \rightarrow {}^4T_2(F)$	2760		$4.8 \times 10^{-20} \text{ cm}^{-2}$	[cs]

cs – current study

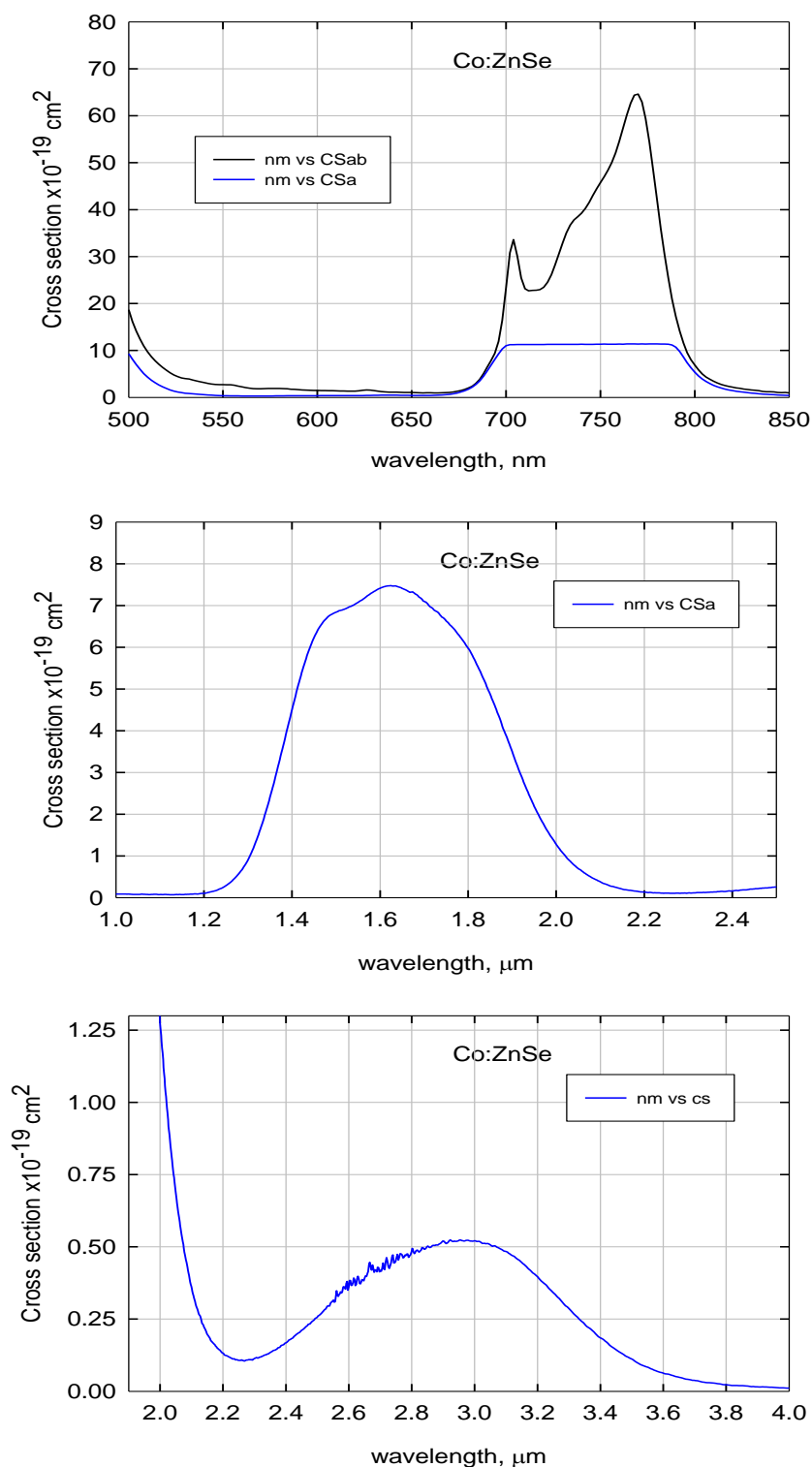


**Figure 77.** The absorption cross-sections of  $\text{Co}^{2+}$  ions in ZnSe crystals on the  $^4\text{A}_2(\text{F}) \rightarrow ^4\text{T}_2(\text{P})$  (Upper part);  $^4\text{A}_2(\text{F}) \rightarrow ^4\text{T}_1(\text{F})$  (Middle part part); and  $^4\text{A}_2(\text{F}) \rightarrow ^4\text{T}_2(\text{F})$  transitions (Bottom part). The black curve refers to a cobalt concentration of  $N_{\text{Co}} = 1 \times 10^{18} \text{ cm}^{-3}$  and the blue curves refers to a cobalt concentration of  $N_{\text{Co}} = 2.2 \times 10^{19} \text{ cm}^{-3}$ .

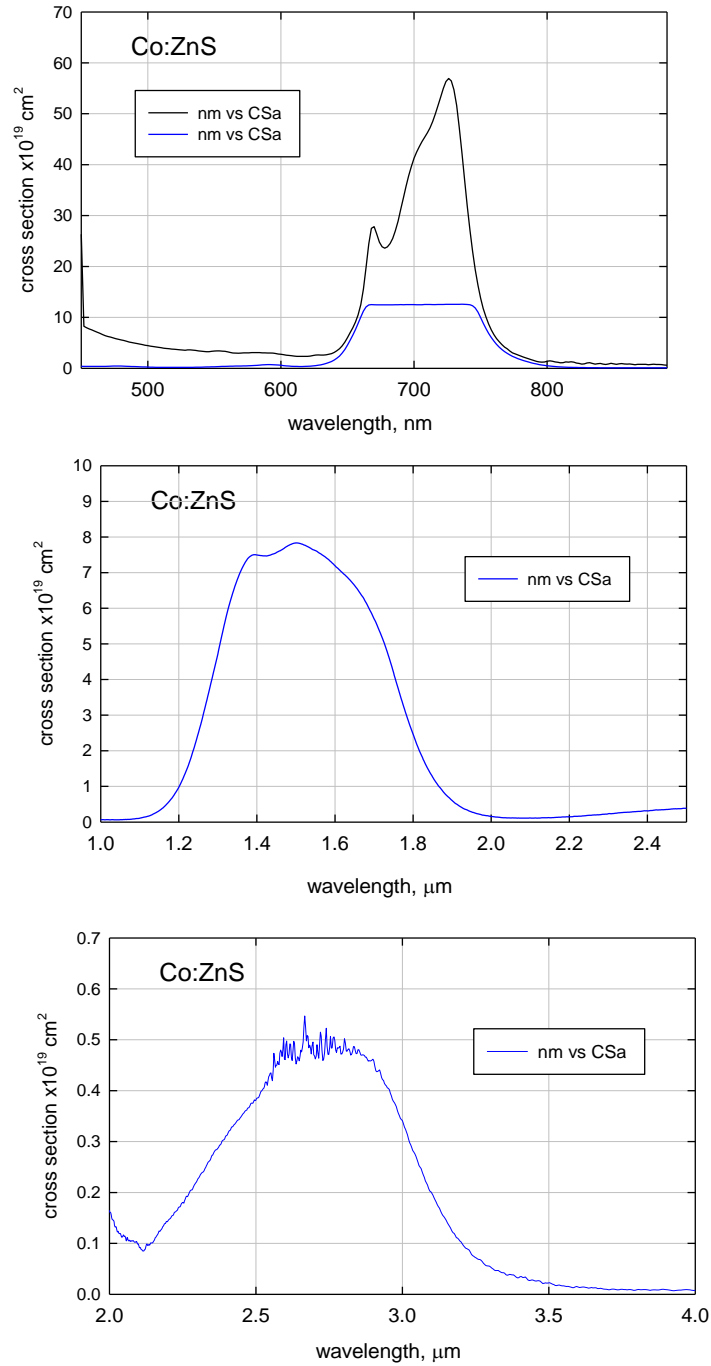


**Figure 78.** The absorption cross-sections of  $\text{Co}^{2+}$  ions in ZnS crystals on the  ${}^4\text{A}_2(\text{F}) \rightarrow {}^4\text{T}_2(\text{P})$  (*Upper part*);  ${}^4\text{A}_2(\text{F}) \rightarrow {}^4\text{T}_1(\text{F})$  (*Middle part*); and  ${}^4\text{A}_2(\text{F}) \rightarrow {}^4\text{T}_2(\text{F})$  transitions (*Bottom part*). The black curve refers to a cobalt concentration of  $N_{\text{Co}} = 0.5 \times 10^{18} \text{ cm}^{-3}$  and the blue curve refers to a cobalt concentration of  $N_{\text{Co}} = 1.9 \times 10^{19} \text{ cm}^{-3}$ .



### 4.3 Spectroscopic characterization of $\text{Co}^{2+}$ and $\text{Fe}^{2+}$ co-doped samples

The lack of convenient pump sources is a major reason hampering the broad application of mid-IR lasers based on Fe:ZnSe crystals. One possible way of exciting iron is via energy transfer from other conveniently pumped TM ions. The donor-acceptor energy transfer rate, according to Forster-Dexter theory, is proportional to the overlap integral of the donor emission and acceptor absorption bands. Therefore, among TM ions, chromium and cobalt are very attractive candidates for this application. Both ions have strong absorption bands in the 1.4-2.0  $\mu\text{m}$  spectral range where a number of convenient pump sources are available. Figure 79 shows possible energy transfer channels among  $\text{Fe}^{2+}$ ,  $\text{Co}^{2+}$  and  $\text{Cr}^{2+}$  ions in II-VI crystals. As one can see, the spectral overlap between cobalt and iron is practically ideal. To study energy transfer characteristics, several cobalt and Co-Fe co-doped samples were fabricated.

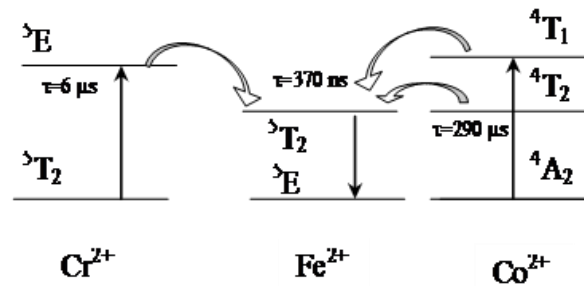


**Figure 79. Diagram of the energy transfer mechanisms in the iron, chromium and cobalt co-doped II-VI materials.**

Initially, a one week thermal diffusion from a cobalt thin-film was carried out to fabricate cobalt doped ZnSe and ZnS. After that in order to form Co:Fe:ZnSe and Co:Fe:ZnS, iron thin films were deposited on both crystals. To provide a homogenous distribution of ions over the crystal thickness, the crystals were annealed for an additional 2 weeks. The absorption spectra of the Co:Fe:ZnSe samples are depicted in Figure 80. As one can see from Figure 80, the  $\text{Co}^{2+}$  ion concentration is the same ( $N_{\text{Co}} = 4.5 \times 10^{18} \text{ cm}^{-3}$ ) in all samples, while the concentration of  $\text{Fe}^{2+}$  changes from 0 to  $N_{\text{Fe}} = 18 \times 10^{18} \text{ cm}^{-3}$ .

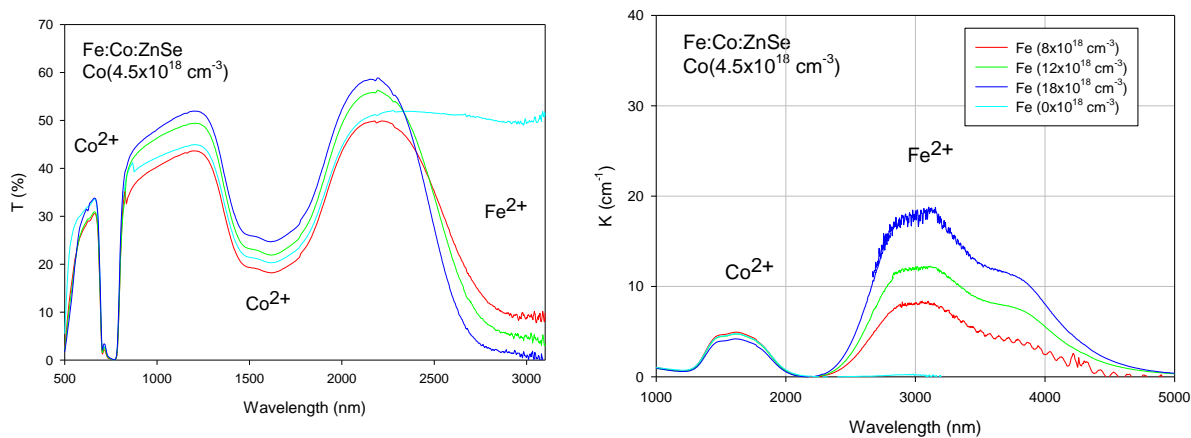


**Figure 80. Transmission and absorption spectra of Co:Fe:ZnSe crystals**

Similar results were obtained for the Co:Fe:ZnS sample shown in the Figure 81. As one can see from Figure 81, the absorption bands of the  $\text{Fe}^{2+}$  and  $\text{Co}^{2+}$  ions are shifted slightly to shorter wavelengths in comparison with the ZnSe host due to a stronger crystal field splitting. From absorption measurements, the cobalt concentration was estimated to be  $N_{\text{Co}} \approx 8 \times 10^{18} \text{ cm}^{-3}$  while the iron concentration varied from 0 to  $10 \times 10^{18} \text{ cm}^{-3}$ .

The luminescence and PL kinetics were measured using an injection seeded, single frequency Q-switched Nd:YAG laser (GCR-230-10, Spectra Physics) with a maximum output energy of 1.5 J at 1.064  $\mu\text{m}$ , a linewidth of 0.003  $\text{cm}^{-1}$ , a 10 ns pulse duration and a repetition rate of 10 Hz. After passing through an optical isolator, the 1.064  $\mu\text{m}$  Nd:YAG radiation was focused by a 25 cm focal length lens into a 50 cm long Raman cell filled with  $\text{D}_2$  at a pressure of 600 psi. In a backscattering geometry, the output energy of the first Stokes line at 1.56  $\mu\text{m}$  exceeded 300 mJ with a pulse duration of 7 ns at the FWHM.

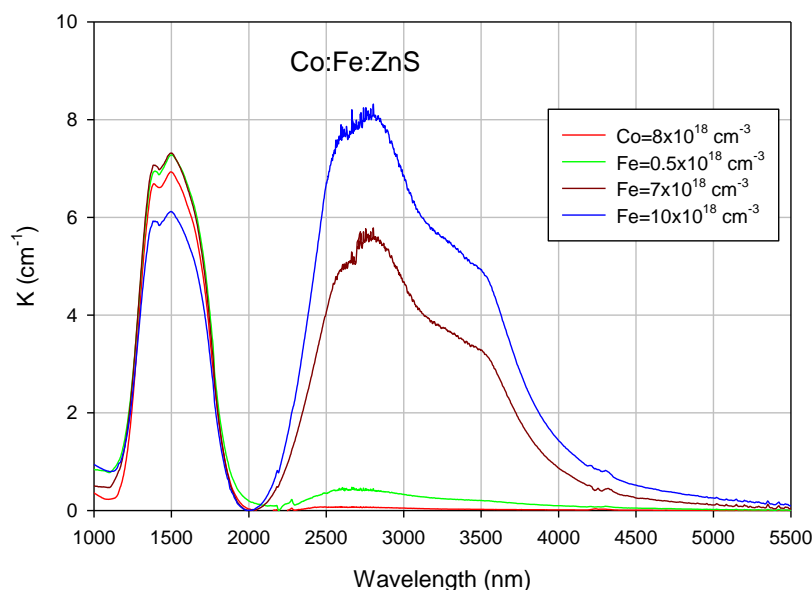


**Figure 81. Absorption spectra of Co:Fe:ZnS crystals**

Room temperature time-resolved photoluminescence spectra of the Co:Fe:ZnSe crystal (with cobalt and iron concentrations equal to  $C_{\text{Co}} = 6 \times 10^{18} \text{ cm}^{-3}$  and  $C_{\text{Fe}} = 8.5 \times 10^{18} \text{ cm}^{-3}$ , respectively) are shown in Figure 82. Pulsed radiation at  $1.56 \mu\text{m}$  with a 15 ns pulse duration was used for direct excitation of  $\text{Co}^{2+}$  on the  ${}^4\text{A}_2 \rightarrow {}^4\text{T}_1$  transition. It is interesting to note that when the time delay is a minimum, the luminescence spectrum (curve i) consists of both  $\text{Co}^{2+}$  and  $\text{Fe}^{2+}$  bands with approximately equal intensities. A dip in the luminescence spectrum at  $4.3 \mu\text{m}$  results from atmospheric  $\text{CO}_2$  absorption in the experimental setup. After a  $40 \mu\text{s}$  time-delay, the luminescence spectrum reveals only a  $\text{Co}^{2+}$  photoluminescence signal (ii). This indicates that the most efficient energy transfer occurs only directly after excitation and that the energy transfer rate from the  ${}^4\text{T}_2$  cobalt level is not significant for the TM concentrations studied.

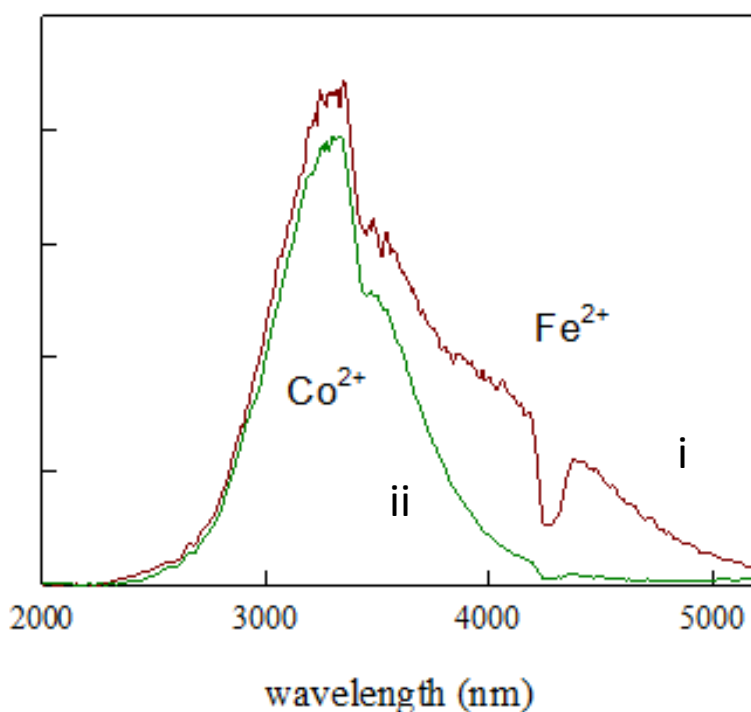


**Figure 82. Time resolved spectra of Co:Fe:ZnSe under  $1.56 \mu\text{m}$  excitation with a  $4 \mu\text{s}$  gate-width and  $0 \mu\text{s}$  (i) and  $40 \mu\text{s}$  time delays (ii).**

#### 4.4 Energy transfer in Co:Fe:ZnS/ZnSe crystals under excitation at $720 \text{ nm}$

Energy transfer studies were associated with measurements of the mid-IR spectra and the kinetics of photoluminescence in several cobalt iron co-doped samples. The absorption spectra of Co:Fe:ZnS (J4510) are shown in the Figure 83.

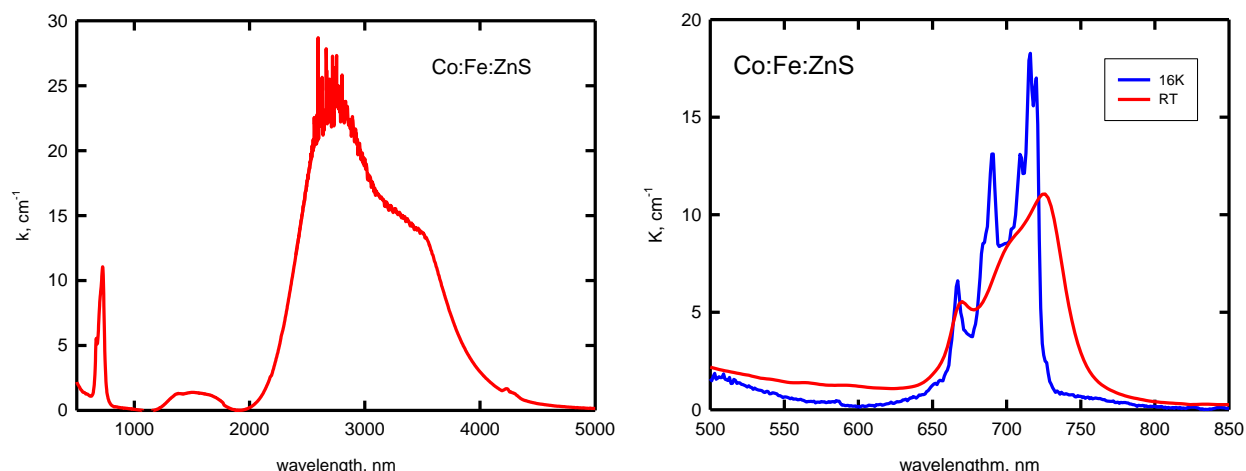


**Figure 83. Absorption spectrum of the Co:Fe:ZnS sample measured at RT (red curve) and  $T = 16^\circ\text{K}$  (blue curve).**

Average concentrations of cobalt and iron ( $N_{Co} = 1.8 \times 10^{18} \text{ cm}^{-3}$ ;  $N_{Fe} = 3.5 \times 10^{19} \text{ cm}^{-3}$ ) in the samples were estimated using the absorption cross-sections for cobalt ( $\sigma_{ab} = 7.8 \times 10^{-19} \text{ cm}^2$ ) and iron ( $\sigma_{ab} = 6.7 \times 10^{-19} \text{ cm}^2$ ) at 1.5 and 2.7  $\mu\text{m}$ , respectively. The right hand side of Figure 83 shows room and low temperature absorption on the  $^4A_2(F) \rightarrow ^4T_2(P)$  transition. As one can see from Figure 83, the long-wavelength edge of the absorption band is shifted to 726 nm at low temperature. Therefore the excitation wavelength should be between 670 and 725 nm for effective excitation of mid-IR emission.

To demonstrate the feasibility of exciting the mid-IR photoluminescence on the  $^4A_2(F) \rightarrow ^4T_2(P)$  transition, we studied mid-IR photoluminescence kinetics and spectra using radiation from an Alexandrite laser for optical pumping of the  $\text{Co}^{2+}$  ions. We used a slightly focused Alexandrite laser (PAL 101, Light Age, Inc.) beam having a maximum pulse energy of 80 mJ at 720-780 nm, a beam diameter of 2 mm (FWHM), a pulse duration of 70 ns, and a repetition rate of 13 Hz.

The kinetics of the mid-IR photoluminescence signal of a Co:Fe:ZnS crystal under excitation by an Alexandrite laser were measured at  $T = 20$  and  $77^\circ\text{K}$  and are shown in Figure 84. Curve i in the upper part of the figure shows the low temperature kinetics of non-selective mid-IR luminescence of the Co:Fe:ZnS (J4510) sample. As one can see from the Figure 84, the kinetics shown in curve i features a non-exponential behavior. On a long time scale ( $t > 300 \mu\text{s}$ ), the kinetics asymptotically approach the decay curve of  $\text{Co}^{2+}$  kinetics in a Co:ZnS (J4110,  $N_{Co} = 1.8 \times 10^{18} \text{ cm}^{-3}$ ) crystal with a decay time of  $\tau = 1.2 \text{ ms}$  (curve ii). Strong non-exponential decay results from the photoluminescence and excitation migration over  $\text{Fe}^{2+}$  ions in the initial stage of the kinetics. For comparison, the insert in Figure 84 shows the kinetics (curve iii) of a Fe:ZnS (J3310,  $N_{Fe} = 5 \times 10^{18} \text{ cm}^{-3}$ ) crystal under direct optical excitation at 2.8  $\mu\text{m}$  with a decay time of  $\tau = 6 \mu\text{s}$  at  $T = 20^\circ\text{K}$ . The rise time of the kinetics is shorter than 1  $\mu\text{s}$  and is limited by the temporal resolution of the registration system. Similar mid-IR photoluminescence dynamics were measured at  $T = 77^\circ\text{K}$  and are shown in the bottom part of Figure 84.

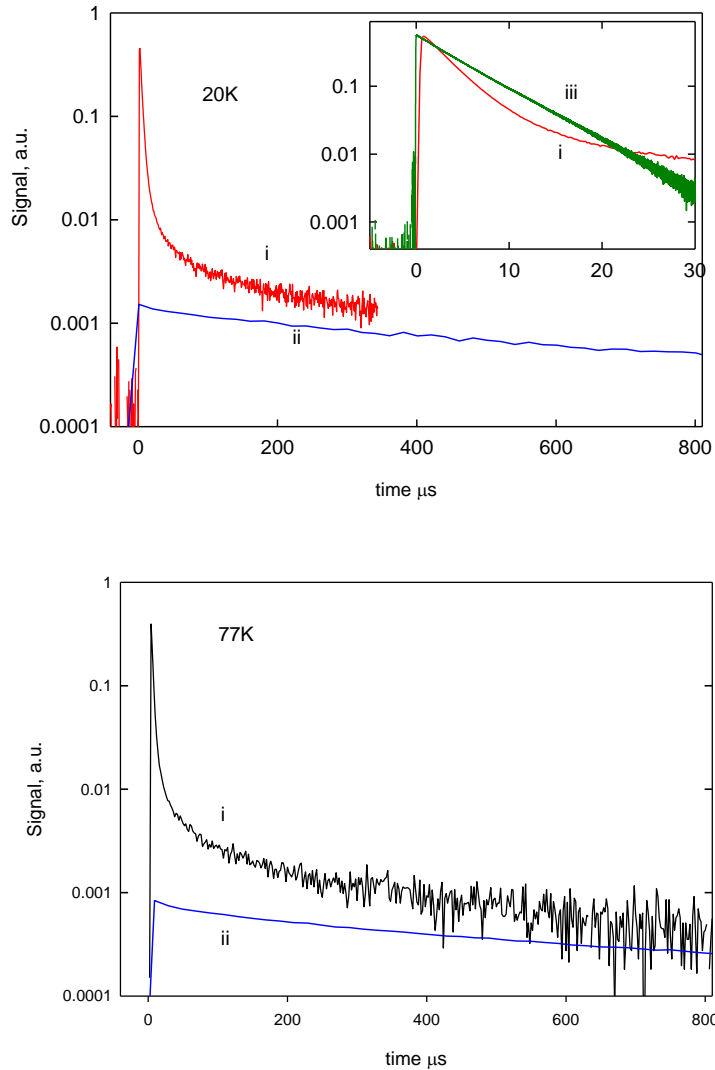


**Figure 84. Kinetics of the mid-IR photoluminescence of Co:Fe:ZnS (curve i); Co:ZnS (curve ii); and Fe:ZnS (curve iii) at  $T = 20^\circ\text{K}$  and  $77^\circ\text{K}$  under  $\text{Co}^{2+}$  excitation (curve i and ii) at  $720\text{ nm}$ ; and under  $\text{Fe}^{2+}$  excitation (curve iii) at  $2.8\text{ }\mu\text{m}$ .**

The kinetics of the mid-infrared photoluminescence signal of Co:Fe:ZnSe under excitation by an Alexandrite laser were measured at  $T = 14^\circ\text{K}$  and are shown in Figure 85. For comparison purposes, the kinetics of the  $\text{Fe}^{2+}$  mid-infrared photoluminescence signal in ZnSe having a decay time of  $\sim 50\text{ }\mu\text{s}$  is also presented in the Figure 85. As one can see from Figure 85, the decay curve of the Co:Fe:ZnSe ( $N_{\text{Co}} = 6.4 \times 10^{18}\text{ cm}^{-3}$ ;  $N_{\text{Fe}} = 1.9 \times 10^{19}\text{ cm}^{-3}$ ) sample kinetics reveals a strong non-exponential behavior which asymptotically approaches the decay curve of the Fe:ZnSe (J1209,  $N_{\text{Co}} = 9 \times 10^{18}\text{ cm}^{-3}$ ) crystal kinetics. It is interesting to note that in contrast to the kinetics of the Co:Fe:ZnS crystal, the kinetics of the Co:Fe:ZnSe crystal does not have the long decay time typical of a single-impurity center. The kinetics of the Co:ZnSe (J2110,  $N_{\text{Co}} = 6 \times 10^{18}\text{ cm}^{-3}$ ) crystal under the same excitation conditions is also shown in Figure 85. The much longer decay time of the Co:ZnSe curve means that the photoluminescence of “practically all of the

Co<sup>2+</sup> ions” is quenched by the energy transfer to Fe<sup>2+</sup> ions in spite of the fact that the iron concentration in the Co:Fe:ZnS crystal was higher. One possible way of explaining this is that the formation of the Fe-Co pair center could be more efficient in the ZnSe crystal than in the ZnS crystal. One example of a system with strong impurity pairing is the Nd:CaF<sub>2</sub> system where Nd-Nd pair formation is the predominant process even at small impurity concentrations.

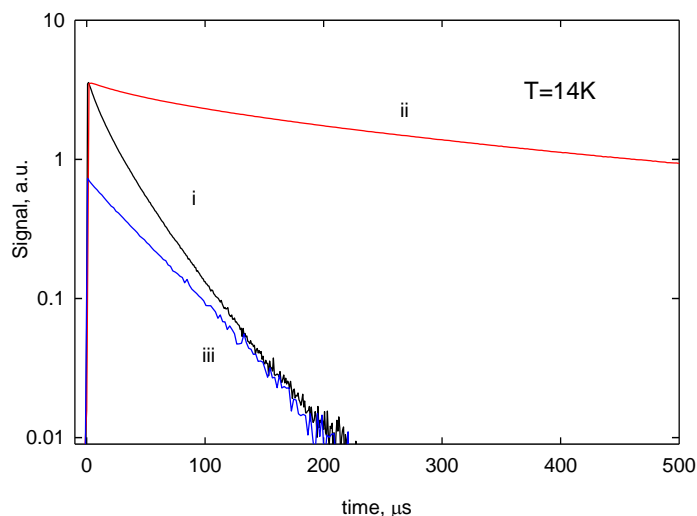


**Figure 85. Kinetics of mid infrared photoluminescence of Co:Fe:ZnSe (curve i); Co:ZnSe (curve ii); and Fe:ZnS (curve iii) under 760 nm excitation of Co<sup>2+</sup> (curves i and ii); and 2.8 μm excitation of Fe<sup>2+</sup> excitation (curve iii) at T = 14°K.**

Shown in Figure 86 are the photoluminescence spectra of Co:Fe:ZnSe and Co:ZnSe samples under direct excitation of the <sup>4</sup>A<sub>2</sub>(F)→<sup>4</sup>T<sub>1</sub>(P) (~750 nm) transition in cobalt at 14°K. In these experiments, we used a crystal with Fe and Co concentrations of 19×10<sup>18</sup> cm<sup>-3</sup> and 6.4×10<sup>18</sup> cm<sup>-3</sup>, respectively. In the Co:ZnSe crystal, one can see a well-structured photoluminescence spectrum corresponding to the <sup>4</sup>T<sub>2</sub>(F) →<sup>4</sup>A<sub>2</sub>(F) symmetry-forbidden transition of cobalt with a luminescence maximum at 3040 nm. In the Co:Fe:ZnSe co-doped samples, the photoluminescence shown in Figure 86B was significantly shifted to longer wavelengths and coincides with earlier reported results of the low temperature photoluminescence spectrum of Fe<sup>2+</sup> ions. A maximum in the photoluminescence signal of the iron-cobalt co-doped samples was found to occur at 3750 nm. Also, as one can see from Figure 86, the direct photoluminescence signal from cobalt was significantly quenched and was hardly detectable in comparison with the iron photoluminescence signal.

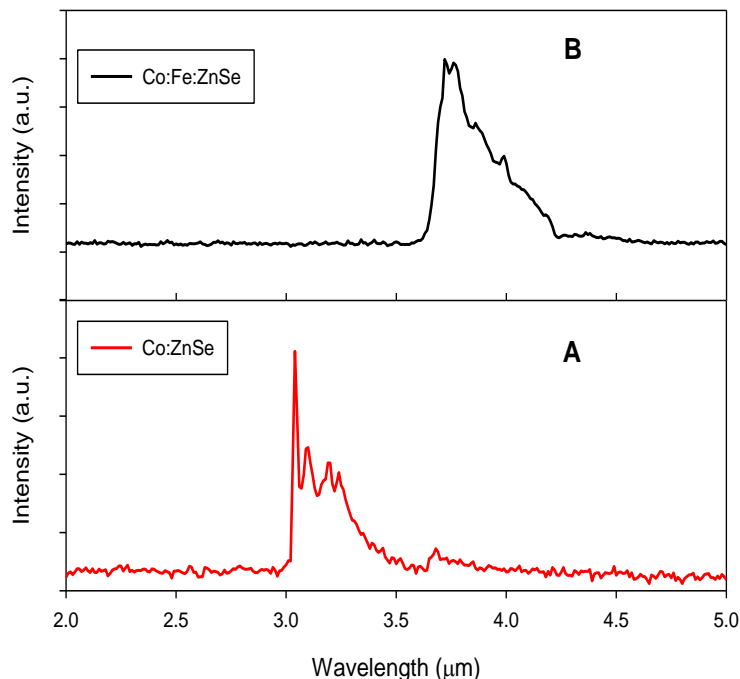


**Figure 86. Mid-infrared luminescence spectra of iron and cobalt co-doped ZnSe crystals at  $T = 14^{\circ}\text{K}$  under 760nm excitation.**

#### 4.5 Spectroscopic characterization of $\text{Co}^{2+}$ and $\text{Ni}^{2+}$ co-doped samples

The absorption spectrum of an unpolished Co:Ni:ZnSe sample (811-65) is shown in Figure 87 below. For comparison, the absorption spectrum of a Co:ZnSe crystal is also presented in Figure 87. Two additional bands at 870 and 1130 nm were observed due to the  ${}^3\text{T}_1(\text{F}) \rightarrow {}^3\text{T}_1(\text{P})$  and  ${}^3\text{T}_1(\text{F}) \rightarrow {}^3\text{A}_2(\text{F})$  transitions, respectively, of nickel in the nickel-cobalt co-doped crystal.

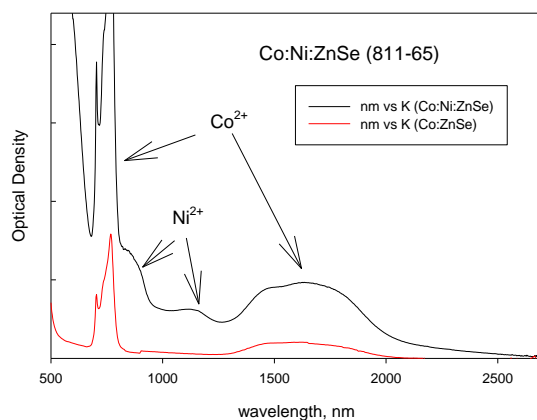


**Figure 87. Absorption spectra of the Co:Ni:ZnSe (black curve), and Co:ZnSe (red curve) crystals.**

The photoluminescence spectra of Ni:Co:ZnS and Ni:Co:ZnSe were measured at room temperature under excitation of a 1064 nm free running Nd:YAG laser. While the Ni:Co:ZnSe sample did not feature a mid-infrared luminescence, a characteristic Co luminescence was observed in the Ni:Co:ZnS sample (see Figure 88).

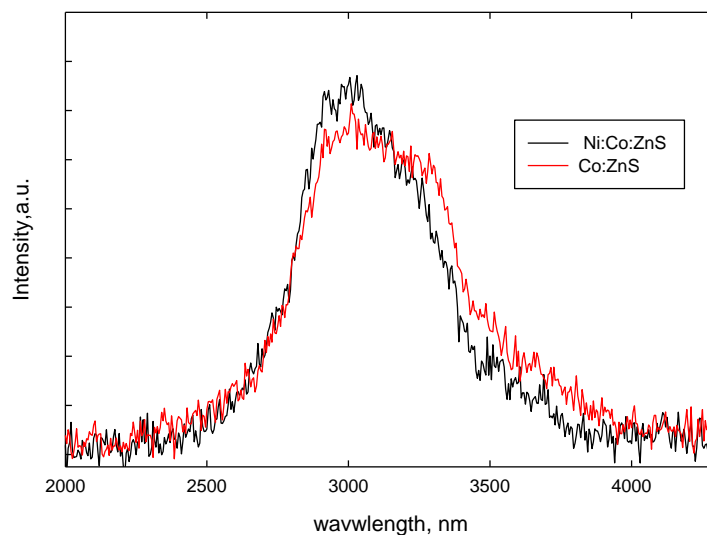


**Figure 88. RT photo-luminescence spectra of Ni:Co:ZnS (black curve) and Co:ZnS (red curve) samples.**

However, a similar PL band was also observed in a Co:ZnS sample under 1064 nm excitation. This luminescence is not believed to be due to energy transfer from Ni to Co, but rather to be due to a direct excitation into the short wavelength tail of the absorption band of  $\text{Co}^{2+}$ .



## 5.0 LASER CHARACTERIZATION OF TM DOPED SAMPLES

### 5.1. Lasing of Co:Fe:ZnSe and Co:Fe:ZnS crystals *via* effective Co→Fe energy transfer under 1.56 $\mu\text{m}$ wavelength excitation

The high gain associated with highly doped Co:Fe:ZnS crystals allowed us to test the lasing properties of these crystals by pumping at 1.56  $\mu\text{m}$  even in the absence of an external cavity. For this experiment, we used Co:Fe:ZnS/ZnSe crystals ( $10 \times 10 \times 1.2 \text{ mm}^3$ ) having cobalt and iron concentrations of  $0.5 \times 10^{18} \text{ cm}^{-3}$  and  $10 \times 10^{18} \text{ cm}^{-3}$ , respectively.

Pump radiation from a Q-switched Raman shifted YAG laser at 1.56  $\mu\text{m}$  was slightly focused into a spot having a  $\sim 3 \text{ mm}$  diameter. The crystal was placed in a Close-Cycle Refrigerator operating in the 14-300°K temperature range.

Figure 89 shows the luminescence spectra of several crystals measured at 14°K. The first plot involving Co:ZnS shows the typical  $\text{Co}^{2+}$  luminescence which has characteristic peaks around 2800 and 3100 nm upon excitation at 1.56  $\mu\text{m}$ . The third plot shows the luminescence spectrum of a Co:Fe:ZnS crystal having a low iron concentration of  $0.5 \times 10^{18} \text{ cm}^{-3}$  under the same excitation with 1.56  $\mu\text{m}$ . As one can see from this graph, in addition to the  $\text{Co}^{2+}$  luminescence, there is also a strong  $\text{Fe}^{2+}$  luminescence having characteristic peaks at 3440 nm, 3570 nm, and 3820 nm. For comparison purposes, the luminescence spectrum of an Fe:ZnS sample under direct excitation of the iron ions at 2.9  $\mu\text{m}$  was measured at 14°K and is depicted in the second graph. The fourth graph shows the luminescence spectrum of a Co:Fe:ZnS crystal under 1.56  $\mu\text{m}$  excitation having an iron concentration  $\times 50$  times greater. As one can see, there is no  $\text{Co}^{2+}$  luminescence in this crystal. The measured luminescence spectrum shows only  $\text{Fe}^{2+}$  bands that are slightly red-shifted in comparison with the spectrum of the low doped sample. This result proves that there is a fast energy transfer from  $\text{Co}^{2+}$  to  $\text{Fe}^{2+}$  ions in this crystal. We used this crystal for the following laser experiments.

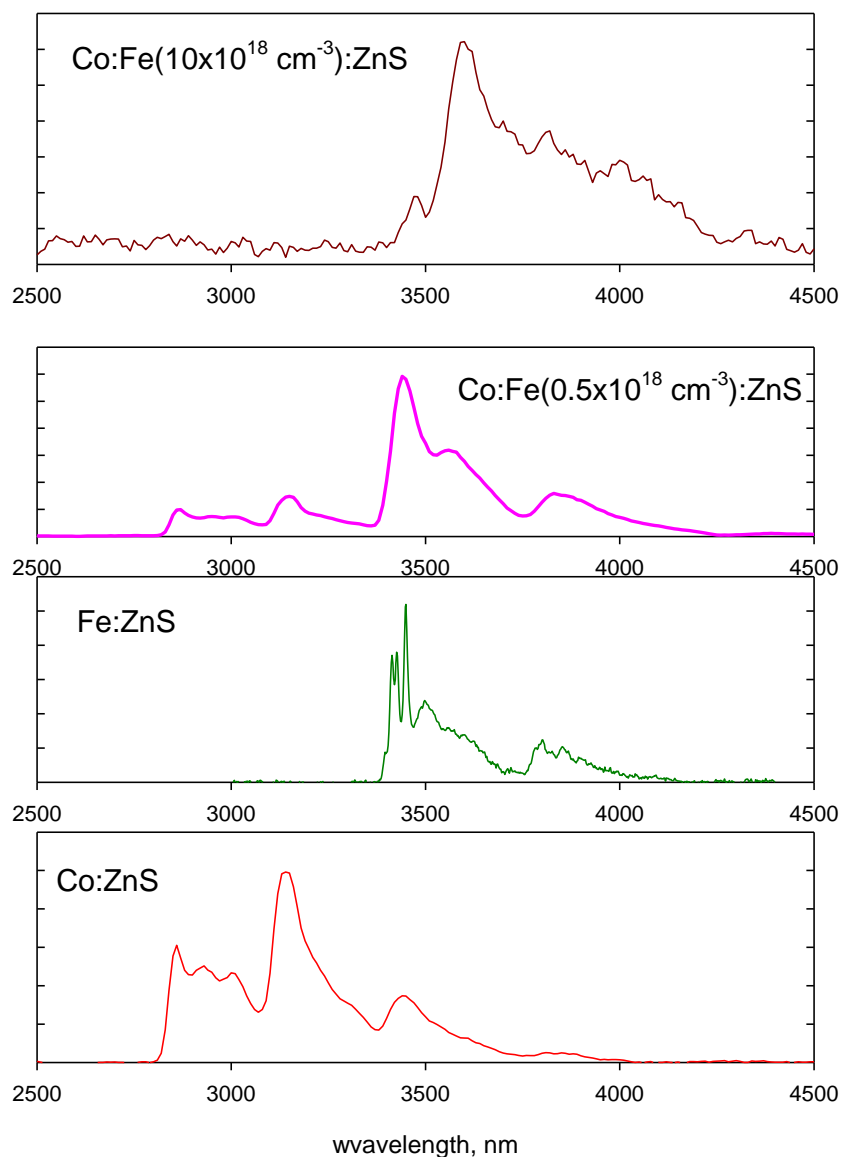


**Figure 89. Mid-infrared luminescence spectra of iron and cobalt doped crystals at  $T = 14^{\circ}\text{K}$ .**

Two basic experiments on the pump energy dependence of the luminescence kinetics and luminescence spectra were performed to demonstrate lasing of  $\text{Fe}^{2+}$  via effective energy transfer from the  $\text{Co}^{2+}$  ion. Positive feedback for the oscillation of Fe was enabled by the Fresnel reflections from the crystal facets which provided a reflectivity of 18% from each surface. The large Fresnel Number  $N_F = d^2/L\lambda \sim 10^4$  of the resonator provided for minimum diffraction losses in the cavity.

The results of the experiments are shown in the Figure 90. Figure 90A shows the photoluminescence spectra of a Co:Fe:ZnSe crystal for different pump energies. As one can see in Figure 90A, at low pump energy, the measured PL spectra were typical for the luminescence of iron. The profile of the photoluminescence spectrum also demonstrated a threshold behavior

that was dependent on the pump energy. A stimulated emission band around 3850 nm as shown in Figure 90 appeared when the threshold was exceeded.

The change of the luminescence profile above the laser threshold was accompanied by a shortening of the decay time of the luminescence kinetics as shown in the Figure 90B. When pumped at low energy, one can see a low temperature  $\text{Fe}^{2+}$  kinetic with a luminescence rise time of  $\tau \sim 1 \mu\text{s}$  followed by an exponential decay with a lifetime of  $\tau \sim 2.5 \mu\text{s}$ . Above the laser threshold, the kinetics demonstrate a typical laser spike with a  $\sim 200 \text{ ns}$  pulse duration followed by luminescence decay kinetics. The threshold dependence of the emission, a significant line narrowing, and the shortening of the lifetime are clear evidence of Co:Fe:ZnSe lasing via the Co $\rightarrow$ Fe energy transfer mechanism.

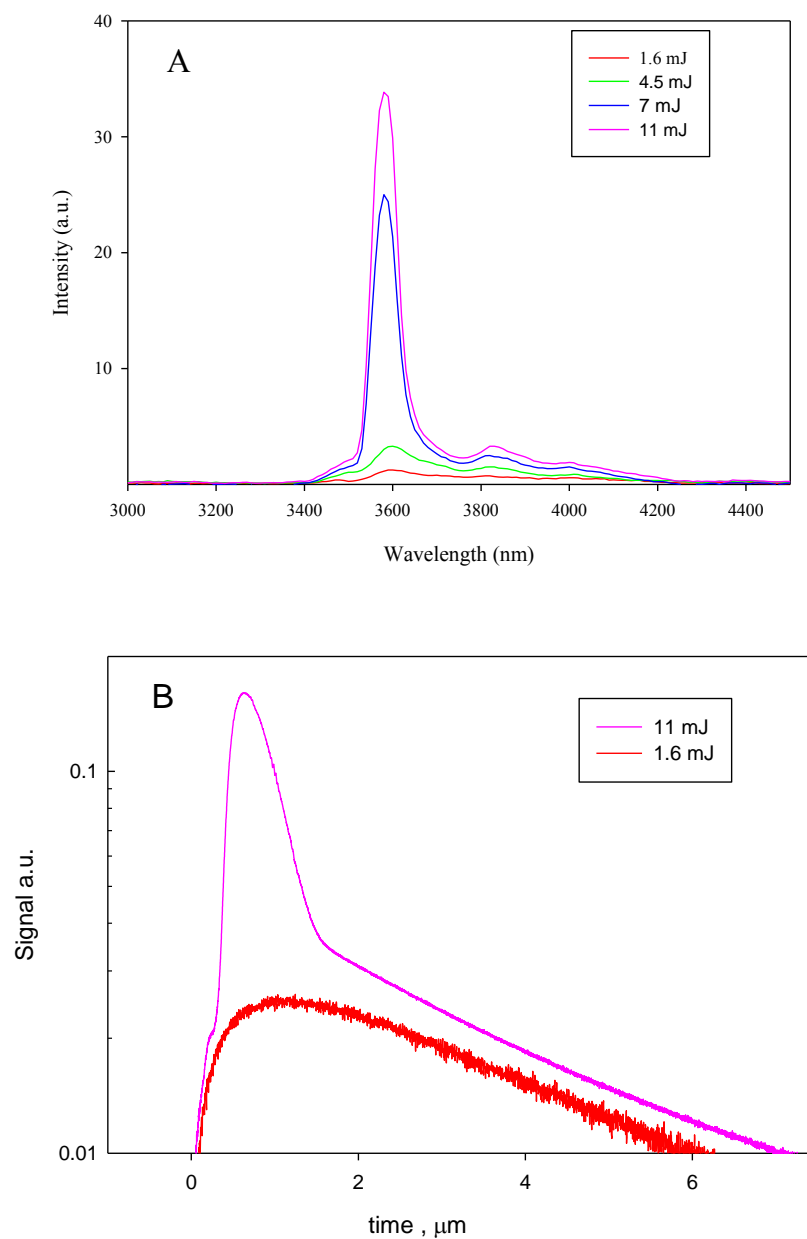


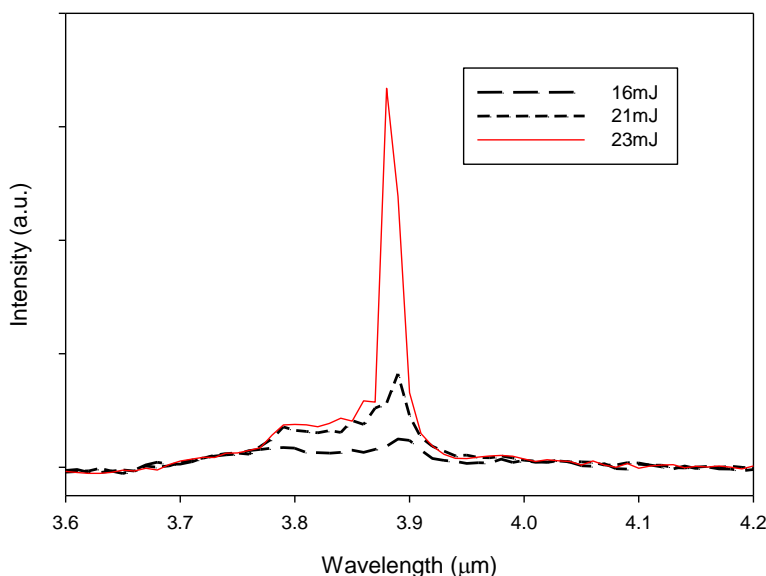
**Figure 90. A) Mid-infrared luminescence spectra of a Co:Fe:ZnS crystal under different pump energies at  $T = 14^\circ\text{K}$ , B) photoluminescence kinetics of a Co:Fe:ZnS crystal for different pump energies below (red) and above (pink) the laser threshold.**

## 5.2. Lasing of Co:Fe:ZnSe and Co:Fe:ZnS crystals *via* effective Co→Fe energy transfer under 0.76 $\mu\text{m}$ wavelength excitation

It was shown in the previous section that the strong absorption band between 650 and 800 nm in cobalt doped ZnS and ZnSe crystals could be utilized for the optical excitation of cobalt by commercially available high power laser diodes operating in this spectral range. The high concentration of co-dopants in Co:Fe:ZnSe and Co:Fe:ZnS crystals as well as the fast rate of energy transfer will provide the necessary high gain to enable lasing under pumping at 0.76  $\mu\text{m}$  without the need for an external cavity. The Co:Fe:ZnSe crystal used in these experiments had a cobalt concentration of  $6.4 \times 10^{18} \text{ cm}^{-3}$  and an iron concentration of  $19 \times 10^{18} \text{ cm}^{-3}$ , while the Co:Fe:ZnS crystal that was used had a cobalt concentration of  $8 \times 10^{18} \text{ cm}^{-3}$  and an iron concentration of  $10 \times 10^{18} \text{ cm}^{-3}$ .

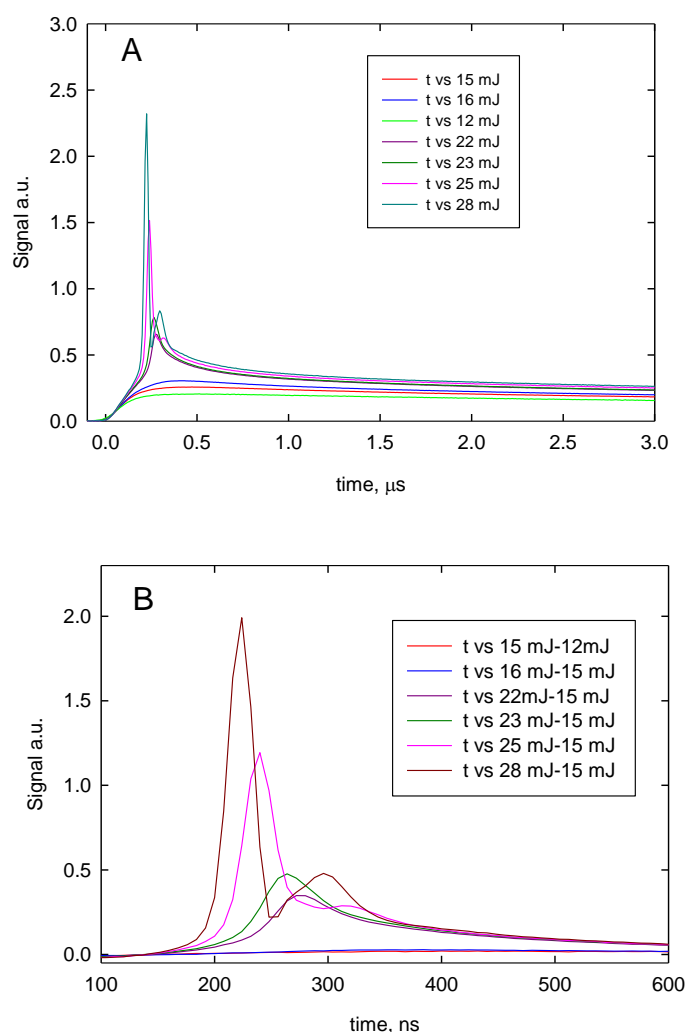
In the laser experiments, the pump radiation of an alexandrite laser was slightly focused to a spot diameter of  $\sim 2 \text{ mm}$  and the Co:Fe:ZnSe crystal was pumped at 760 nm. The crystal was contained in a closed-cycle refrigerator to enable adjustment of the temperature from 14 to 300°K. The luminescence spectra and kinetics were measured over a range of pump energies to show threshold behavior, Figure 89. Feedback in the crystal was provided by Fresnel reflections of  $\sim 18\%$  from each of the polished facets.

Figure 91 shows the photoluminescence spectra of the Co:Fe:ZnSe crystal for different pump energies. As one can see, at low pump energy, the measured PL spectra were typical for the luminescence of iron ions. The dependence of the PL spectrum profile on the pump energy demonstrated a threshold behavior accompanied by the appearance of a stimulated emission band around 3.85  $\mu\text{m}$ . The laser threshold was measured to be 19 mJ of pump power.



**Figure 91. Mid-infrared luminescence spectra of the Co:Fe:ZnSe crystal for different pump energies under 760 nm excitation at  $T = 14^\circ\text{K}$  measured below and above the laser threshold.**

The change of the luminescence profile above the laser threshold was accompanied by a shortening of PL kinetics as shown in Figure 92. For low pump energies, one can see the low temperature  $\text{Fe}^{2+}$  kinetics with a luminescence rise time  $\sim 0.5 \mu\text{s}$  followed by an exponential decay. Above the laser threshold, the kinetics exhibit the typical laser spike with a  $\sim 100 \text{ ns}$  pulse duration followed by below threshold luminescence kinetics. The temporal profile of the laser pulses were obtained by taking the difference between the measured kinetics and the normalized luminescence signals measured below the laser threshold. The results are shown in Figure 92B. As one can see from Figure 92, an increase in the pump energy results in a shortening of the onset of lasing as well as the pulse duration. Relaxation spikes with  $\sim 100 \text{ ns}$  between laser spikes were observed at high pump energy. The threshold dependence of emission, a significant line narrowing, as well as the shortening of the lifetime are clear evidence of Co:Fe:ZnSe lasing via the Co $\rightarrow$ Fe energy transfer mechanism.



**Figure 92. A) Co:Fe:ZnSe crystal photoluminescence kinetics for different pump energies at an excitation wavelength of 760 nm measured below and above the laser threshold at 14°K. B) Difference between the measured kinetics and the normalized luminescence signals measured below the laser threshold.**

### 5.3. Preliminary laser experiments with Co:ZnSe/ZnS crystals

Preliminary laser experiments were performed with Co:ZnSe and Co:ZnS Brewster cut samples under transverse pumping by a free running Alexandrite laser at 739.7 nm. The chosen samples are of the dimensions and concentrations shown in Table 16.

**Table 16. Properties of Co:ZnSe and Co:ZnS samples studied by pumping with a 739.7 nm laser.**

	Length (mm)	Width (mm)	Height (mm)	Co Concentration [cm <sup>-3</sup> ]
Co:ZnS (#811-14-06)	37	6	2.5	$1.76 \times 10^{19}$
Co:ZnSe (#811-29-11)	40	6.8	2.4	$2.15 \times 10^{19}$

RT mid-Infrared PL measurements at 739.7 nm under free running excitation of each sample are shown in Figure 93.

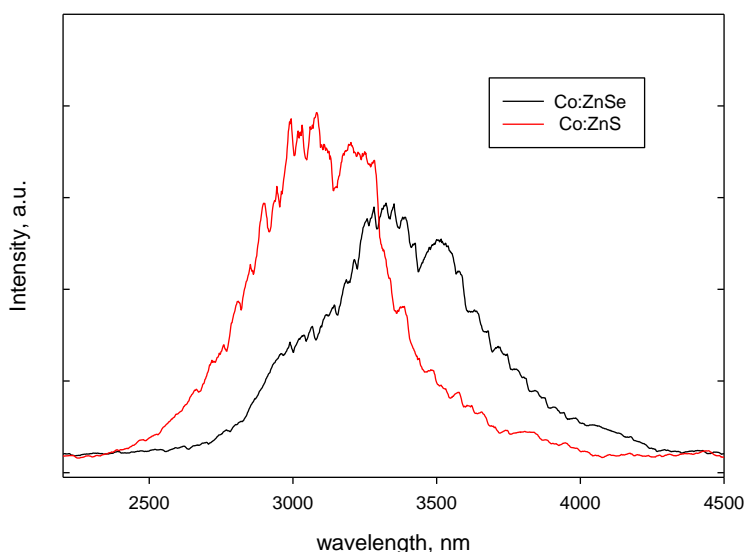


**Figure 93. Middle-Infrared PL spectra of Co:ZnS and Co:ZnSe.**

Figure 94 shows the RT photoluminescence kinetics of Co:ZnS and Co:ZnSe under excitation of the  $^4A_2(F) \rightarrow ^4T_2(P)$  transition. As one can see from Figure 94, the luminescence lifetime constants are equal to 208 and 167  $\mu$ s at RT for the Co:ZnSe and Co:ZnS crystals, respectively. The kinetic rise-time constants were measured to be less than the response time of the detection system ( $<0.5 \mu$ s). These results indicate that the upper laser level should accumulate a population and thereby create an inversion even under the relatively long free running pulses of the Alexandrite laser. Let's estimate the possible optical gain of Co:ZnSe/ZnSe active elements on the  $^4A_2(F) \rightarrow ^4T_2(F)$  transition under excitation with 100 mJ ( $N_{ph} = 3.7 \times 10^{17}$  photon @ 0.74  $\mu$ m) pulses from an Alexandrite laser. We will assume that quantum efficiency of the pump is equal to 1. By using a cylindrical lens in addition to taking advantage of the strong absorption of the

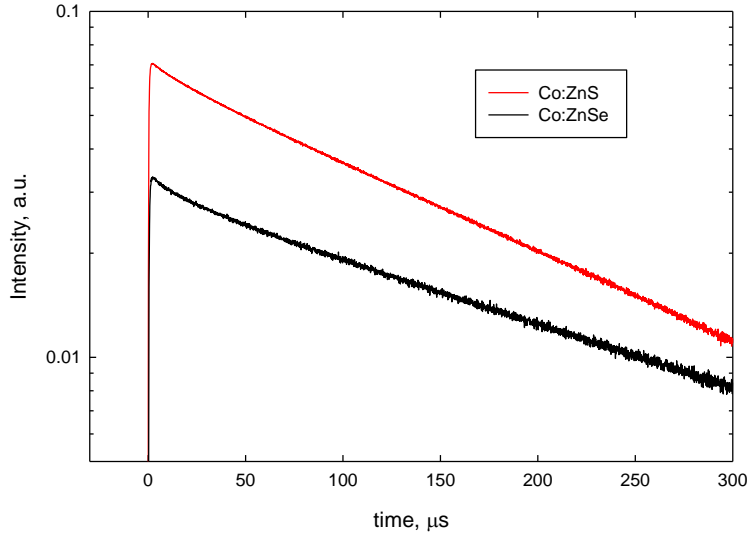


**Figure 94. PL kinetics of Co:ZnS and Co:ZnSe crystals**

pump radiation from an Alexandrite laser ( $k > 30 \text{ cm}^{-1}$ ), one can design a pump transfer geometry with an active channel area of  $A = 300 \times 300 \text{ μm}$ . In this geometry, the single pass gain could be estimated as:

$$G = \exp(N_{ph}\sigma_{em}/A) \approx \exp(7) \quad (70)$$

with  $\sigma_{em} \approx g_1/g_2 \cdot \sigma_{ab} \approx 1.7 \times 10^{-20} \text{ cm}^2$ . The laser performance of the Co:ZnSe/ZnS gain elements was tested in the experimental setup shown in Figure 95. In this setup, the output coupler had a reflectivity  $R > 98\%$  for wavelengths longer than  $3.5 \text{ μm}$ . In addition, the Alexandrite pump laser operated in the free running regime with an average power of  $1.4 \text{ W}$  with a repetition rate of  $13 \text{ Hz}$  at  $739.7 \text{ nm}$ .

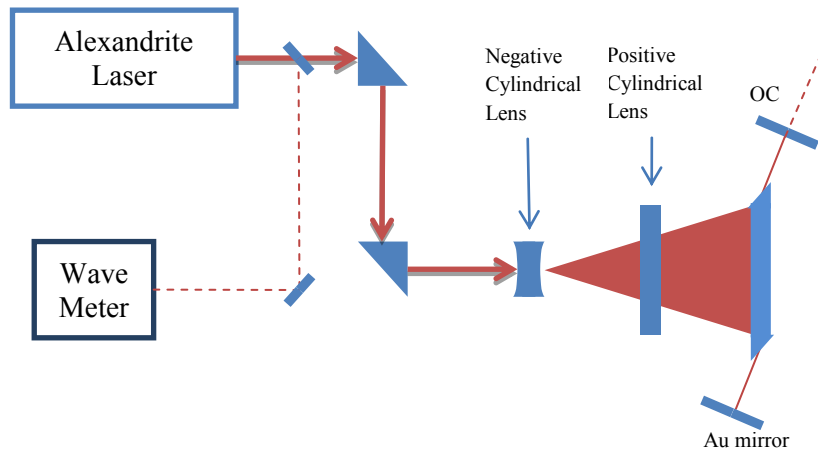


**Figure 95. Laser Experimental Setup.**

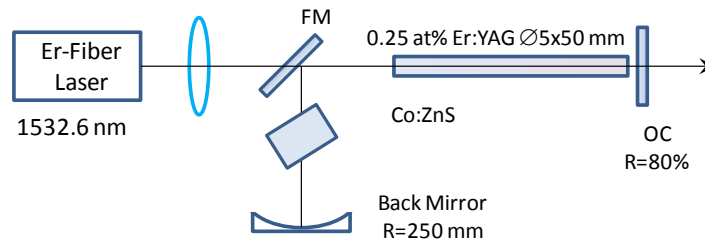


Unfortunately, under these experimental conditions Co:ZnS/ZnSe lasing was not detected. There are two major factors that could have prevented lasing at RT. First of all, it can be due to possible excited state absorption from the upper laser level ( ${}^4T_2 \rightarrow {}^4T_1$ ). The second reason could have to do with the branching ratio of relaxation processes from the pumped  ${}^4T_2(P)$  level. In addition to relaxation to the upper laser level  ${}^4T_2(P) \rightarrow {}^4T_2(F)$ , relaxation from the pumped level could also include relaxation to the ground level  ${}^4T_2(P) \rightarrow {}^4A_2(F)$ . The total pump efficiency depends on this ratio.

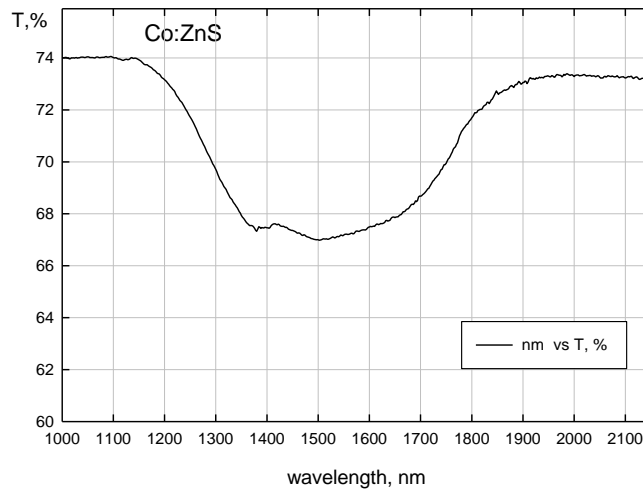
#### 5.4. Co:ZnSe saturable absorber for passively Q-switched Er:YAG lasers

Er:YAG lasers operating in the 1.6  $\mu\text{m}$  eyesafe spectral range ( ${}^4I_{13/2} \rightarrow {}^4I_{15/2}$  transition) are widely used in a variety of medical, scientific, and military applications. Direct resonant pumping into the  ${}^4I_{13/2}$  manifold by commercially available 1.532  $\mu\text{m}$  Er-fiber lasers results in a small quantum defect of  $\sim 7\%$  as well as a high, more than 80%, efficient laser. Cobalt and chromium doped II-VI crystals have been successfully utilized as passive saturable absorbers due to the absence of excited state absorption as well as having a high cross-section of saturation of  $\sim 10^{-18} \text{ cm}^2$ . The simplicity and compactness of TM:II-VI passive Q-switches is ideal for many applications. However, a 1.6  $\mu\text{m}$  Er-laser passively Q-switched by a Co doped II-VI material under continuous wave (CW) excitation was not reported yet. The purpose of this work was to verify whether or not a Co:ZnS crystal having a relatively long upper state relaxation time ( $\sim 200 \mu\text{s}$ ) could be effective as a passive Q-switch in erbium lasers.

The laser cavity configuration used in this experiment is depicted in Figure 96. A 1.1 mm pump beam from an ELR-20-1532.6-LP fiber laser (IPG Photonics Corp.) was focused into an Er:YAG laser rod (0.25 % at. Er:YAG, 5 mm $\times$ 50 mm) through a dichroic flat 45-degree folding mirror (HR @ 1600-1700 nm, AR @ 1532 nm) with a 300 mm AR-coated focusing lens. The laser scheme is based on a semiconcentric cavity design with a 250 mm end mirror and an 80% output coupler. ZnS doped with cobalt having an initial transmission of  $\sim 92\%$  at 1617 nm served as a saturable absorber and was placed at Brewster's angle 50 mm away from the dichroic mirror. The transmission spectrum of the Co:ZnS crystal utilized is shown in Figure 97 at normal incidence .

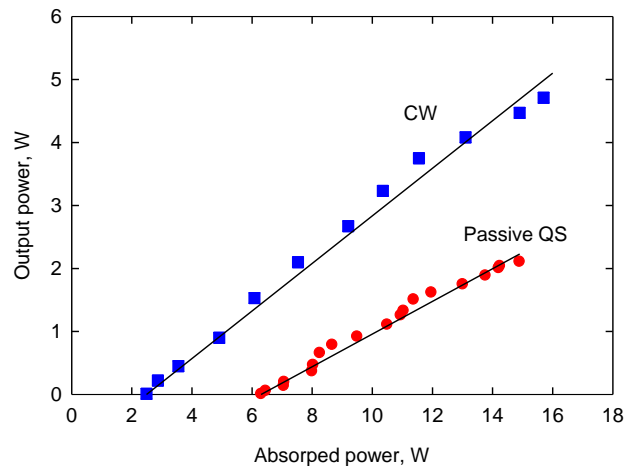


**Figure 96. Experimental setup.**



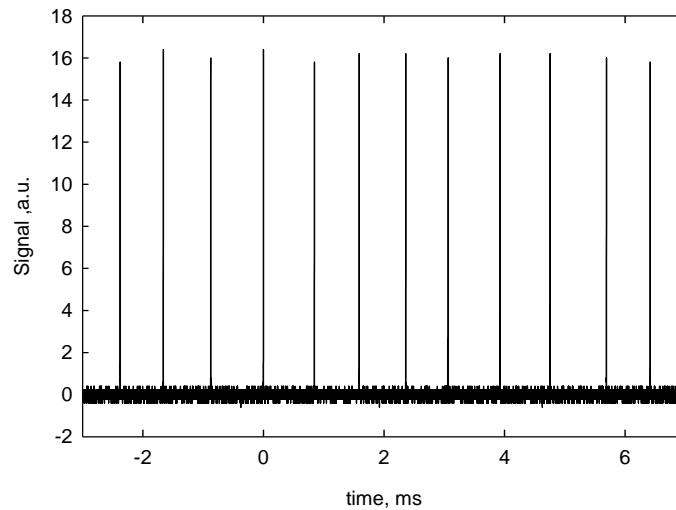
**Figure 97. Transmission spectrum of the Co:ZnS crystal.**

In Figure 98 are shown the input-output characteristics of the passively Q-switched Er:YAG laser with an initial transmission of the Co:ZnS passive crystal of 92%. The output power reached a level of 2.1 W when pumped with 16 W of incident power. The slope efficiency was 24% slope with a real optical efficiency of 14%. For comparison, CW oscillations of the Er:YAG laser were measured to have a 38% slope efficiency in the same cavity without the Co:ZnS crystal. The slope efficiency for operation in the passively Q-switched regime relative to CW operation was as high as 63%.



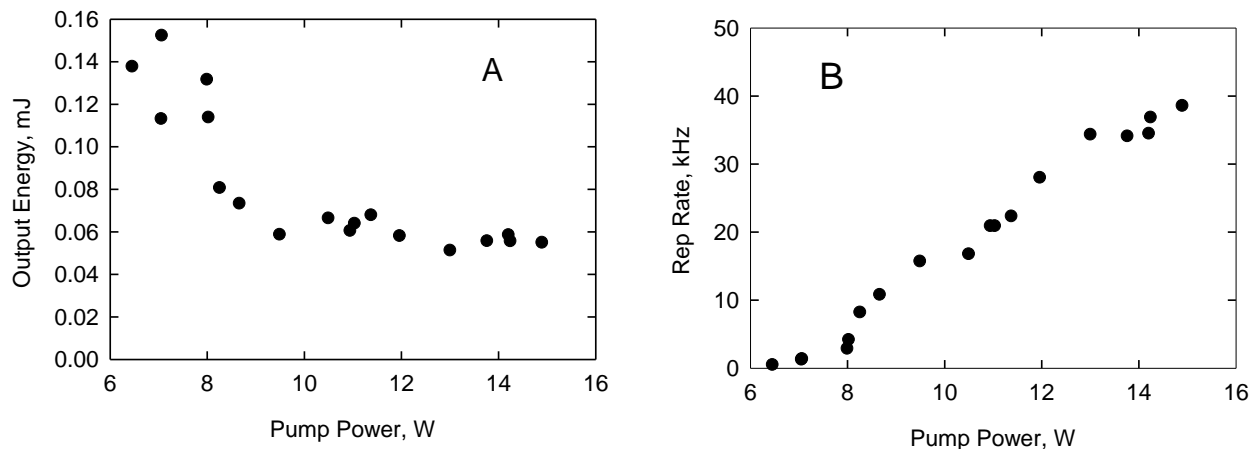
**Figure 98. Output power of a passively Q-switched and CW Er:YAG laser.**

Figure 99 represents a characteristic train of Q-Switched Er:YAG pulses obtained from the laser with an input power of 7.4 W. As one can see for this pump power, the passively Q-switched Er:YAG laser operates at repetition rate of 1.25 kHz and features a stable output pulse energy of 0.1 mJ.



**Figure 99. Train of output pulses from a passively Q-switched Er:YAG laser at a pump power of 7.4 W.**

According to a simple model of the passively Q-switched regime of operation, the pulse energy is defined by the initial transmission of the absorber and is not sensitive to a variation in the pump power. As one can see from Figure 100A, the output energy of a passively Q-switched Ho:YAG laser is approximately stable with increases in the pump power to more than 30% of the laser threshold. Figure 100B shows the repetition rate of a passively Q-switched Er:YAG laser versus the incident pump power. The maximum estimated repetition rate was 38 kHz.



**Figure 100. Output energy (A) and repetition rate (B) of the passively Q-switched Er:YAG laser.**

Finally, oscillation pulses of duration 0.5-1.2  $\mu\text{s}$  from the passively Q-switched cavity showed no evidence of the mode beating associated with multimode operation (see Figure 101.)

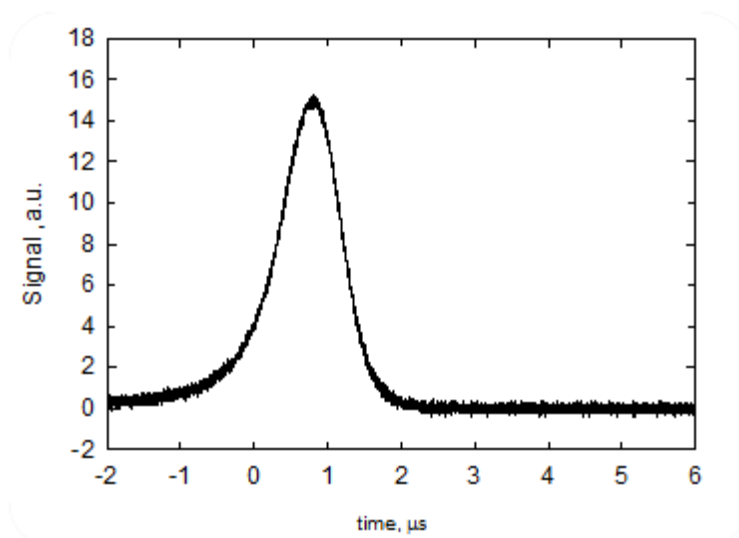


Figure 101. Temporal profile of the passively Q-switched output pulses.

## 6.0 CONCLUSIONS

The technology of high optical quality gain elements based on Co, Ni, and Fe doped ZnSe and ZnS crystals which are promising for room-temperature lasing was developed. Multiple co-doped ZnSe and ZnS crystals have been fabricated and studied via absorption and photoluminescence spectroscopy. For the first time, lasing was achieved on Fe ions in ZnS and ZnSe crystals co-doped with Co via effective Co-Fe energy transfer. For the first time, Co:ZnS crystals were successfully used for passive Q-switching of CW pumped Er:YAG 1645 nm lasers.

We developed a theory to describe the properties of TMs in II-VI materials taking into account all of the operators necessary to describe the ion interactions associated with  $3d^n$  electronic configurations ( $n = 2, 3, 4, 6, 7$ , and  $8$ ) to include the electrostatic and spin-orbit interactions as well as the influence of the crystal field and external magnetic field on the electronic energy. For the ions  $\text{Co}^{2+}$ ,  $\text{Fe}^{2+}$ , and  $\text{Ni}^{2+}$ , we derived explicit formulas for the energy interaction matrices.

We constructed a system for calculating the eigenvalues of the energy matrices based on the quantum numbers of an orthogonal group of three-dimensional rotation states of the ions as well as two electrostatic parameters ( $F_{22}$ ,  $F_{44}$ , ( $B$ ,  $C$ )), the spin-orbit parameter  $\xi_{3d}$ , plus the 13 parameters  $A_{kq}$  ( $k = 2, 4$ ) which describe a crystal field of any symmetry.

The matrices which were calculated are a modern alternative of the Tanabe-Sugano matrices, which happen to be a particular case of the matrices that we developed, i.e., the case where  $\xi_{3d}=0$  and the crystal field has cubic symmetry with a single parameter  $Dq$  that depends on the strong crystal field wave-function basis.

We created matrices to calculate the intensities of electro-dipole transitions arising from odd potentials of a crystal field having tetrahedral symmetry. The matrices enabled calculation of the oscillator strengths and lifetimes for all transitions of the  $3d^n$  ( $n = 2, 3, 4, 6, 7$ , and  $8$ ) electronic configuration. In addition, they allow the computation of the oscillator strengths and lifetimes of all transitions in the absorption and fluorescence spectra, as well as fluorescence and absorption spectra for transitions to and from excited states. We further developed a method to find the intensity parameters from the experimental values of the fluorescence transition lifetimes. These values are then used to calculate the oscillator strengths and lifetimes of all the other transitions in spectra of various types.

We developed the principles for modeling spectra. To determine the bandwidths of the transitions that identify the spectra of  $3d^n$  ( $n = 2, 3, 4, 6, 7$ , and  $8$ ) ions in semiconductor crystals, we considered the oscillator strengths versus the transition energies. We coordinated the experimental and theoretical results by fitting the modeled spectra to the experimental data.

We created a method to calculate the configuration curves of the energy levels taking into account the vibration amplitudes of the surrounding atoms. We developed energy and intensity matrices and approximated the crystal field parameters of the zeroth and fourth order by the parabolic vibration amplitude dependencies. Configuration diagrams are calculated for the  $\text{Co}^{2+}$ ,  $\text{Fe}^{2+}$ , and  $\text{Ni}^{2+}$  ions and as well as various anharmonic cases.

The theory that was created was used to analyze experimental data from the literature for  $\text{Co}^{2+}$ ,  $\text{Fe}^{2+}$ , and  $\text{Ni}^{2+}$  ions in ZnSe and good agreement was obtained between the experimental and modeled spectra.

To conclude, all of the theory and application methods were originally developed.

## 7.0 REFERENCES

- [1] J.J. Adams et al, "4.0–4.5- $\mu\text{m}$  lasing of Fe:ZnSe below 180 K, a new mid-infrared laser material", *Optics Letters* **24**(23)(1999)1720-1722.
- [2] L. D. DeLoach, R. H. Page, G. D. Wilke, S. A. Payne, W. F. Krupke, "Transition metal-doped zinc chalcogenides: spectroscopy and laser demonstration of a new class of gain media", *IEEE Journal of Quantum Electronics* **32**(1996)885.
- [3] T. Sorokina, " $\text{Cr}^{2+}$ -doped II–VI materials for lasers and nonlinear optics", *Optical Materials* **26**(2004)395.
- [4] V.V. Fedorov, S.B. Mirov, A. Gallian, D. V. Badikov, M.P. Frolov, Y.V. Korostelin, V.I. Kozlovsky, A.I. Landman, Y.P. Podmar'kov, V.A. Akimov, A.A. Voronov, "3.77-5.05- $\mu\text{m}$  tunable solid state lasers based on  $\text{Fe}^{2+}$ -doped ZnSe crystals operating at low and room temperatures", *IEEE J. of Quantum Electronics* **42**(9)(2006)907-917.
- [5] S. Mirov, V. Fedorov, I. Moskalev, D. Martyshkin, invited paper, "Recent progress in transition metal doped II-VI mid-IR lasers", *IEEE Journal of Selected Topics in Quantum Electronics* **13**(3)(2007)810.
- [6] S.B.Mirov and V.V.Fedorov, "New regimes of excitation and mid-IR lasing of transition metal doped II-VI crystals", invited chapter in the Springer book *Mid-Infrared Coherent Sources And Applications*", Editors, Majid Ebrahimzadeh and Irina T. Sorokina, **314**(2008)261.
- [7] S. Mirov, "Investigation of Co, Ni, and Fe doped II-VI chalcogenides", Kirtland AFB-UAB Contract FA9451-10-C-0254, First year report.
- [8] S.B. Mirov, V.V. Fedorov, I.S. Moskalev, D. Martyshkin, C. Kim, "Progress in  $\text{Cr}^{2+}$  and  $\text{Fe}^{2+}$  doped mid-IR laser materials", (invited review) *Laser & Photonics Review*, **4**(1)(2010)21-41.
- [9] E. F. Kustov, "Calculation of energy matrices of  $d^n$  the configuration ( $n=2,3,7, 8$ ) in a crystal field having T symmetry", *Crystallography* **18**(1)(1973)26-31. (Кустов Е.Ф. Расчет матриц энергии конфигураций  $d^n$  во внутрикристаллическом поле с симметрией T ( $n=2,3,7,8$ )). Кристаллография, 1973, Т.**18**, №1, С.26-31).
- [10] E.F. Kustov et al., "Electronic spectra of rare earth compositions" (in Russian Электронные спектры соединений редкоземельных элементов) М., Наука, 1981, с.303.
- [11] A. P. Jucys, A.J. Savukynas, "Mathematical foundations of the atomic theory" (in Russian Математические основы теории атома) Inst. Phys. and Mat. Vilnius, 1973, p.479.
- [12] M. Rotenberg, R. Bivins, N. Metropolis, J.K. Wooten, "The 3j and 6j symbols", MIT, Cambridge. Massachusetts Press, 1959, p. 497.
- [13] E.F. Kustov, "Subgroup coefficients of point groups", M. Standard. 1982. page 316 (in Russian).
- [15] Physics and chemistry of  $A^{II}B^{VI}$  compounds, ed. by S. A. Medvedev, Moscow, Mir 1970.
- [16] Yu. F. Vaksman, V. V. Pavlov, Yu. A. Nitsuk, Yu. N. Purtov, A.S. Nasibov, P. V. Shapkin, "Optical absorption and photoconductivity of ZnSe:Co single crystals", *Functional Materials* **14**(4)(2007)426.
- [17] J. M. Baranowski, J. W. Allen, and G. L. Pearson, "Crystal-field spectra of  $3d^n$  impurities in II-VI and III-V compound semiconductors", *Physical Review* **160**(3)(1967)627.
- [18] Ming Luo, N. Y. Garces, N. C. Giles, Utpal N. Roy, Yunlong Cui, and Arnold Burger, "Optical and electron paramagnetic resonance spectroscopies of diffusion-doped

- Co<sup>2+</sup>:ZnSe”, Journal of Applied Physics **99**(2006)073709.
- [14] J. Dreyhsig and B. Litzenburger, “Nature of optical transitions in the charge-transfer region of ZnS:Co and ZnSe:Co”, Physical Review **B54**(15)(1996)10516.
  - [29] Tzong-Yow Tsai and Milton Birnbaum, “Co<sup>2+</sup>:ZnS and Co<sup>2+</sup>:ZnSe saturable absorber Q switches”, Journal of Applied Physics **87**(1)(2000)25.
  - [20] Ming Luo, “Transition-metal ions in II-VI semiconductors: ZnSe and ZnTe”, Dissertation submitted to the Eberly College of Arts and Sciences at West Virginia University, Morgantown, West Virginia, 2006.
  - [21] Umit Demirbas, Alphan Sennaroglu, Mehmet Somer, “Synthesis and characterization of diffusion-doped Cr<sup>2+</sup>:ZnSe and Fe<sup>2+</sup>:ZnSe”, Optical Materials **28**(2006)231-240.
  - [22] N. Myoung, V. V. Fedorov, and S. B. Mirov, “Optically dense Fe:ZnSe crystals for energy scaled gain switched lasing”, Proceedings of the SPIE **7578**(2010)75781H.
  - [23] B. Henderson, R.H. Bartran, “Crystal-Field Engineering of Solid-State Laser Materials”, Cambridge University Press, Cambridge (2000).
  - [24] W.F. Krupke, “Induced-emission cross-sections in neodymium laser glasses”, IEEE Journal of Quantum Electronics **10**(1974)450.
  - [25] L. Podlowski, R. Heitz, P. Thurian, A. Hoffmann, I. Broser, “Nonradiative transition rates of Fe<sup>2+</sup> in III-V and II-VI semiconductors”, Journal of Luminescence **58**(1-6)(1994)252-256 (1994).
  - [26] Z. Mierczyk, A. Majchrowski, K. Ozga, A. Slezak, I.V. Kityk, “Simulation of nonlinear optical absorption in ZnSe:Co<sup>2+</sup> crystals”, Optics and Laser Technology, **38**(7)(2006)558-564.
  - [27] A. V. Podlipensky, V. G. Shcherbitsky, N. V. Kuleshov, V. P. Mikhailov, V. I. Levchenko, and V. N. Yakimovich, “Cr<sup>2+</sup>:ZnSe and Co<sup>2+</sup>:ZnSe saturable-absorber Q switches for 1.54- $\mu$ m Er:glass lasers”, Optics Letters **24**(14)(1999)960-962.
  - [28] Shcherbitsky, V. G., Girard, S., Fromager, M., Moncorge, J. R., Kuleshov, N. V., Levchenko, V. I., Yakimovich, V. N., et al. “Accurate method for the measurement of absorption cross sections of solid-state saturable absorbers”, Applied Physics **B74**(2002)367-374.

### A.1 Program for calculation of the spectra of $\text{TM}^{2+}:\text{ZnSe}$

[illegible][illegible]

The program outlined below calculates the matrix elements of interaction.

$$\begin{aligned}
& > F(j,k); \text{ if } j < k \text{ then } 0 \quad \text{else } (j-k)! \\
> FS(j_1, j_2, j_3, l_1, l_2, l_3, k) &= k! * F(j_1 + j_2 - j_3, k) * F(l_1 + l_2 - j_3, k) * F(j_1 + l_2 - l_3, k) * F(l_1 + j_2 - \\
& \quad l_3, k) * F(j_3 + l_3 + k, j_1 + l_1) * F(j_3 + l_3 + k, j_2 + l_2); \\
> C_1(j_1, j_2, j_3) &= [(F(j_1 + j_2, j_3) * F(j_1 + j_3, j_2) * F(j_2 + j_3, j_1) / (j_1 + j_2 + j_3 + 1)!)]^{0.5}; \\
> FS_1(j_1, j_2, j_3, l_1, l_2, l_3, k) &= \text{if } FS(j_1, j_2, j_3, l_1, l_2, l_3, k) = 0 \text{ then } 0 \\
& \quad \text{else } (-1)^k * F(j_1 + j_2 + l_1 + l_2 + 1, k) / FS(j_1, j_2, j_3, l_1, l_2, l_3, k).
\end{aligned} \tag{73}$$
$$\begin{aligned}
& > 6J(j_1, j_2, j_3, l_1, l_2, l_3) = (-1)^{j_1 + j_2 + l_1 + l_2} * \\
& C_1(j_1, j_2, j_3) * C_1(l_1, l_2, j_3) * C_1(l_1, j_2, l_3) * C_1(j_1, l_2, l_3) * (FS_1(j_1, j_2, j_3, l_1, l_2, l_3, 0) + \\
& FS_1(j_1, j_2, j_3, l_1, l_2, l_3, 1) + FS_1(j_1, j_2, j_3, l_1, l_2, l_3, 2) + FS_1(j_1, j_2, j_3, l_1, l_2, l_3, 3) +
\end{aligned}$$



$$\begin{aligned} &FS_1(j_1,j_2,j_3,l_1,l_2,l_3,4)+FS_1(j_1,j_2,j_3,l_1,l_2,l_3,5)+FS_1(j_1,j_2,j_3,l_1,l_2,l_3,6)+ \\ &FS_1(j_1,j_2,j_3,l_1,l_2,l_3,7)+FS_1(j_1,j_2,j_3,l_1,l_2,l_3,8)+FS_1(j_1,j_2,j_3,l_1,l_2,l_3,9)+ \\ &FS_1(j_1,j_2,j_3,l_1,l_2,l_3,10)+FS_1(j_1,j_2,j_3,l_1,l_2,l_3,11)+FS_1(j_1,j_2,j_3,l_1,l_2,l_3,12)+ \\ &FS_1(j_1,j_2,j_3,l_1,l_2,l_3,13)+FS_1(j_1,j_2,j_3,l_1,l_2,l_3,14)). \end{aligned} \quad (74)$$

3. The six momenta vector summation coefficient is given by:

$$\begin{aligned} 6JJ(j_1,j_2,j_3,l_1,l_2,l_3) &= 6J(j_1,j_2,j_3,l_1,l_2,l_3)* \\ &(-1)^{j_1+j_2+l_1+l_2}[(2j_3+1)*(2l_3+1)]^{0.5}. \end{aligned} \quad (75)$$

4. The Clebsch-Gordon coefficients are:

$$\begin{aligned} G_1(j_1,j_2,j_3,m_1,m_2,m_3) &= [(F(j_1+j_2,j_3)*F(j_1+j_3,j_2)*F(j_2+j_3,j_1)* \\ &(j_1+m_1)!(j_1-m_1)!(j_2+m_2)!(j_2-m_2)!(j_3+m_3)!(j_3-m_3)!/(j_1+j_2+j_3+1)!]^{0.5}; \\ FG(j_1,j_2,j_3,m_1,m_2,m_3,z) &= z!*F(j_1+j_2-j_3,z)*F(j_1-m_1,z)* \\ &F(j_2+m_2,z)*F(j_3+z,j_2-m_1)*F(j_3+z,j_1+m_2); \\ FG_1(j_1,j_2,j_3,m_1,m_2,m_3,z) &= \text{if } FG(j_1,j_2,j_3,m_1,m_2,m_3,z)=0 \text{ then } 0 \\ &\text{else } (-1)^z/FG(j_1,j_2,j_3,m_1,m_2,m_3,z). \end{aligned} \quad (76)$$

5. The 3J coefficients are given by:

$$\begin{aligned} 3J(j_1,j_2,j_3,m_1,m_2,m_3) &= (-1)^{j_1-j_2-m_3} * G_1(j_1,j_2,j_3,m_1,m_2,m_3)* \\ &(FG_1(j_1,j_2,j_3,m_1,m_2,m_3,0)+FG_1(j_1,j_2,j_3,m_1,m_2,m_3,1)+FG_1(j_1,j_2,j_3,m_1,m_2,m_3,2) \\ &+FG_1(j_1,j_2,j_3,m_1,m_2,m_3,3)+FG_1(j_1,j_2,j_3,m_1,m_2,m_3,4)+FG_1(j_1,j_2,j_3,m_1,m_2,m_3,5) \\ &+FG_1(j_1,j_2,j_3,m_1,m_2,m_3,6)+FG_1(j_1,j_2,j_3,m_1,m_2,m_3,7)+FG_1(j_1,j_2,j_3,m_1,m_2,m_3,8) \\ &+FG_1(j_1,j_2,j_3,m_1,m_2,m_3,9)+FG_1(j_1,j_2,j_3,m_1,m_2,m_3,10)+FG_1(j_1,j_2,j_3,m_1,m_2,m_3,11) \\ &+FG_1(j_1,j_2,j_3,m_1,m_2,m_3,12)+FG_1(j_1,j_2,j_3,m_1,m_2,m_3,13)+FG_1(j_1,j_2,j_3,m_1,m_2,m_3,14)). \end{aligned} \quad (77)$$

6. The zero projection 3J coefficients are:

$$\begin{aligned} 3J_0(j_1,j_2,j_3) &= (-1)^{(j_1+j_2+j_3)/2} * \\ &[F(j_2+j_3,j_1)*F(j_1+j_3,j_2)*F(j_1+j_2,j_3)/(j_1+j_2+j_3+1)!]^{0.5} * ((j_1+j_2+j_3)/2)! / \\ &F((j_1+j_2+j_3)/2,j_1)/F((j_1+j_2+j_3)/2,j_2)/F((j_1+j_2+j_3)/2,j_3). \end{aligned} \quad (78)$$

7. The matrix elements of electrostatic interaction are:

$$\begin{aligned} fd(l_1,l_2,S,L) &= f_k(l_1,l_2,L,0)*Cf_k(l_1,l_2,0)*F_0+f_k(l_1,l_2,L,2)*Cf_k(l_1,l_2,2) \\ &*F_2+f_k(l_1,l_2,L,4)*Cf_k(l_1,l_2,4)*F_4+(-1)^S*(g_k(l_1,l_2,L,1)*Cg_k(l_1,l_2,1)* \\ &G_1+g_k(l_1,l_2,L,3)*Cg_k(l_1,l_2,3)*G_3+g_k(l_1,l_2,L,5)*Cg_k(l_1,l_2,5)*G_5). \end{aligned} \quad (79)$$

8. More specifically, the Clebsch-Gordon coefficients are calculated as:

$$\begin{aligned} KGz(j_1,j_2,j_3,m_1,m_2,m_3,z) &= \text{if } j_1+j_2-j_3 < 0 \text{ then } 0 \text{ elif } m_1+m_2-m_3 < 0 \text{ then } 0 \\ &0 \text{ elif } j_1+j_3-j_2 < 0 \text{ then } 0 \text{ elif } j_2+j_3-j_1 < 0 \text{ then } 0 \text{ elif } j_1+m_1 < 0 \\ &\text{then } 0 \text{ elif } j_1-m_1 < 0 \text{ then } 0 \text{ elif } j_2+m_2 < 0 \text{ then } 0 \text{ elif } j_2-m_2 < 0 \text{ then } 0 \\ &0 \text{ elif } j_3+m_3 < 0 \text{ then } 0 \text{ elif } j_3-m_3 < 0 \text{ then } 0 \text{ elif } j_1+j_2-j_3-z < 0 \text{ then } 0 \\ &0 \text{ elif } j_1-m_1-z < 0 \text{ then } 0 \text{ elif } j_2+m_2-z < 0 \text{ then } 0 \text{ elif } j_3+z-j_2+m_1 < 0 \\ &\text{then } 0 \text{ elif } j_3+z-j_1-m_2 < 0 \text{ then } 0 \text{ else } [(2*j_3+1)*(j_1+j_2-j_3)!*(j_1+j_3-j_2)! \\ &*(j_2+j_3-j_1)!*(j_1+m_1)!*(j_1-m_1)!*(j_2+m_2)!*(j_2-m_2)!*(j_3+m_3)!* \\ &(j_3-m_3)!/(j_1+j_2+j_3+1)!]^{0.5} * ((-1)^z/(z!*(j_1+j_2-j_3-z)!*(j_1-m_1-z)!* \\ &(j_2+m_2-z)!*(j_3+z-j_2+m_1)!*(j_3+z-j_1-m_2)!)); \end{aligned} \quad (80)$$

$$\begin{aligned}
KG(j_1, j_2, j_3, m_1, m_2, m_3) = & KGz(j_1, j_2, j_3, m_1, m_2, m_3, 0) + KGz(j_1, j_2, j_3, m_1, m_2, m_3, 1) \\
& + KGz(j_1, j_2, j_3, m_1, m_2, m_3, 2) + KGz(j_1, j_2, j_3, m_1, m_2, m_3, 3) + KGz(j_1, j_2, j_3, m_1, m_2, m_3, 4) \\
& + KGz(j_1, j_2, j_3, m_1, m_2, m_3, 5) + KGz(j_1, j_2, j_3, m_1, m_2, m_3, 6) + KGz(j_1, j_2, j_3, m_1, m_2, m_3, 7) \\
& + KGz(j_1, j_2, j_3, m_1, m_2, m_3, 8) + KGz(j_1, j_2, j_3, m_1, m_2, m_3, 9) + KGz(j_1, j_2, j_3, m_1, m_2, m_3, 10) \\
& + KGz(j_1, j_2, j_3, m_1, m_2, m_3, 11) + KGz(j_1, j_2, j_3, m_1, m_2, m_3, 12) + KGz(j_1, j_2, j_3, m_1, m_2, m_3, 13) \\
& + KGz(j_1, j_2, j_3, m_1, m_2, m_3, 14) + KGz(j_1, j_2, j_3, m_1, m_2, m_3, 15) + KGz(j_1, j_2, j_3, m_1, m_2, m_3, 16) \\
& + KGz(j_1, j_2, j_3, m_1, m_2, m_3, 17) + KGz(j_1, j_2, j_3, m_1, m_2, m_3, 18) + KGz(j_1, j_2, j_3, m_1, m_2, m_3, 19) \\
& + KGz(j_1, j_2, j_3, m_1, m_2, m_3, 20).
\end{aligned} \tag{81}$$

9. The Clebsch-Gordon coefficients from the Wigner theorem of one-electron operator matrix elements are defined as:

$$J_{31}(j_1, j_2, j_3, m_1, m_2, m_3); KG(j_3, j_2, j_1, -m_3, m_2, -m_1)/(2j_1+1)^{0.5}. \tag{82}$$

10. Genealogical coefficients are:

$$\begin{aligned}
Gen := & \text{matrix}([[-(8/15)^{0.5}, -(7/15)^{0.5}, 0, 0, 0], \\
& [-1/5^{0.5}, 2/5^{0.5}, 0, 0, 0], \\
& [(7/30)^{0.5}, -2/15^{0.5}, 0, 1/2^{0.5}, 0], \\
& [-1/2*(3/5)^{0.5}, -1/2*(7/5)^{0.5}, 2/15^{0.5}, -1/2*3^{0.5}, -1/2*(3/5)^{0.5}], \\
& [-1/2*(7/5)^{0.5}, 1/2*(3/5)^{0.5}, 0, 3/2*7^{0.5}, -1/2*(5/7)^{0.5}], \\
& [(2/5)^{0.5}, 1/10^{0.5}, 0, -1/7^{0.5}, -(5/14)^{0.5}], \\
& [0, 1/2^{0.5}, 0, -(5/21)^{0.5}, (11/42)^{0.5}], \\
& [0, -1/2^{0.5}, 0, 0, 1/2^{0.5}]]).
\end{aligned} \tag{83}$$

11. The matrix elements of electrostatic interaction in the  $d^3$  configuration are:

$$\begin{aligned}
V_{qq}(n_1, n_2, k) = & 3*(Gen[n_1, 1]*Gen[n_2, 1]*(-1)^1*6J(2, 2, 1, 2, 2, k) \\
& + Gen[n_1, 2]*Gen[n_2, 2]*(-1)^3*6J(2, 2, 3, 2, 2, k) + \\
& Gen[n_1, 3]*Gen[n_2, 3]*(-1)^0*6J(2, 2, 0, 2, 2, k) + \\
& Gen[n_1, 4]*Gen[n_2, 4]*(-1)^2*6J(2, 2, 2, 2, 2, k) + Gen[n_1, 5]* \\
& Gen[n_2, 5]*(-1)^4*6J(2, 2, 4, 2, 2, k))*25*(3J_0(2, k, 2, 0, 0, 0))^2.
\end{aligned} \tag{84}$$

12. The matrix elements of the electrostatic interaction with parameters are:

$$q(n_1, n_2) = V_{qq}(n_1, n_2, 0)*F_0 + V_{qq}(n_1, n_2, 2)*F_2 + V_{qq}(n_1, n_2, 4)*F_4. \tag{85}$$

13. The matrix elements of the spin-orbit interaction in the  $d^3$  configuration are:

$$\begin{aligned}
W^{11}(n_1, n_2, L_1, L_2, S_1, S_2) = & 3*(-1)^{(L_1+S_1-1/2+1)*} \\
& [3/2*(2L_1+1)(2L_2+1)(2S_1+1)(2S_2+1)]^{0.5}*(Gen[n_1, 1]*Gen[n_2, 1]* \\
& 6J(1, 2, L_1, 1, L_2, 2)*6J(1, 1/2, S_1, 1, S_2, 1/2) + Gen[n_1, 2]*Gen[n_2, 2]* \\
& 6J(3, 2, L_1, 1, L_2, 2)*6J(1, 1/2, S_1, 1, S_2, 1/2) + Gen[n_1, 3]*Gen[n_2, 3]* \\
& 6J(0, 2, L_1, 1, L_2, 2)*6J(0, 1/2, S_1, 1, S_2, 1/2) + Gen[n_1, 4]*Gen[n_2, 4]* \\
& 6J(2, 2, L_1, 1, L_2, 2)*6J(0, 1/2, S_1, 1, S_2, 1/2) + Gen[n_1, 5]*Gen[n_2, 5]* \\
& 6J(4, 2, L_1, 1, L_2, 2)*6J(0, 1/2, S_1, 1, S_2, 1/2)); \\
J(n_1, n_2, L_1, L_2, S_1, S_2, J) = & (2*3*5)^{0.5}*(-1)^{J+L_1+S_2}*6J(L_1, L_2, 1, S_2, S_1, J)* \\
& W^{11}(n_1, n_2, L_1, L_2, S_1, S_2).
\end{aligned} \tag{86}$$

14. The matrix elements of the tensor operators  $U_k$  are:

$$U_k(n_1, n_2, S, L_1, L_2, k); 3*(-1)^{L_1}*((2L_1+1)*(2L_2+1))^{0.5}*(Gen[n_1, 1]*$$

$$\begin{aligned} & \text{Gen}[n_2,1]*(-1)^1*6J(2,L_1,1,L_2,2,k)+\text{Gen}[n_1,2]*\text{Gen}[n_2,2]*(-1)^3* \\ & 6J(2,L_1,3,L_2,2,k)+\text{Gen}[n_1,3]*\text{Gen}[n_2,3]*(-1)^0*6J(2,L_1,0,L_2,2,k)+ \\ & \text{Gen}[n_1,4]*\text{Gen}[n_2,4]*(-1)^2*6J(2,L_1,2,L_2,2,k)+\text{Gen}[n_1,5]* \\ & \text{Gen}[n_2,5]*(-1)^4*6J(2,L_1,4,L_2,2,k)). \end{aligned} \quad (87)$$

15. The matrix elements of the crystal field potential are:

$$\begin{aligned} & \text{Crd}_3(n_1,n_2,S,L_1,L_2,J_1,J_2,k)=(-1)^{(S+L_2+J_1+k)*} \\ & [(2J_1+1)*(2J_2+1)]^{0.5}*6J(J_1,J_2,k,L_2,L_1,S)*U_k(n_1,n_2,S,L_1,L_2,k). \end{aligned} \quad (88)$$

16. The matrix elements of the angular momentum L are:

$$\begin{aligned} & \text{MuL}(S,L_1,L_2,J_1,J_2);(-1)^{(L_1+S+J_2)*} [(L_1*(L_1+1)*(2L_1+1)*(2J_1+1)*(2J_2+1)]^{0.5} \\ & *6J(L_1,J_1,S,J_2,L_2,1). \end{aligned} \quad (89)$$

17. The matrix elements of spin angular momentum S are:

$$\begin{aligned} & \text{MuS}(S,L_1,L_2,J_1,J_2)=\text{if } L_1=L_2 \text{ then } 2(-1)^{(L_1+S+J_1)*} \\ & [S*(S+1)*(2S+1)*(2J_1+1)*(2J_2+1)]^{0.5}*6J(S,J_1,L_1,J_2,S,1) \text{ else } 0. \end{aligned} \quad (90)$$

18. The matrix elements of the electro-dipole operator are:

$$\begin{aligned} & > Q_1(l_1,l_2,S,L_1,L_2,J_1,J_2)=(-1)^{(l_1+l_2+S+J_2)*} \\ & [(2L_1+1)*(2L_2+1)*(2J_1+1)*(2J_2+1)]^{0.5}*6J(l_2,L_1,l_1,L_2,l_2,1)*6J(L_1,J_1,S,J_2,L_2,1) \\ & *[(2l_1+1)*(2l_2+1)]^{0.5}*(-1)^{((l_1+l_2+1)/2)*}3J(l_2,1,l_1,0,0,0). \end{aligned} \quad (91)$$

19. Finally, the matrix elements of the g-factor are:

$$g(S,L,J)=1+(J(J+1)-L(L+1)+S(S+1))/2J/(J+1). \quad (92)$$

### A.3 Program for calculation of the eigenvectors and eigenvalues of the total matrix A

The total matrix A is a summation of the matrices of the:

1. Electrostatic interaction with parameters  $F_{22}$  and  $F_{44}$ , which correspond to the Slater parameters as  $F_k^k=F_{kk}$ ,  $F_{22}=F_2/49$ ,  $F_{44}=F_4/441$ ;
2. Spin-orbit interaction with the parameter  $\xi_{3d}$ ;
3. Crystal field with the second-order parameters  $A_{20}, A_{21}, A_{2-1}, A_{22}, A_{2-2}$ , and the fourth-order parameters  $A_{40}, A_{41}, A_{4-1}, A_{42}, A_{4-2}, A_{43}, A_{4-3}, A_{44}, A_{4-4}$ .

Maple calculates the eigensystem as:

$$> \text{Eigenvals}(A,\text{vecs}): \text{vecs}: M:=(\text{vecs}(\%)): M1:=\text{evalm}(1/M): \text{Ksi}:=[\text{eigenvals}(A)]: \quad (93)$$

And the energy of the transition between the first and  $n^{\text{th}}$  levels is given by:

$$E(n)=\text{Ksi}[n]-\text{Ksi}[1]. \quad (94)$$

### A.4 Program for the calculation of the matrix elements of the second and fourth order tensor operators $U_2$ and $U_4$

The matrices of the tensor operators  $U_2$  and  $U_4$  of the second and fourth order, respectively, are transformed with the matrix M of eigenvectors of the total matrix A:

$$U_{22}=M^{-1}*U_2*M; \quad (95)$$

$$U_{44}=M^{-1}*U_4*M;$$

Operator values of the n to m level transition with energy  $Ksi[m]-Ksi[1]$  are given by:

$$> UU2(m,n)=print(m,n,Ksi[n]-Ksi[m],U_{22}[m,n],U_{44}[m,n]). \quad (96)$$

The effective cross-section of the n to m state transition with the use of the experimental parameter  $a_2$  is given by:

$$> Q(a_2,n,m)=a_2(U_{22}[n,m])^2+a_2(U_{44}[n,m])^2;$$

$$Q_{t0}=\text{sum}(\text{sum}((U_{22}[j,m])^2+(U_{44}[j,m])^2,j=1..4),m=5..16); \quad (97)$$

$$Q_1(a_2,m)=\text{sum}(Q(a_2,j,m),j=1..4).$$

The calculation of experimental parameter  $a_2$  from the lifetime  $t_0$  is the following:

$$a_2=4.52*\epsilon/t_0/E(6)^3/(2*Q_{t0}(\pi)+Q_{t0}(\sigma)). \quad (98)$$

Oscillator strengths of the transitions of the absorption spectrum from levels 1-4 to levels 5-120 were calculated. The absorption spectrum  $f_{abs}$  vs  $h\nu$  is given by:

$$> f_{abs}(a_2,s_2,h\nu)=\text{sum}(Q_1(a_2,p)*(Ksi[p]-Ksi[1])\exp(-(h\nu-Ksi[p]+Ksi[1])^2/(s_2)^2),$$

$$p = 5..120)/10^4*h\nu. \quad (99)$$

The oscillator strength of the transition from the ground state to the level m is given by:

$$f(a_2,m)=Q_1(a_2,m)*E(m). \quad (100)$$

The absorption spectrum oscillator strength  $f_{nm}$  vs  $h\nu$  for level n to m transition is:

$$f_{nm}(a_2,s_3,n,m,h\nu)=Q(a_2,n,m)*(Ksi[n]-Ksi[m])*\exp(-(h\nu-Ksi[n]+Ksi[m])^2/(s_3)^2)/10^4*h\nu. \quad (101)$$

A table of the initial STS[1] and the  $m^{\text{th}}$  level STS[m], the transition energies  $Ksi[m]-Ksi[1]$  and the oscillator strengths  $10^7 f(a_2,m)$  are:

$$> \text{for } m \text{ from } 5 \text{ to } 120 \text{ do } print(m,STS[1],STS[m],(Ksi[m]-Ksi[1]),$$

$$10^7 f(a_2,m)) \text{ end do.} \quad (102)$$

The absorption spectrum diagram is given by:

$$plot(f_{abs}(a_2,s_2,h\nu),h\nu=22000..2000,colour=black). \quad (103)$$

The oscillation force of transitions from an excited state  $j_1$  to the levels  $j_2=1..j_1-1$  is:

$$> f_{j1}(a_2,s_3,j_1,h\nu)=\text{sum}(f_{nm}(a_2,s_3,j_1,j_2,h\nu),j_2=1..j_1-1). \quad (104)$$

The program was developed to: 1. calculate the oscillator strengths and lifetimes of any transition, 2. to model the absorption and luminescence spectra, and 3. to model the absorption transitions starting from an excited state.

To use the program, one needs to know the lifetime of a level and the experimental absorption spectrum. This data is used to choose the parameters of the transition energy, intensity, and average transition bandwidths  $s_2$ ,  $s_3$ , to enable maximal experimental – modeled spectra agreement. Finally, we used the program to calculate the spectral characteristics of  $Co^{2+}$ ,  $Fe^{2+}$ , and  $Ni^{2+}$  in ZnSe.

## LIST OF SYMBOLS, ABBREVIATIONS, AND ACRONYMS

IR	Infrared
TM	Transition metal
RT	Room temperature
UAB	University of Alabama Birmingham
GPI	Prokhorov General Physics Institute
PL	Photoluminescence
AFM	Atomic Force Microscopy
CF	Crystal Field
TS	Tanabe-Sugano
SO	Spin-orbit
MO	Molecular orbital
PMMO	Phenomenological method of molecular orbital
ED	Electric dipole
CFP	Crystal field potential
CC	Configuration curves
CHV	Coefficients of the harmonic vibrations
CW	Continuous wave
STS	States

## DISTRIBUTION LIST

DTIC/OCP 8725 John J. Kingman Rd. Suite 0944 Ft. Belvoir, VA 22060-6218	1 cy
AFRL/RVIL Kirtland AFB, NM 87117-5776	1 cy
Dr. Leanne Henry Official Record Copy AFRL/RDLTS	1 cy